Université d'Ottawa · University of Ottawa

Université d'Ottawa · University of Ottawa

FACULTÉ DES ÉTUDES SUPÉRIEURES ET POSTDOCTORALES

FACULTY OF GRADUATE AND POSTDOCTORAL STUDIES

Matthew Gerard DOYLE

AUTEUR DE LA THÈSE - AUTHOR OF THESIS

M. A. Sc. (Mechanical Engineering)

GRADE - DEGREE

Department of Mechanical Engineering

FACULTÉ, ÉCOLE, DÉPARTEMENT - FACULTY, SCHOOL, DEPARTMENT

TITRE DE LA THÈSE - TITLE OF THE THESIS

Simulation of Blood Flow in a Ventricular-Assist-Device with Fluid-Structure Interaction Effects

S. Tavoularis

DIRECTEUR DE LA THÈSE - THESIS SUPERVISOR

Y. Bourgeault

CO-DIRECTEUR DE LA THÈSE - THESIS CO-SUPERVISOR

EXAMINATEURS DE LA THÈSE - THESIS EXAMINERS

D. Feszty

T. Mussivand

J.-M. De Koninck, Ph.D.

LE DOYEN DE LA FACULTÉ DES ÉTUDES SUPÉRIEURES ET POSTDOCTORALES

DEAN OF THE FACULTY OF GRADUATE AND POSTDOCTORAL STUDIES

Simulation of Blood Flow in a Ventricular Assist Device with Fluid-Structure Interaction Effects

Matthew G. Doyle

A thesis submitted to the Faculty of Graduate and Postdoctoral Studies
in partial fulfillment of the requirements for the degree of

MASTER OF APPLIED SCIENCE

in Mechanical Engineering

Ottawa-Carleton Institute for Mechanical and Aerospace Engineering
University of Ottawa
Ottawa, Canada

April 2004

Your file Votre référence
ISBN: 0-494-01465-2
Our file Notre référence
ISBN: 0-494-01465-2

ABSTRACT

Numerical simulations combining solid and fluid models and fluid-structure interaction effects were performed for a diaphragm-type ventricular assist device (VAD). These simulations include an open loop configuration, in which the VAD inlet and outlet tubes are open to the surroundings, and a closed loop configuration, in which the VAD is connected to an idealized model of the circulatory system.

Comparisons have been made between the open loop case and previous experimental and numerical results for a similar VAD designed by a group at Brunel University. Differences between the two models can be partially accounted for by differences in flow forcing. Even with these differences, this comparison validates this method as a tool for the design and optimization of VADs.

For the closed loop case, results were limited by the required use of a slightly compressible fluid model. Further relaxation of this requirement is needed to fully explore closed loop simulations.

ACKNOWLEDGEMENTS

I would like to thank my co-supervisors, Dr. Stavros Tavoularis and Dr. Yves Bourgault for all of their help with this research. Without their ideas, knowledge, and support, this work would not have been possible. A special thank you for their financial support for the past eight months.

I would also like to thank my thesis defence examiners, Dr. Tofy Mussivand and Dr. Daniel Feszty, for their comments during my defence. Your recommendations have allowed me to improve the quality of my thesis.

I am grateful to the support staff at ADINA, especially Yanhu Guo, Gustavo Ledezma, and Theodore Sussman, for answering all of my technical questions about the ADINA software and fixing bugs in the code that limited my work.

I am grateful to HPCVL for allowing me to run simulations on their computer network, enabling me to run more complex computations than I would have been able to run otherwise. A special thank you to Nabil Benabbou for his support with HPCVL.

I would like to thank the other graduate students in our research group, especially Warren Dunn and Pascal Tremblay. Warren, thank you for giving your time to answer all of my questions about graduate student life, research, and thesis writing. Pascal, thank you for sharing your CFD knowledge and ideas with me.

A special thank you to my Mom and Dad, my brother, Blair, and my fiancée, Kim Adams. Without your support, it would have been very difficult to complete this work.

Lastly, thank you to NSERC and the University of Ottawa Faculty of Graduate Studies for funding during the first two years of this research. My NSERC-PGSA and University of Ottawa Excellence Scholarship helped greatly with my expenses during this research.

TABLE OF CONTENTS

LIST OF FIGURES

LIST OF TABLES

NOMENCLATURE

A	cross-sectional area
$\mathbf{C}$	damping matrix
C_a	total arterial compliance
C_v	total venous compliance
D	distensibility
$\boldsymbol{d}$	displacement vector
E	Young's modulus of elasticity
$\mathbf{F}$	force vector
$\boldsymbol{f}^B$	body force per unit volume
g	gravitational acceleration
h_i	head
K	permeability
$\mathbf{K}$	stiffness matrix
$\boldsymbol{k}$	specific permeability vector
L	length
$\mathbf{M}$	mass matrix
p	pressure
Q	volumetric flow rate
$\mathbf{R}$	external load vector
R_p	total peripheral resistance
Re	Reynolds number
t	time
$\mathbf{U}$	displacement vector
u	displacement
v	fluid velocity vector
w	mesh velocity vector
$\mathbf{X}$	solution vector
z	elevation with respect to reference level

Greek letters

κ	fluid bulk modulus of elasticity
λ	relaxation factor
μ	fluid viscosity
ν	Poisson ratio
ρ	density
ρ_m	compressible fluid density
τ	stress tensor
ϕ	porosity

Subscripts

d	displacement
f	fluid
s	solid
τ	stress

Other Notation

$\bar{a}$	average of property a
$\underline{(...)}$	fluid-structure boundary
$\dot{a}$	time derivative of property a
$\ddot{a}$	second time derivative of property a

Acronyms

ALE	arbitrary-Lagrangian-Eulerian
BU-VAD	Brunel University ventricular assist device
CFD	computational fluid dynamics
FSI	fluid-structure interaction
LDV	laser Doppler velocimetry
TAH	total artificial heart
TR-BDF	Trapezoidal Rule / Backward-Differentiation-Formula
VAD	ventricular assist device

CHAPTER 1
INTRODUCTION

1.1 Motivation

Heart disease is one of the leading causes of death in the industrialized world. One of the most severe types of heart disease is heart failure, in which the heart can no longer pump an adequate amount of blood through the body. Currently, the best treatment for heart failure is a heart transplant, but the need for donor hearts greatly exceeds the supply (Collard *et al.*, 2003). In response to this need, biomedical researchers are developing medical devices that can aid diseased hearts in the pumping of blood while patients are awaiting transplants. One such group of devices and the focus of this research are ventricular assist devices (VADs).

VADs are connected between the heart and a major artery to help pump blood through the body. Currently available VADs are either partially implantable or externally installed devices and are mainly used as a bridge to transplantation. Recently, several companies have been developing fully implantable devices, with the goal being to use these devices as an alternative to transplantation.

As described in the next chapter, there are many different types of VADs. The present research, however, is concerned with the diaphragm-type VAD, which consists of two

fluid chambers separated by a flexible diaphragm. One of the fluid chambers contains blood and is connected to the body by separate inlet and outlet tubes. The other chamber contains a driving fluid, with a common inlet/outlet tube. A pump is used to move the driving fluid into its chamber, causing the diaphragm to deform towards the blood chamber, which results in the ejection of blood into the body. Reversal of the driving fluid direction causes evacuation of the driving fluid chamber, which allows the blood to fill the blood chamber so that the cycle can be repeated.

Due to the interdependence of the diaphragm and fluid motions, numerical modelling of these devices has been limited by the inability to model this fluid-structure interaction (FSI) properly. It is, therefore, worthwhile to use computational methods in an attempt to incorporate FSI effects in the simulation of VAD operations.

Fluid dynamics are essential to the design and optimization of VADs, as unwanted flow features lead to device failure and blood degradation. Long residence times inside the VAD can lead to the formation of a thrombus in the VAD (Anderson *et al.*, 2000). Also, hemolysis tends to occur in regions of high shear stress or high levels of turbulence (Anderson *et al.*, 2000; Baldwin *et al.*, 1989 and 1990). Therefore, in order to optimize the design of a VAD, the fluid dynamics need to be well understood through either experiments or computational fluid dynamics (CFD).

1.2 Objectives and Scope

The primary objective of this study is to numerically simulate the operation of a diaphragm-type VAD with FSI effects. A secondary objective is to simulate the operation of a VAD coupled to a representative model of the systemic circulatory system.

The VAD geometry used in this research is based on an idealized model from Brunel University, which does not include FSI effects. It consists of two hemispherical chambers separated by a circular diaphragm. The driving fluid chamber has a common inlet/outlet tube through which the flow is driven, while the upper chamber has separate inlet and outlet tubes with valves to control the flow direction. Two cases will be

considered. First, the VAD will be connected in an open loop to a constant pressure reservoir. Second, the inlet and outlet of the VAD blood chamber will be connected to a three-dimensional representation of the systemic circulatory system. This coupling forms a closed loop, which creates additional computational challenges. The circulatory loop in this research contains two elastic tubes to represent total arterial and venous compliances and a porous medium to represent peripheral resistance.

1.3 Outline of Thesis

This thesis is organized into five chapters: Introduction, Background and Literature Review, Mathematical Models and Numerical Procedures, Results and Discussion, and Conclusions and Recommendations for Future Research. The Background and Literature Review section provides information about the human cardiovascular system and the different types of VADs. Also contained in this section is information about models of the circulatory system and previous experimental and computational studies of VAD models. The Mathematical Models and Numerical Procedures section contains details on the computational model used in this research and the implementation of this model in the finite element software ADINA. This is followed by a presentation of the results obtained in this research and a discussion of these results. Lastly, conclusions are presented along with recommendations for extensions and future applications of this research.

CHAPTER 2

BACKGROUND AND LITERATURE REVIEW

2.1 Cardiovascular System

The cardiovascular system is a major system in the human body, consisting of the heart and blood vessels, whose purpose is to move blood through the body. The heart muscle acts as a pump in the system, expanding and contracting to send and receive blood. The blood vessels, including arteries, arterioles, capillaries, venules, and veins, are the piping components that allow for distribution of the blood through the body (Tortora, 2002).

The human heart consists of four chambers: two upper chambers, the left and right atria, and two lower chambers, the left and right ventricles (Tortora, 2002). The identification of left and right is based on how a person views their own heart. The heart has four unidirectional valves: the bicuspid valve, which separates the left atrium and ventricle; the tricuspid valve, which separates the right atrium and ventricle; the aortic valve, which separates the left ventricle from the aorta; and the pulmonary or mitral valve, which separates the right ventricle from the pulmonary artery (Tortora, 2002). Figure 1 shows the layout of the four chambers of the heart as well as the direction of blood flow to and from the heart.

Blood vessels carry the blood to and from the heart. Blood vessels can be divided into three major classes, arteries, veins, and capillaries. Arteries carry blood from the heart,

while veins carry blood back to the heart. The capillaries are small blood vessels that join the arteries and veins. It is through the capillaries that oxygen is transferred from blood to the surrounding tissues. Two major differences exist between blood vessel walls and more traditional engineering pipe materials. Unlike pipes, which are generally rigid and solid, blood vessel walls are both elastic and porous. The consequence of this is that, as blood travels through the blood vessels, the walls expand and contract. As well, nutrients can be transferred to the surrounding tissues through the pores in the blood vessel walls. These pores are selectively permeable, allowing nutrient transfer while preventing red blood cells from leaving the vessels (Fung, 1990).

Two major circulation paths make up the cardiovascular system, the pulmonary circulation, which carries blood between the heart and lungs, and the systemic circulation, which carries blood from the heart through the body and back. The purpose of the pulmonary circulation system is to take deoxygenated blood from the heart to the lungs, where carbon dioxide is released and oxygen is added, and return the blood to the heart. The systemic circulatory system involves the movement of oxygenated blood from the heart through the body. Nutrients and oxygen from the blood can then be transferred to the tissues that surround the blood vessels. The systemic circulatory system begins in the left atrium, which receives oxygenated blood from the pulmonary veins. The blood then moves from the left atrium to the left ventricle where it is pumped into the aorta, the largest artery in the body. From the aorta, the blood travels through the arteries into the capillaries and returns to the right atrium through the veins (Tortora, 2002).

The heart is continually expanding or contracting. This motion creates pulsatile blood flow, which moves the blood as pressure waves through the body. One complete cardiac cycle occurs during every heartbeat. Two important terms describe the motion of the heart chambers during the cycle, systole and diastole. Systole is the contraction of a chamber, while diastole is the relaxation of a chamber (Tortora, 2002).

The cardiac cycle begins with the ventricles in diastole during a period known as passive ventricular filling. This phase begins when the atrial pressure exceeds the ventricular

pressure causing the bicuspid and tricuspid valves to open (Tortora, 2002). Three-quarters of the way through ventricle filling, atrial systole occurs. Once atrial systole has stopped, ventricular systole begins. As the ventricles contract, the bicuspid and tricuspid valves are forced closed. At this moment, all four valves are closed. The aortic and mitral valves remain closed until the left ventricular pressure exceeds the arterial pressure, at which point both valves open and blood begins to flow into the arteries (Tortora, 2002). Once the ventricular diastole begins, the aortic and mitral valves close and all four valves remain closed until ventricular filling begins again.

2.2 Ventricular Assist Devices and Total Artificial Hearts

Since the early 1800s, people have thought about using medical devices to aid or replace the human heart. However, it was not until the early 1950s when mechanical devices began to be used to help the heart. In 1954, Gibbons published a paper describing the first successful open-heart surgery using a heart-lung machine. In the 1960s, the first ventricular assist device (VAD) and the first artificial heart were both implemented. Today, many groups all over the world are designing both total artificial hearts (TAHs) and VADs using many different technologies. For a more detailed description of the history of VADs the reader is referred to Frazier *et al.* (2000) and Fuchs and Netz (2002) and the references contained therein.

A VAD is a medical device used when one ventricle in the natural heart is diseased and no longer able to pump the required amount of blood through the body. A VAD is a mechanical pump that increases the amount of blood pumping through the body to an acceptable level. The device is either attached to the left ventricle and the aorta, or the right ventricle and the pulmonary artery depending on which side is diseased (Fuchs & Netz, 2002; Reul *et al.*, 1998). Because the resistance to pumping is much higher on the left ventricle than the right, left VADs are much more common than right ones.

Once a VAD is attached to a diseased ventricle, the pumping requirements of the ventricle are reduced. If the ventricle is not permanently damaged, this reduction of work may permit healing of the damaged heart muscles (Fuchs & Netz, 2002). If the heart is

permanently damaged, the VAD can be used as a bridge to transplantation. Due to the shortage of donor organs, it is hoped that fully implantable VADs can be developed as an alternative to transplantation, rather than a bridge.

According to Reul *et al.* (1998), thirty percent of patients who need a VAD for their left ventricle on a more long-term basis develop problems with their right ventricle as well. As a result, some of the existing VADs offer biventricular support. As an alternative to biventricular support and in cases where transplantation is not an available option, a TAH can be used.

VADs can be classified in many ways. One way to classify them is by whether or not the device is implantable. VADs that are outside the body are called extracorporeal devices, whereas those that are inside the body are intracorporeal devices. Extracorporeal devices in which the blood pump is in contact with the body are sometimes referred to as paracorporeal devices.

Intracorporeal devices can be divided into two subgroups. Intracorporeal devices that are currently in use have tubes that attach the internal and external components through the skin. These devices are called partially implantable. The next generation of intracorporeal devices, currently in the development stages, are fully implantable devices. All energy transfer and communication with external components in these devices is done using special coils on either side of the skin, so that no tubes go through the skin (Hendry *et al.*, 2001). Table 2-1 summarizes the devices in each category, all of which produce pulsatile flow. Each of these devices is described below following a brief discussion of non-pulsatile devices.

Non-pulsatile VADs offer several advantages over pulsatile VADs. They are smaller, quieter, and simpler to implant and remove (Collard *et al.*, 2003). However, they produce flow which is different from the physiological pulstaile flow produced by ventricular contraction. Also, according to Fuchs and Netz (2002), the range of survival for patients with pulsatile devices is 25 - 80 % compared to 25 - 40 % with non-pulsatile

devices. As both devices have widespread use, the modelling of a pulsatile device continues to be a relevant research topic.

Non-pulsatile VADs: Three non-pulsatile VADs with axial flow pumps are currently available. Two of these devices, the HeartMate II VAD and the MicroMed DeBakey VAD attach to the body between the apex of the left ventricle and the aorta. The third device, the Jarvik 2000, fits inside the left ventricle. For further information about these devices, the reader is referred to the references contained in the review article by Collard *et al.* (2003).

Table 2-1. Types of Pulsatile VADs.

Type of VAD	Name of Device	Manufacturer	Country
Extracorporeal			
	ABIOMED BVS 5000	ABIOMED Inc.	USA
Paracorporeal	Thoratec VAD	Thoratec Corporation	USA
	Medos/HIA-VAD	MEDOS Medizintechnik AG	Germany
	Berlin Heart	Berlin Heart AG	Germany
Intracorporeal			
Partially Implantable	TCI HeartMate IP / VE	Thoratec Corporation	USA
	Novacor LVAS	World Heart Corporation	Canada
Fully Implantable	HeartSaver	World Heart Corporation	Canada
	LionHeart LVD-2000	Arrow International, Inc.	USA

ABIOMED BVS 5000: The ABIOMED BVS 5000, manufactured by ABIOMED Inc. of Danvers, Massachusetts, is an extracorporeal VAD that can provide support for one or both ventricles (Chen *et al.*, 1999). This device differs from most other extracorporeal devices in that the pumping system does not rest on the exterior of the skin, but rather in a large console adjacent to the patient's bed. This console pneumatically drives air through two tube-like chambers, containing synthetic trileaflet valves and flexible sacs. Figure 2 shows the ABIOMED BVS 5000 attached to a patient for biventricular support.

Thoratec VAD: Thoratec Corporation, of Pleasanton, California, currently manufactures three VADs, the Thoratec VAD, the TCI HeartMate IP, and the TCI HeartMate VE (Collard *et al.*, 2003). The Thoratec VAD is an extracorporeal device with a paracorporeal pump placement. It can be used to support the left or right ventricle or both (Reichenbach *et al.*, 2001). In the Thoratec VAD, blood is pumped through the body by the expansion and contraction of a pneumatically driven blood sac (Pennington *et al.*, 2000). The valves in the Thoratec VAD are tilting disk valves. Figure 3 is an illustration of the locations of the components of the Thoratec VAD on the body for biventricular support.

Medos/HIA-VAD: The Medos/HIA-VAD is an extracorporeal device with paracorporeal pump placement developed in Germany by the Hemholtz Institute in Aachen (HIA) (Herwig *et al.*, 1997). This device has two chambers, separated by a diaphragm and offers uni- or biventricular support. Air is pumped in and out of the first chamber causing the diaphragm to move up and down, which forces blood in and out of the second chamber. Polyurethane trileaflet valves are used at the entrance and exit of the blood chamber in this device. Figure 4 is a cross-sectional view of the Medos/HIA-VAD.

Berlin Heart: The Berlin Heart is an extracorporeal, pneumatically driven VAD with a paracorporeal pump (Loebe *et al.*, 2000). What distinguishes it from other similar devices is the multi-layer membrane separating the air and blood chambers. Two of the membranes move in response to the flow of air in the chamber, while the third membrane, which is in contact with the blood, moves because of the motion of the other membranes (Loebe *et al.*, 2000). Two types of valves are used in the Berlin Heart depending on the size of the device, tilting disk valves or polyurethane trileaflet valves. A cross-sectional view of the Berlin Heart with tilting disk valves is given in Figure 5.

TCI HeartMate IP and VE: The Thoratec Corporation currently produces two models of HeartMate VADs, the IP and VE devices. The two HeartMate VAD models are intracorporeal partially implantable devices. The HeartMate devices have a pusher plate, which pushes a diaphragm causing blood to flow through the body (Fuchs & Netz, 2002).

The difference between the two HeartMate devices is that the IP device is pneumatically driven, while the VE device is electrically driven (Delgado *et al.*, 2002). The VE version of the HeartMate VAD is shown in Figure 6.

Novacor LVAS: The Novacor LVAS, shown in Figure 7, is a unique intracorporeal partially implantable VAD manufactured by the World Heart Corporation, which is based in Ottawa (Collard *et al.*, 2003). This device uses two pusher plates to push blood out of a flexible sac, rather than the more common one pusher plate design (Yu *et al.*, 2001). A solenoid is closed causing two springs to move the pusher plates towards each other causing the blood to flow out of the blood sac.

HeartSaver VAD: The World Heart Corporation in Ottawa is developing a totally implantable VAD called the HeartSaver (Figure 8; Hendry *et al.*, 2001). The implantable components of this system include the pump, an internal battery, and a remotely controlled electronic system. Recharging of batteries is done transcutaneously through an electromagnetic coil. Blood pumping action is effected by transferring hydraulic fluid between a volume displacement chamber and the pumping chamber of the VAD through one-way valves. This deforms a diaphragm separating the pumping chamber from a flexible blood sac. Diaphragm displacement causes pumping of blood out of and into the VAD.

LionHeart LVD-2000: The LionHeart LVD-2000 is a joint project in the development stages between Arrow International and Pennsylvania State University (Mehta *et al.*, 2001). It is being designed as an alternative to transplantation, and is fully implantable. Figure 9 shows the implantable components of the LionHeart LVD-2000 and their positions in the body. The LionHeart LVD-2000 uses a pusher plate to push blood out of a flexible blood sac, and tilting disk valves at the inlet and outlet.

2.3 Circulatory System Models

The volume of blood ejected from the heart during each cardiac cycle is determined by four factors: heart rate, heart muscle contractility, preload, and afterload (Berne & Levy,

1992). While the first two of these factors are dependent on the heart itself, the other two depend on the heart and the blood vessels. It is therefore necessary to couple any natural or artificial heart model with a model of the circulatory system in order to represent the interaction between them properly.

Due to the complexity of the natural circulatory system, it is extremely difficult to construct a model that accurately simulates all details either experimentally or computationally. Instead, models of varying complexity and order can be used to represent some functions of the circulatory system.

The circulatory system can be represented by compliant and resistive elements. In this context, compliance is defined as the change in volume of a vessel divided by the change in pressure ($C = dV/dP$), and resistance is defined as the change in pressure divided by the volumetric flow rate ($R = dP/Q$). Compliant and resistive elements can be used to represent sections of the circulatory system or specific vessels depending on the level of detail desired. In addition to compliant and resistive components, the inertial effects due to blood flow should also be represented.

One of the simplest ways to represent the circulatory system either experimentally or computationally is through electric circuit models. In these models, three types of components are used: resistors, which represent the viscous effects of the blood flow; capacitors, which represent the compliance of the blood vessel walls; and inductors, which represent the inertial effects of the blood flow. The pressure and velocity in the system are normally represented by voltage and current, respectively. These models can be used to represent the entire cardiovascular system, including the natural heart and artificial medical devices. Valves can be simulated in the system experimentally using diodes, as diodes only permit unidirectional flow, or computationally, using if-else statements. Complex branching models can be developed to include as much or as little detail as desired. While some electric circuit models consist of many elements, others lump together all blood vessels into a three-element model. For examples of electric circuit models, the reader is referred to Verdonck *et al.* (1998) or Formaggia *et al.* (1999).

Experimentally, models that are more complex can be developed using various components to represent the compliance and resistance in the circulatory system. One example of a well-known experimental system is the Pennsylvania State University Mock Circulatory System (Rosenberg *et al.*, 1981). In this loop, adjustable piston-spring systems are used to represent compliance and small tubes placed between two flat plates are used to represent resistance.

Computationally, different orders of equations can be developed to model the circulatory system depending on the detail required. The simplest of these are lumped or zero-dimensional models made up of ordinary differential equations. These equations can be derived from electric circuit models.

The next class of models are one-dimensional. These models consist of partial differential equations and take into account the cross-sectional area through which blood flows in a vessel (Formaggia *et al.*, 1999). These models do not give any spatial information about the blood flow, but do allow for the simulation of pressure waves through the vessel.

To get spatial information about the fluid flow in the circulatory system, more complex two-dimensional and three-dimensional fluid models can be used. In these models, the Navier-Stokes equations can be used to model the fluid behaviour inside blood vessels. The move from one to two or three dimensions greatly increases the complexity in the system and thus the computational time. In models of the circulatory system in which the interest is in a specific vessel, a two- or three-dimensional model of that vessel can be coupled to a one-dimensional model of the surrounding vessels. An example of the application of this coupling can be found in the article by Formaggia *et al.* (2000).

If the inertial effects of blood are neglected, three parameters are required in a model of the systemic circulation: total arterial compliance, C_a; total venous compliance, C_v; and total peripheral resistance, R_p (Berne & Levy, 1992). Several values of C_a and R_p proposed in the literature are presented in Table 2-2. Once a C_a value is chosen, the value

of C_v can be calculated based on a relationship developed by Guyton and Hall (2000). To relate the two compliance values, the distensibility of the arteries and veins must be used. Distensibility, D, is a property of a vessel wall and is a measure of the ability of the wall to deform. It is defined as $D = (1/V)(dV/dP)$, where V is the undeformed volume inside the vessel. Using this definition, compliance can be calculated as the product of the vessel distensibility and the undeformed volume inside the vessel. Veins are approximately eight times more distensible than arteries and contain about three times more blood in their undeformed state, leading to the relationship $C_v = 24C_a$ (Guyton & Hall, 2000). A comparable relationship, $C_v \approx 20C_a$, was used by Berne and Levy (1992).

Table 2-2. Total arterial compliance and peripheral resistance values.

C_a ($\times 10^8$) (m^5/N)	R_p ($\times 10^{-8}$) ($N \cdot s/m^5$)	Source
1.2	1.6	Rosenberg *et al.* (1981)
0.38 - 1.5	0.8 - 2.4	Segers *et al.* (2002)
1.8	1	Geertsema *et al.* (1997)
----	0.9 - 1.8	Tsach *et al.* (1989)
----	1.4	Hoppensteadt and Peskin (2002)
----	1.3	Guyton and Hall (2000)

2.4 Experimental and Computational Studies of VADs and TAHs

Several effects must be taken into account in the modelling of a VAD or TAH. These include the three-dimensionality and unsteady nature of the flow inside the VAD or TAH chambers. Another significant effect in the modelling of such devices is the interaction between fluids and flexible solid materials, such as a diaphragm or blood sac. This effect, commonly referred to as fluid-structure interaction (FSI), has been neglected in many previous VAD and TAH studies. Inclusion of FSI effects would add significant complication in a numerical simulation, because it would require the solution of coupled equations governing the fluid and solid motions. Below is a review of previous computational models and experimental studies of VADs and TAHs.

An early computational study of steady flow in a two-dimensional representation of a TAH without FSI effects was done by Kim *et al.* (1992). They modelled various types of valves, in stationary positions, at the inlet and outlet of the TAH. Of note in this model is the simulation of turbulent as well as laminar flow. On the experimental side, Orime *et al.* (1994) and Nakata *et al.* (1998) performed flow visualization on different TAH designs for design optimization.

Henry *et al.* (1997) performed experimental and computational studies on flow inside a skeletal muscle ventricle (SMV). An SMV is similar to a VAD or TAH in that it helps the heart pump blood through the body. However, rather than using an artificial device, a SMV uses a person's own muscles to aid in the pumping. FSI effects have been neglected in their computational study, as the motion of the ventricle walls was prescribed.

Chesler and Kamm (1998) performed CFD simulations on a similar device that is a hybrid between a VAD and a SMV. Their device is artificial, but uses the person's muscles to supply the power. Unlike most VADs, the one in this study has a common inlet/outlet instead of separate tubes. Their simulation was for three-dimensional unsteady flow with prescribed motion.

Several papers have been published on experimental or computational studies of flow inside the Penn State VAD. The Penn State VAD, which became the LionHeart LVD-2000, consists of a flexible blood sac with a circular cross-section. Instead of a flexible diaphragm, a rigid pusher plate is used to drive the flow of blood in this VAD. Experimentally, Laser Doppler velocimetry (LDV) measurements for this VAD have been published by Baldwin *et al.* (1989; 1990; 1994). In addition, Bachmann *et al.* (2000) performed LDV measurements on a paediatric version of the Penn State VAD for both Newtonian and non-Newtonian fluids. While these experimental studies focused on the fluid dynamics, Hochareon *et al.* (2003) have developed a simplified model of the LionHeart VAD to study the interaction between the fluid and the solid diaphragm motion. Flow visualization results are presented for this work.

Computationally, Kiris *et al.* (1997) performed a study on an idealized version of the Penn State VAD geometry. In their model, the VAD is cylindrical with cylindrical inlet and outlet tubes and a circular pusher plate to drive the fluid motion. Tilting disk valves are present at the ends of the inlet and outlet tubes, and their motion is prescribed based on previous experimental work. Qualitative velocity vector plots are provided by Kiris *et al.* (1997) in a plane containing the centre of the VAD inlet and outlet tubes. A similar CFD study on a sac-type VAD was done by Okamoto *et al.* (2003). This study, which did not include FSI effects, was done for steady flow only.

One study that has included FSI effects is that of Zhang and Hisada (2001), with their focus being on the large structural deformation of a diaphragm in an artificial heart. They present two tests cases in their work. The first is a two-dimensional model of a blood chamber with separate inlet and outlet tubes. A pressure is applied directly to the diaphragm to control the deformation and drive the fluid flow. Their second study is of a three-dimensional cylindrical artificial heart with a circular membrane in the centre of the cylinder separating it into two fluid chambers. Each of the fluid chambers has a single inlet/outlet tube aligned with the primary flow direction. The flow in their system is driven by a velocity applied to the end of one of the tubes. While several results are shown for the diaphragm motion, no results for the fluid motion are presented.

The research that is most closely related to the present research is that of a group at Brunel University in Uxbridge, Middlesex, United Kingdom (Clark *et al.*, 1990). Details of their studies are presented in the next section.

2.5 Brunel University VAD

The original design studied by the Brunel University group was that of T. Gilken Co. of Japan. Their major interest in this design was to study the flow of blood inside the device for design optimization. The T. Gilken Co. VAD, as shown in Figure 10, is ovoid in shape, divided into two parts by a diaphragm. The upper chamber of the device holds blood and is connected to the body through an inlet and outlet, both containing Sorin

Biomedica tilting disk valves (Clark *et al.*, 1990). The lower chamber contains air, which is driven into and out of the chamber pneumatically through a small tube.

Flow visualization and velocity measurements in this VAD were made for steady (Clark *et al.*, 1990) and unsteady flow (Jin & Clark, 1993). The results of this experimental work were limited by a lack of visibility in some parts of the VAD (König *et al.*, 1999a).

König *et al.* (1999a; 1999b) reviewed some CFD studies of VADs and TAHs and found somewhat limited results, with little or no validation. As a result, they decided to develop a simplified model of a VAD, in order to generate comparable experimental and CFD results. The idealized Brunel University VAD (BU-VAD) has a hemispherical blood chamber with cylindrical inlet and outlet tubes as shown in Figure 11. This model is twice the size of an actual VAD to permit easier flow visualization (König *et al.*, 1999a). Instead of a diaphragm, a hemispherical piston with prescribed motion is used in their model. Valves in the simplified model were specified as completely open or completely closed (König *et al.*, 1999b). Computationally, when the valve is closed, it is modelled as a wall with zero velocity. A solenoid-driven plate containing two holes was used to open and close the valves in the experimental set-up. Both CFD analysis and experimental measurements were performed on this simplified model (König *et al.*, 1999a; 1999b; König & Clark, 2001). The results of this work are summarized below.

Qualitative flow visualization and CFD simulation results are available for the BU-VAD (König *et al.*, 1999a; 1999b). Quantitatively, three pieces of information are available for comparison. First, a maximum Reynolds number of 3300 found at the entrance of the VAD inlet and the exit of the VAD outlet (König *et al.*, 1999b). Second, ensemble averaged LDV measurements and CFD computations of the velocity component perpendicular to the VAD inlet and outlet tubes at three points in the VAD (König *et al.*, 1999b). Third, experimental and computational pressure measurements at the apex of the blood chamber (König & Clark, 2001). Details on the velocity and pressure variations are presented in Section 4.2.1.

As mentioned in Section 1.2, the VAD modelled in this research is based on the BU-VAD. Comparisons to the above-mentioned BU-VAD results will be used for partial validation of the current research, in the absence of more directly comparable literature.

CHAPTER 3
MATHEMATICAL MODELS AND NUMERICAL PROCEDURES

3.1 Hardware

Prior to choosing the software for the computations in this research, it was necessary to assess the available computer resources. Computations for this research were done using two computer systems, a local Beowulf cluster and a remote high performance computer network. The Beowulf cluster, located in the Department of Mathematics and Statistics at the University of Ottawa, contains eight nodes, each with two Pentium 3 800 MHz processors and 1 GB of RAM. All pre-processing and most post-processing were done on the Beowulf cluster as well as testing of model parameters and smaller computations.

The second computer system is the High Performance Computing Virtual Laboratory (HPCVL), a high performance computer network jointly funded by four Ontario Universities, Queen's University, the Royal Military College of Canada, Carleton University, and the University of Ottawa. The major computing system on HPCVL is a SunFire Cluster made up of UltraSPARC-III processors, with hundreds of gigabytes of RAM. Further details regarding this system can be found at http://www.hpcvl.org. HPCVL was used for computationally intensive models that require more than 1 GB of RAM after smaller models were tested on the Beowulf cluster.

3.2 Software - ADINA

A commercial software package has been chosen for this research instead of a code developed in-house. The use of a commercial code allowed significant savings in development time and reduced the need for validation testing. A disadvantage of using a commercial code is the lack of flexibility in controlling certain aspects of the pre- and post-processing as well as the solvers being used. However, considering the time and effort required to develop and test an in-house code, it was determined that the advantages of a commercial code exceed its disadvantages for this research.

A mandatory criterion for choosing a commercial software package for this research was the existence of FSI capabilities. Additional non-essential but desirable criteria included the availability of a parallel version, to increase the speed at which simulations can be carried out, as well as the availability of both Windows and Linux versions, allowing for computations on different computer systems. Below is a description of several commercial codes that were considered for this research, followed by a description of the chosen code, ADINA.

ANSYS/CFX: ANSYS (http://www.ansys.com), a finite element software package has recently merged with CFX, a CFD code. This merger will lead to the development of fluid-structure interaction capabilities that were unavailable when this research began. Neither software is currently available on HPCVL; however, both have parallel solvers.

Fluent/ABAQUS: Fluent, Inc. (http://www.fluent.com), a leading CFD software company, has recently begun collaborations with ABAQUS (http://www.abaqus.com) to develop FSI capabilities. Fluent is a finite volume code, unlike the other software packages considered, which are finite element codes. Fluent has parallel capabilities and is available on HPCVL. However, ABAQUS is not currently available.

Fidap: Fidap (http://www.fluent.com/software/fidap/index.htm) is a finite element CFD software package, marketed by Fluent, that has FSI capabilities and is parallelized. Fidap is now available on HPCVL but was not available when this research began.

FEMLAB: FEMLAB (http://www.comsol.com/products/femlab) is a finite element package that works as an add-on to MATLAB. It does have FSI capabilities, but is not currently available on HPCVL and has not been parallelized.

Marc: Marc (http://www.marc.com) is a parallel finite element package that is currently available on HPCVL. While Marc does have multiphysics, it does not appear to have FSI capabilities.

ADINA: ADINA v. 8.1 (http://www.adina.com), provided by ADINA R & D, Inc. of Watertown, Massachusetts, was chosen for this research because it best met our desired criteria. ADINA is one of the leading codes for FSI applications in biomechanics, is available on both HPCVL and the Beowulf Cluster, and has parallel capabilities. On both computer systems, ADINA was run in parallel using two processors, which was the maximum number available.

3.3 Fluid-Structure Interaction and the Finite Element Method

As mentioned in Section 2.4, FSI effects are important in the modelling of VADs. In recent years, the study of FSI effects in biomechanics has increased, especially in the cardiovascular research area. A few examples of other applications of FSI analysis in cardiovascular research include modelling of blood flow through a stenotic artery (Bathe & Kamm, 1999; Tang *et al.*, 2003), the left ventricle (Deserranno *et al.*, 2003), and the aortic valve (De Hart *et al.*, 2003). A three-dimensional model of the natural heart with moving valves (Peskin & McQueen, 1996) was simulated using the immersed-boundary method, which was specifically developed for the study of FSI problems in the cardiovascular system (Peskin & McQueen, 1995). In this method, rather than coupling separate fluid and solid models, the solid material is included as part of the fluid model, with additional forces added to it to mimic the behaviour of the solid (Peskin & McQueen, 1995).

While many different numerical methods, such as the finite volume method or the immersed boundary method, discussed above, can be used to solve FSI problems, the method we have chosen for this research is the finite element method. The form of the finite element method used in ADINA is the Galerkin approach, in which the weak form of the governing equations is derived. In this approach, the various terms in the equations are multiplied by weighing functions and integrated over the domain. Then, the divergence theorem is used to reduce the order of the integrals in the equation, which results in expressions that represent the natural boundary conditions of the system.

Further details of the finite element method can be found in books by Bathe (1996), Reddy (1993), Reddy and Gartling (2001), Gresho and Sani (2000), and Zienkiewicz and Taylor (2000a; b; c).

3.4 Theory and Governing Equations

The VAD in this research is an idealized device based on the BU-VAD (see Section 2.5). It is studied in two configurations, an open loop case, for which the VAD is simulated alone, and a closed loop case, for which the VAD is coupled to a three-dimensional circulatory system model. In both cases, FSI effects are taken into account. Therefore, both fluid and solid analyses must be performed in ADINA. One additional set of equations that must be defined in this model are those governing porous media flow, as a porous medium is used in this research to represent the total peripheral resistance in our circulatory system model.

To perform FSI analysis in ADINA, separate fluid and solid models must be defined. These models are coupled through coincident FSI boundaries during the solution process. Details on the equations governing these models as well as the implementation and solution of this system in ADINA are presented in the following sections. Further details can be found in the ADINA manuals (ADINA R & D, Inc., 2003a; 2003b), the finite element textbook written by the founder of ADINA, K. J. Bathe (1996), and several articles published in Computers and Structures (Bathe *et al.*, 1995; 1997; 1999; Zhang *et al.*, 2003).

3.4.1 Fluid

The flows in the VAD and circulatory system model are assumed to be laminar. While flow in an actual VAD would be turbulent, the current simulations are assumed to have laminar flow for numerical convenience and in order to match the laminar flow assumption in the BU-VAD simulations (König *et al.*, 1999b).

Two types of configurations are modelled in this research, open and closed loop. In the open loop configuration, the VAD is separated from the circulatory loop, while in the closed loop configuration, the VAD and the circulatory loop are joined together. Each of these two configurations requires the use of a different fluid model, as discussed below.

For all open loop simulations, the fluids are taken as viscous and incompressible. Therefore, the governing equations are the incompressible Navier-Stokes equations:

$$\nabla \cdot \boldsymbol{v} = 0 \tag{1}$$

$$\rho \frac{\partial \boldsymbol{v}}{\partial t} + \rho \boldsymbol{v} \cdot \nabla \boldsymbol{v} - \nabla \cdot \boldsymbol{\tau} = \boldsymbol{f}^{\mathrm{B}}, \tag{2}$$

where ρ is the fluid density, $\boldsymbol{v}$ is velocity, t is time, $\boldsymbol{\tau}$ is the stress tensor, and $\boldsymbol{f}^{\mathrm{B}}$ is the body force per unit volume. The bold characters in the above equations and throughout this thesis are used to represent vectors, tensors, or matrices.

In this research, all fluids are assumed to be Newtonian, which implies that the stress tensor in the momentum equation is defined as:

$$\boldsymbol{\tau} = -p\mathbf{I} + 2\mu\mathbf{e}, \tag{3}$$

where p is pressure, $\mathbf{I}$ is the identity matrix, μ is the fluid viscosity, and $\mathbf{e} = \frac{1}{2}\left(\nabla \boldsymbol{v} + \nabla \boldsymbol{v}^{\mathrm{T}}\right)$.

When the VAD and circulatory loop are coupled to form a closed loop, convergence can only be obtained in ADINA by using slightly compressible fluid models. The use of a slightly compressible fluid model is a requirement of the ADINA software for simulations of flow in an enclosure with moving boundaries. This requirement is due to the difficulty of conserving volume in such an enclosure with a strictly incompressible fluid. A slightly compressible fluid model was chosen over a fully compressible one due

to the desire for the fluid to be as close to incompressible as possible and the difficulties that regularly arise in using fully compressible flow solvers to simulate nearly incompressible flows.

For slightly compressible flow, the momentum equation (2) is the same as above, while the continuity equation (1) is modified to account for the compressibility of the fluid. This is done through a compressible fluid density, ρ_m, defined as (ADINA R & D, Inc., 2003b):

$$\rho_m = \rho\left(1+\frac{p}{\kappa}\right) \tag{4}$$

In this equation, κ is the fluid bulk modulus of elasticity, defined as:

$$\kappa = \rho\frac{\partial p}{\partial \rho}, \tag{5}$$

where ρ is the density of the fluid at zero pressure.

Using these above-mentioned parameters, the continuity equation can be modified to (ADINA R & D, Inc., 2003b):

$$\frac{\rho}{\kappa}\left(\frac{\partial p}{\partial t}+v\cdot\nabla p\right)+\rho_m\nabla\cdot v=0 \tag{6}$$

Once the flow is chosen to be incompressible or slightly compressible, the next step in the discretization of the governing equations is to choose the appropriate element type. Due to the complex shape of the geometry, an unstructured mesh must be used. Once this choice is made in ADINA, only one element type, four-node tetrahedral MINI elements, can be used. These elements have nodes at the four vertices at which the pressure and velocity are calculated. For stability reasons, an additional velocity node, called the bubble velocity, is placed in the centre of the element. This velocity is so named because of the shape of the basis function, which takes the value one at the centre of the element and zero on all of the faces of the tetrahedral. The MINI elements pass the LBB stability test, preventing spurious pressure modes in the solution (Gresho & Sani, 2000). These elements are first order accurate and have linear basis functions for the

nodes at the vertices. The basis function for the bubble velocity can be found as the product of the linear basis functions associated with the other four nodes.

After choosing the element type used in the fluid model, along with the necessary boundary and initial conditions, material properties, and mesh density, the fluid equations can be discretized using the finite element method. The discretized equations can then be grouped together into a system of equations, which can be written as:

$$\mathbf{F}(\mathbf{X}) = 0, \tag{7}$$

where $\mathbf{F}$ is the equation vector and $\mathbf{X}$ is the solution vector.

The above system of equations is non-linear and must be linearized in order to be solved. To do this, the Newton-Rhapson method is used. The linearized system of equations is:

$$\left(\frac{\partial \mathbf{F}(\mathbf{X})}{\partial \mathbf{X}}\right)\Delta \mathbf{X} = -\mathbf{F}(\mathbf{X}) \tag{8}$$

At each Newton-Rhapson iteration, the solution $\mathbf{X}$ is updated by $\Delta\mathbf{X}$ until convergence is reached or the user-defined maximum number of iterations is performed. The above system of equations is solved using a direct sparse solver, which is an optimized version of the Gauss elimination method. The number of elements stored in the solution matrix is minimized and then the matrix is divided into regions over which Gauss elimination can be performed. The result is a ten to one hundred times improvement in computational time. Further details on this solver are given in the ADINA-F Theory and Modelling Guide, (ADINA R & D, Inc., 2003b).

3.4.2 Porous Medium

A porous medium is a solid medium containing pores (holes) through which fluid can flow. These pores may be rigid, as is the case in this research, or flexible. Due to the small size of these pores, it is impractical to calculate the fluid flow using the Navier-Stokes equations. Instead, the average velocity over the medium is calculated. Therefore, while the previously defined continuity equation is still used for porous media

flow analysis, the momentum equation is replaced by the following empirical equation for inviscid fluid flow, known as Darcy's Law:

$$Q = -KA\frac{\Delta h}{L}, \tag{9}$$

where Q is volumetric flow rate, A is the cross-sectional area, Δh is head difference between the inlet and outlet of the porous medium, L is the distance through which the fluid flows, and K is a proportionality constant known as the permeability, which is discussed in more detail below (McCarthy, 1998).

In the above form of Darcy's Law, K depends on the properties of both the fluid and the porous medium (Scheidegger, 1974). Ideally, this constant should contain only information about the porous medium and be independent of the fluid flowing through it. To achieve this and to get the above equation into a vector form that can be used in flow simulations, several substitutions must be made. Scheidegger (1974) describes these steps in detail and a brief summary is presented below.

The first substitution is based on Bernoulli's equation, defined as:

$$h = \frac{p}{\rho g} + \frac{v}{2g} + z, \tag{10}$$

where z is the vertical elevation at a given location with respect to a reference elevation (McCarthy, 1998). In porous media flow, the velocity component in Bernoulli's equation is typically small compared to the other terms and is therefore neglected (McCarthy, 1998). The modified expression $h_i = p_i / \rho g + z_i$ can be substituted into Darcy's Law. Making this substitution, noting that $z_2 - z_1 = L$, dividing through by A, and simplifying leads to:

$$\bar{v}_f = -K'\left(\frac{\Delta p}{L} + \rho g\right), \tag{11}$$

where $\bar{v}_f$ is the average fluid velocity and K' is a modified permeability constant. By defining K', the influences of the solid and fluid parts on the permeability can be separated. It was found by Nutting in 1930 that $K' = k/\mu$, where k is specific

permeability, which depends only on the porous medium and μ is the fluid viscosity (Scheidegger, 1974).

By replacing K' by k/μ, rearranging, and taking the limit as L goes to zero, a vector form of Darcy's Law can be found as:

$$\mu k^{-1} \cdot \bar{v}_f = -\nabla p + f^B, \tag{12}$$

where f^B is the body force per unit volume. Note that in the above equation, k is a tensor, which allows for an anisotropic definition of the permeability in a porous medium.

The above form of Darcy's Law is used to calculate the average fluid velocity through a porous medium. Once the average fluid velocity is calculated, the total average velocity, $\bar{v}$, can be calculated by using the porosity, ϕ. Porosity is defined as the ratio of the volume of void space to the total volume in a porous medium. The average velocity over the entire medium is therefore:

$$\bar{v} = \phi \bar{v}_f \tag{13}$$

3.4.3 Solid

The governing equation for the solid model is given as:

$$\tau_{ij,j} + f_i^B = \rho_s \ddot{u}, \tag{14}$$

where τ is stress, f^B is body force, ρ_s is solid density, and $\ddot{u}$ is acceleration.

To determine the finite element form of the governing equations for the solid model, the kinematics of the system must be considered. In this problem, the three solid components undergo large displacements with relatively small strains. Due to these large displacements, the appropriate system of governing equations is the non-linear dynamic system given below.

$$\mathbf{M}(t+\Delta t)\ddot{\mathbf{U}} + \mathbf{C}(t+\Delta t)\dot{\mathbf{U}} + \mathbf{K}(t)\mathbf{U} = \mathbf{R}(t+\Delta t) - \mathbf{F}(t), \tag{15}$$

where $\mathbf{M}$ is the mass matrix, $\mathbf{C}$ is the damping matrix, $\mathbf{K}$ is the stiffness matrix, $\mathbf{R}$ is the external load vector, $\mathbf{F}$ is a force vector equal to the element stresses from the previous iteration, and $\ddot{\mathbf{U}}, \dot{\mathbf{U}}$, and $\mathbf{U}$ represent the acceleration, velocity, and displacement,

respectively, of the solid body nodes (ADINA R & D, Inc., 2003a). The **F** vector is the term in the above equation that accounts for the non-linearity in the system. The **R** load vector is made up of body forces, concentrated loads, surface forces, and initial stresses as detailed by Bathe (1996). The mass, damping, and stiffness matrices, **M**, **C**, and **K**, taken as constants in this analysis, are defined as:

$$\mathbf{M} = \sum_i \int_{V(i)} \rho_i \mathbf{H}_i^T \mathbf{H}_i dV_i \tag{16a}$$

$$\mathbf{C} = \sum_i \int_{V(i)} \kappa_i \mathbf{H}_i^T \mathbf{H}_i dV_i \tag{16b}$$

$$\mathbf{K} = \sum_i \int_{V(i)} \mathbf{B}_i^T \mathbf{C}_i \mathbf{B}_i dV_i \,, \tag{16c}$$

where the subscript i represents the ith element, ρ_i is the element density, κ_i is the element damping property parameter, $\mathbf{H}_i$ is the element displacement matrix, $\mathbf{B}_i$ is the strain-displacement matrix, $\mathbf{C}_i$ is the elasticity matrix, and V_i is the element volume.

One other aspect that needs to be addressed in order to define the solid model is the degrees of freedom. While all translational degrees of freedom must be included in the analysis, in order to obtain model convergence, all rotational degrees of freedom must be set to zero.

To discretize the governing equations in the finite element method, the type of element must be chosen. All solid components of the VAD and circulatory loop are meshed using 9-noded quadrilateral MITC shell elements. Two assumptions are made in the development of these elements: zero stress is present through the element thickness in the direction perpendicular to the surface, and particles perpendicular to the surface direction remain this way regardless of deformation.

Once the appropriate governing equations, boundary conditions, material properties, elements, and mesh are known, the system of solid equations can be solved. A Full Newton method is used to linearize this system of equations. Details of this method are presented in the ADINA Theory and Modeling Guide (ADINA R & D, Inc., 2003b). The

linear system of equations is solved using a direct sparse solver, similar to the one used to solve the system of fluid equations.

3.4.4 Fluid-Structure Interaction

Once the separate fluid and solid models are defined, they can be solved simultaneously with information transferring between the two models through coincident FSI boundary conditions. Because the solid displacements affect the fluid motion and the applied stress from the fluid effects the solid motion, two-way fluid-structure coupling must be used to solve the governing equations.

For a solution to be obtained along the FSI boundary, dynamic and kinematic compatibility conditions must be satisfied. The kinematic compatibility condition is:

$$\underline{\boldsymbol{d}}_{\mathrm{f}} = \underline{\boldsymbol{d}}_{\mathrm{s}}, \tag{17}$$

where $\underline{\boldsymbol{d}}_{\mathrm{f}}$ and $\underline{\boldsymbol{d}}_{\mathrm{s}}$ are the fluid and solid displacements on the FSI boundary. Note that the underbar will be used throughout this section to denote quantities calculated along the FSI boundary.

With a no-slip wall boundary condition, the above equation leads to the fluid velocity on the FSI boundary being defined as:

$$\underline{\boldsymbol{v}}_{\mathrm{f}} = \dot{\underline{\boldsymbol{d}}}_{\mathrm{s}} \tag{18}$$

The dynamic compatibility condition is:

$$\boldsymbol{n} \cdot \underline{\boldsymbol{\tau}}_{\mathrm{f}} = \boldsymbol{n} \cdot \underline{\boldsymbol{\tau}}_{\mathrm{s}}, \tag{19}$$

where $\underline{\boldsymbol{\tau}}_{\mathrm{f}}$ and $\underline{\boldsymbol{\tau}}_{\mathrm{s}}$ are the fluid and solid stresses on the FSI boundary.

The above condition gives the following relationship for the fluid force acting on the solid elements at the FSI boundary:

$$\underline{\mathbf{F}}(t) = \int h^{\mathrm{d}} \underline{\boldsymbol{\tau}}_{\mathrm{f}} \cdot d\boldsymbol{S}, \tag{20}$$

where h^{d} represents virtual quantities related to the solid displacement.

Once the compatibility conditions have been defined, the governing equations for the FSI problem can be written as:

$$\mathbf{F}[\mathbf{X}] = \begin{bmatrix} \mathbf{F}_f[\mathbf{X}_f, \underline{\boldsymbol{d}}_s(\mathbf{X}_s)] \\ \mathbf{F}_s[\mathbf{X}_s, \underline{\boldsymbol{\tau}}_f(\mathbf{X}_f)] \end{bmatrix} = 0, \tag{21}$$

where $\mathbf{X}$ is the vector containing the solution vectors $\mathbf{X}_f$ and $\mathbf{X}_s$ for the fluid and solid models, respectively. As can be seen from the above equation, the solution to the fluid part of the model depends on solid displacement on the FSI boundary, while the solution of the solid part depends on the fluid stress applied on the FSI boundary.

To solve the above system of equations, an iterative solver is used. In the iterative method, the fluid and solid models are solved separately with information on the FSI boundaries being passed between the two models and iterated until convergence is reached. Convergence is based on previously defined displacement and the stress criteria. Both have associated user-defined tolerances, which control how close the boundary variables have to match for convergence to be reached. To aid in convergence, relaxation factors, λ_d and λ_τ ($0 < \lambda_d, \lambda_\tau \leq 1$), are used for the displacement and stress, respectively.

For iterative coupling, the following steps are used (ADINA R & D, Inc., 2003b):

1. Solve the following system of fluid equations.

$$\mathbf{F}_f\left[\mathbf{X}_f^k, \lambda_d \underline{\boldsymbol{d}}_s^{k-1} + (1-\lambda_d)\underline{\boldsymbol{d}}_s^{k-2}\right] = 0, \tag{22}$$

   where k represents the iteration number.

2. Solve the following system of solid equations.

$$\mathbf{F}_s\left[\mathbf{X}_s^k, \lambda_\tau \underline{\boldsymbol{\tau}}_f^k + (1-\lambda_\tau)\,\underline{\boldsymbol{\tau}}_f^{k-1}\right] = 0 \tag{23}$$

3. Calculate the fluid displacements on the boundary based on the solid boundary displacements. This is given by the equation:

$$\underline{\boldsymbol{d}}_f^k = \lambda_d \underline{\boldsymbol{d}}_s^k + (1-\lambda_d)\underline{\boldsymbol{d}}_s^{k-1} \tag{24}$$

4. Check the displacement and stress tolerances. If the differences in both of these criteria are within the acceptable tolerance, the iteration for the current time step is completed and the iteration for the next time step begins. If not, more iterations, up to the maximum prescribed number, are performed.

In ADINA, the fluid and solid nodes need not line up on the FSI boundary to ensure the proper transfer of information between the fluid and solid models. Where the nodes do not coincide, interpolation is used to calculate the appropriate nodal values to be transferred from the solid to the fluid and from the fluid to the solid. That is, the solid nodal displacements are interpolated to calculate the fluid nodal displacements and the fluid stresses are interpolated to calculate the solid stresses. To ensure the quality of the solution at the FSI boundary, a tolerance in the distance between fluid and solid nodes is defined in ADINA. Whenever the distance becomes too large, a warning message is printed by the ADINA solvers allowing the user to refine the mesh in the required regions. Further details of this method are presented in the ADINA-F Theory and Modeling Guide (ADINA R & D, Inc., 2003b).

3.4.5 Time Integration

Time integration is used to solve the solution at a time $t + \Delta t$ given a solution at time t. For FSI problems in ADINA, a common time integration method is used in solving the fluid and solid equations. ADINA offers two implicit methods, the Euler α-method, which is first order accurate, and the Trapezoidal Rule/Backward-Differentiation-Formula (TR-BDF) method, which is second order accurate. Both of these methods have been used in this research and are described below.

A time integration parameter, α ($0 < \alpha \leq 1$), is used in both methods. For the Euler α-method, the solution to the governing system of equations at time $t + \Delta t$ is:

$$u(t+\Delta t) = u(t) + \Delta t \cdot f\left[u(t+\alpha\Delta t)\right], \tag{25}$$

where $u(t+\alpha\Delta t) = (1-\alpha)u(t) + \alpha u(t+\Delta t)$.

The TR-BDF method subdivides each time step into two sub-time steps. This subdivision, along with the increased order of the time integration method, permits the use of fewer time steps, saving computational time. The formulae for the two sub-time steps used in the TR-BDF method to find the solution at time $t + \Delta t$ are given as:

$$\begin{aligned} u(t+\gamma\Delta t) &= u(t)+\gamma\Delta t\cdot f\left[u\left(t+\tfrac{1}{2}\gamma\Delta t\right)\right] \\ u(t+\Delta t) &= u(t+\beta\gamma\Delta t)+(1-\alpha)\Delta t\cdot f\left[u(t+\Delta t)\right] \end{aligned} \tag{26}$$

where $\gamma = 2-1/\alpha$, $\beta = \alpha^2/(2\alpha-1)$, and $u(t+\beta\gamma\Delta t) = (1-\beta)\,u(t)+\beta u(t+\gamma\Delta t)$ (ADINA R & D, Inc., 2003b).

For the Euler α-method, a commonly used value of α is 1, which is the Euler backwards time integration method, while for the TR-BDF method, α is usually taken as $1/\sqrt{2}$.

3.4.6 Arbitrary-Lagrangian-Eulerian (ALE) Method

The motion of fluids and solids can be described in two ways, Lagrangian and Eulerian. In the Lagrangian formulation, the motion of particles is tracked in space, while in the Eulerian formulation, a fixed volume is observed as particles move through it.

What this means in finite element analysis is that, in the Lagrangian formulation, the material points are fixed to the mesh, while, in the Eulerian formulation, the material points move through a fixed mesh (Bathe, 1996). For this reason, the Lagrangian formulation is typically used for solids, while the Eulerian formulation is used for fluids.

A problem arises, however, in the use of a purely Eulerian formulation for a fluid model containing moving boundaries, as the fixed mesh through which the particles move is also moving. In this case, a hybrid formulation known as the Arbitrary-Lagrangian-Eulerian (ALE) method is appropriate (Bathe, 1996). In this method, the Eulerian formulation is used at fixed boundaries, the Lagrangian formulation is used at moving boundaries, and the ALE formulation is used in between.

In the governing equations of the ALE formulation, the actual fluid velocity with respect to a fixed mesh is replaced by a relative velocity relating the actual fluid velocity to the mesh velocity. In doing so, the continuity equation for slightly compressible flow and the momentum equation are modified as shown below:

$$\frac{\rho}{\kappa}\left(\frac{\partial p}{\partial t}+(v-w)\cdot\nabla p\right)+\rho_{\mathrm{m}}\nabla\cdot v=0 \tag{27}$$

$$\rho\frac{\partial v}{\partial t}+\rho(v-w)\cdot\nabla v-\nabla\cdot\tau=f^{B}, \tag{28}$$

where w is the mesh velocity vector.

3.5 Geometry

The geometry in this research consists of two major components, the VAD and a model of the circulatory system. Simulations are performed on the VAD alone (open loop) and with the VAD connected to a circulatory system model (closed loop). Details of these geometries are presented below.

The VAD geometry used in this research consists of two hemispherical chambers separated by a circular diaphragm. The lower chamber contains water as the driving fluid and has a single inlet/outlet tube. The upper chamber is the blood chamber, whose dimensions are based on the BU-VAD. To design the blood chamber, the diameters of the chamber and the inflow and outflow tubes were taken from the BU-VAD as 140 mm and 38 mm, respectively (König & Clark, 2001). Note that the BU-VAD was scaled to twice the size of an actual VAD to aid in flow visualization of their experimental model and that this scaling has been used in the current model as well.

To define the rest of blood chamber geometry, three additional dimensions were required: x^*, the distance between the centres of the inflow and outflow tubes; y^*, the distance from the centre of the hemisphere to the end of the inlet and outlet tubes; and z^*, the distance from the bottom of the hemisphere to the centre of the inlet and outlet tubes. To obtain these dimensions, measurements were made from two two-dimensional drawings of the BU-VAD using the known measurements to calculate the scale. From Figure 1 of

König and Clark (2001), $y^* = 157$ mm and $z^* = 42$ mm and from their Figure 3a, $x^* = 60$ mm. These dimensions are labelled on the blood chamber geometry shown in Figure 12.

As no driving fluid chamber exists in the BU-VAD, we were free to select a design that complements the blood chamber design. The driving fluid chamber was taken to be a hemisphere with the same diameter as the blood chamber. Unlike the blood chamber, the driving fluid chamber was given a single inlet/outlet tube, which is 80 mm long from the centre of the hemisphere, parallel to the blood chamber inlet/outlet tubes, and has a diameter of 38 mm. The solid portion of the VAD geometry consists of the circular diaphragm, with a diameter of 140 mm and negligible thickness. Both the fluid and solid geometries can be seen in Figure 13.

For the closed loop computations, a circulatory system model is defined to connect the inlet and outlet tubes of the VAD blood chamber (Figure 14). It consists of three components, two elastic cylindrical tubes, used to model the total arterial and venous compliances, and a porous medium, used to model peripheral resistance. The two elastic tubes are cylindrical with lengths of 95 mm and diameters of 38 mm and the porous medium is a rectangular prism that is 40 mm high, 90 mm long, and 100 mm wide.

To orient the geometries in space, a co-ordinate system and origin must be defined. These co-ordinates and origin location will be used throughout this thesis. The origin is defined to be at the centre of the undeformed diaphragm separating the two fluid chambers, and the co-ordinate system is shown in Figure 12.

3.6 Boundary Conditions

3.6.1 Fluid

For the fluid geometry, no-slip boundary conditions are applied to all fixed walls except those of the porous medium, where slip boundary conditions are applied. For the no-slip wall boundary condition, the velocity vector at the wall is equal to zero, while, for the slip boundary condition, only the normal component of the velocity at the wall is zero.

FSI boundary conditions are defined along the circular surfaces that join the two hemispherical VAD chambers as well as the walls of the compliant tubes. These FSI boundaries must match up with corresponding FSI boundaries in the solid model for the FSI analysis to run properly.

Instantly opening and closing valves are modelled at the ends of the VAD inlet and outlet tubes. Two different techniques were used in ADINA to model these valves in the open and closed loop cases. For the open loop case, a zero velocity condition is used to mimic a closed valve. This zero velocity condition is applied and removed at fixed times during the cycle using the element birth-death option in ADINA. For the closed loop case, gap boundary conditions were applied. Gap boundaries act as no-slip walls when they are closed, and allow fluid to flow freely through them when they are open. The opening and closing of these gaps are controlled by time functions. In both the open and closed loop cases, the valves are opened and closed when the diaphragm deformation is at its highest and lowest points, with both valves being opened for two time steps at these points to prevent model divergence.

A time-dependent pressure function is applied at the inlet of the water chamber to drive the motion of the diaphragm, which, in turn, moves blood around the closed loop. To implement this pressure function, a normal-traction boundary condition is used. This condition is applied to the boundary nodes as a force on the right-hand side of the momentum equation. It is defined as:

$$\mathbf{F}(t) = \int h^{v} \bar{\tau}_{nn}(t) dS \tag{29}$$

where h^{v} is a virtual quantity of the boundary velocity and $\bar{\tau}_{nn}(t) = \boldsymbol{n} \cdot \boldsymbol{\tau} \cdot \boldsymbol{n}$ is the normal traction. This normal traction consists of two components, pressure and normalized deviatoric stress. The normalized component of the deviatoric stress is negligible along open boundaries, such as the one in this model and, as a result, this boundary condition is recommended for use at locations where the pressure is known on the boundary. The pressure function chosen for this model is sinusoidal with a maximum amplitude of 215 MPa and a period of $T = 3.64$ s. This period, equivalent to 16.5 heartbeats per minute, is

based on the scaling done by König and Clark (2001) to match a heart rate of 66 heartbeats per minute in the actual human body.

An input pressure variation was chosen as a means for flow forcing, rather than the more realistic input velocity variation. It is reminded that, because pressure appears only in a gradient term in the Navier-Stokes equations, the pressure value resulting from the solution of these equations can only be found as the difference from a reference value at some point in the flow domain. Thus, it is necessary to specify such a reference pressure at all times during the cycle. For the open loop case, this requirement would be satisfied by setting the pressure at the distal ends of the inlet and outlet tubes of the blood chamber to zero throughout the cycle. However, for the closed loop case, it is not possible to define a constant reference pressure, because the pressure varies with time at all points in the flow domain. Therefore, the only way to obtain pressure values in the closed loop model was to specify the pressure variation at the distal end of the inlet/outlet tube of the driving fluid chamber. For uniformity, we used the same condition for both the open and closed loop cases.

Figure 15 shows the variation of the input pressure function along with the corresponding displacement of the centre of the diaphragm for a single period. The sequencing of the inlet and outlet valves is shown at the bottom of this figure. Note that there are two time steps near $t = 0.25T$ and $0.75T$ at which both valves are open.

3.6.2 Solid

For the solid model, FSI boundary conditions are specified on all solid surfaces. Due to the fluid-structure-fluid interaction of the diaphragm, two FSI boundaries must be specified on the diaphragm. In addition to the FSI boundary conditions, special conditions, called "fixities" in ADINA, are used to anchor the solid geometries, preventing them from moving downstream with the fluid flow. Fixities allow the user to apply zero conditions at specified locations on a geometry. In this case, fixities are applied to the outside edges of all solid geometries, fixing all rotations and translations for these edges.

3.7 Material Models and Parameter Values

3.7.1 Fluid

Two fluids are used in this model, water, for the external VAD chamber and blood, for the internal VAD chamber and the circulatory system model. Both of these fluids are modelled as Newtonian, with constant material properties. While blood is a non-Newtonian fluid, non-Newtonian effects are negligible in large vessels (Pedley, 1980) and devices such as VADs. To fully define the material properties of these fluids, the following parameters are needed: density, viscosity, bulk modulus of elasticity (for slightly compressible fluid only), and the gravitational acceleration vector.

A gravitational acceleration vector of 9.81 m/s^2 in the negative z-direction is used in this model. This coincides with the orientation of the BU-VAD. The values for the remaining parameters are given in Table 3-1. For water, parameter values were taken at 20°C, with the bulk modulus of elasticity taken several orders of magnitude higher than actual values to limit compressibility. The blood density and viscosity values were chosen to match the properties of the fluid used in the BU-VAD model. This viscosity value is the high-shear viscosity at 37°C (König *et al.*, 1999a). To limit the compressibility of the blood around the closed loop, the bulk modulus of elasticity has been increased to the maximum value for which a solution could be obtained.

Table 3-1. Fluid material parameter values.

Material	Water	Blood
Density, ρ (kg/m^3)	999	1105
Viscosity, μ (kg/m·s)	1×10^{-3}	4.66×10^{-3}
Bulk Modulus of Elasticity, κ (kN/m^2)	1×10^{10}	1×10^{5}

3.7.2 Porous Medium

For the porous medium, material properties of both the fluid and solid must be specified. The fluid flowing in the porous medium is blood with the same material properties given previously in Table 3-1. To define the material properties of the solid portion of the

porous medium, the solid density, porosity, and specific permeability tensor are needed. The solid density has been set to match the blood density of 1105 kg/m^3. The specific permeability tensor has been defined as isotropic, with a value of 1×10^{-4} m^2, and the porosity has been set at 1 %.

3.7.3 Solid

The two flexible tubes and the diaphragm have been modelled using separate linear elastic material models. The parameters necessary to define each of these materials are the Young's modulus, E, the Poisson ratio, ν, and the solid density, ρ_s. All three materials are essentially incompressible, which would imply a Poisson ratio of 0.5. However, in ADINA, strictly incompressible materials cannot be defined, so the Poisson ratio has been set to 0.495 to approximate an incompressible material. The densities of all solid materials have been defined as 1000 kg/m^3 to approximate the densities of the fluids used. The Young's modulus of each material has been adjusted to give the desired deformation. For the diaphragm, $E = 1\times10^8$ kN/m^2 and for the elastic tubes, $E = 7.5\times10^4$ kN/m^2. The Young's modulus value for the elastic tubes has been chosen to be less than the fluid bulk modulus value to allow the walls to expand and contract. Having a Young's modulus value greater than the bulk modulus of the fluid prevents wall motion.

CHAPTER 4

RESULTS AND DISCUSSION

4.1 Simulation Setup

Simulations were performed for the two previously defined configurations, open and closed loop. In both cases, several periods were run in an attempt to reach a periodic solution. Visualization results and quantitative results will be presented for each configuration in the sections to follow. Initially, all fluid inside the blood and driving fluid chambers were at rest, requiring a full period to be run to initialize the system properly. For each period, 520 time steps were simulated with the results being saved every 13 time steps.

For the open loop case, two fluid and two solid mesh densities were simulated. These mesh densities will be referred to as "coarse" and "fine". For the solid, the coarse mesh contained 1649 nodes and 792 elements and the fine mesh contained 3081 nodes and 1496 elements as shown in Figure 16. For the fluid, the coarse mesh contained 13 711 nodes and 66 742 elements and the fine mesh contained 24 998 nodes and 126 967 elements, as shown in Figure 17.

For the closed loop case, simulations were only done for one mesh density, which was based on the "coarse" mesh used for the open loop case. This mesh consists of 19 300 nodes and 92 737 elements, as shown in Figure 18. Due to an identified error in ADINA

code, for which there is currently no correction, we were unable to run the closed loop simulations with a finer mesh density.

Initially, closed loop simulations were attempted using the TR-BDF time integration method previously described in Section 3.4.5; however, this approach would not lead to convergence. For this reason, an initial period was run using the less accurate Euler time integration method. Once the initial period was complete, subsequent periods were run using the TR-BDF method. In order to achieve convergence with the Euler time integration method, 1040 time steps were used for the initial period. Once the TR-BDF method could be used, the number of time steps was reduced to 520 per period to coincide with the number of steps in the open loop case.

For the fluid model, nodal results at six locations are used for comparisons between mesh densities, periods, and configurations, as well as comparisons to the BU-VAD results. All of these "control" nodes are located inside the blood chamber as shown in Figure 19. The co-ordinates of the control nodes are given in Table 4-1 for both mesh densities along with the type of value saved at each node. Note that, due to the unstructured nature of the fluid mesh, nodal locations differ slightly between the two mesh densities. In addition, due to mesh deformation, nodes *d*, *e*, and *f* move throughout the cycle with maximum displacement magnitudes of 0.87, 3.3, and 5.4 mm, respectively. The largest maximum displacement among those three nodes (5.4 mm) corresponds to less than 4% of the chamber radius. Because ADINA does not provide values at fixed geometrical locations, it was decided to disregard nodal displacement at this phase of the study.

Four of the control node locations, *a, d, e,* and *f*, were chosen as points for comparison to the published BU-VAD data. The other two control nodes, *b* and *c*, which are located at the centre of the ends of the blood chamber outlet and inlet tubes, were chosen because they were expected to be the points where the maximum local Reynolds number would occur.

For the solid model, control node and element results on the diaphragm are used for comparisons between mesh densities. The co-ordinates of the five control nodes used for comparison are given in Table 4-2. The five elements chosen each have one of the chosen nodes as a vertex. The locations of these elements and nodes on the diaphragm for both mesh densities can be seen in Figure 20. Note that each element in Figure 20 contains nine nodes, which makes the density of the diaphragm mesh finer than it appears to be.

Table 4-1. Fluid nodes chosen within blood chamber for comparisons.

Label	Coarse Mesh (mm)			Fine Mesh (mm)			Type of Value
	x	*y*	*z*	*x*	*y*	*z*	
a	0	0	70	0	0	70	Pressure
b	30	157	41	30	157	40	Velocity Magnitude
c	-30	157	41	-30	157	40	Velocity Magnitude
d	-1.5	-54	37	2.5	-53	42	*x*-velocity
e	-5.5	-37	42	2.0	-39	43	*x*-velocity
f	3.5	-26	40	4.4	-25	43	*x*-velocity

Table 4-2. Solid nodes chosen on diaphragm for comparisons.

Label	*x* (mm)	*y* (mm)	*z* (mm)
1	0	0	0
2	0	35	0
3	35	0	0
4	0	-35	0
5	-35	0	0

4.2 Open Loop VAD Model

To compare results with those found using the BU-VAD, simulations of the VAD were carried out without the circulatory loop. Due to the difference in flow forcing between the two models, this comparison will be mainly qualitative, with quantitative comparisons being concerned with order-of-magnitude agreement. To match the BU-

VAD ejection volume of 480 mL, the Young's modulus of the diaphragm and the amplitude of the sinusoidal pressure function were varied. It was found that the ejection volume depends on the ratio of the Young's modulus of the diaphragm and the amplitude of the sinusoidal pressure function. It was also realized that the lower the magnitude of each of the parameters was, the more difficult it became to obtain model convergence, especially with the TR-BDF time integration method. Because of this limitation, relatively large values, 1×10^8 kN/m^2 for the Young's modulus and 215 MPa for the maximum inlet pressure, were used in the simulations. While these values are much larger than those in the actual system, it is important to note that, because the flow in the VAD is only dependent on the ratio of these two values, their individual magnitudes are not of great significance.

4.2.1 Flow Description

Visualizations of the pressure and velocity inside the blood chamber are shown in Figure 21 to Figure 23, and effective stress values for the solid diaphragm are shown in Figure 24 and Figure 25. These results correspond to the second period of simulations with the fine fluid and solid mesh densities. Figure 21 shows the diaphragm deformation and blood velocity vectors on a plane at $x = 0$. To reduce the size of the simulation output, velocities in the water chamber were not saved during the computations. Note that all velocity vectors have been assigned the same length, with the velocity magnitude indicated by colour only. Velocities with values higher than or equal to 0.28 m/s have been plotted with the same colour to improve visualization of the results at lower velocities. Figure 22 shows the velocity vectors on a plane at $z = 42$ mm. In this figure, velocities with values higher than or equal to 0.84 m/s have been plotted with the same colour. Figure 23 shows pressure band plots on the same plane as the previous figure. The pressure bands have been truncated at +/- 0.525 kPa, such that pressures equal to or exceeding these values are shown in the same colour. Note that the external pressure is set to zero, so that, when a valve is open, the pressure inside the VAD is taken relative to the zero pressure outside. Figure 24 shows a side view of the effective stress in the diaphragm over one period and Figure 25 shows the same effective stress in a top view.

In both of these figures, the effective stress has been truncated at a maximum value of 4.16×10^7 kN/m^2.

Prior to discussing quantitative results, a qualitative look at the flow patterns inside the blood chamber will be presented. At the start of the period, the diaphragm is in its undeformed state, the outlet valve is open, and the inlet valve is closed. Water is forced into the water chamber deforming the membrane upwards and forcing blood out of the blood chamber. The velocity in the outlet tube is initially large, with the velocity increasing towards the outer wall of the tube. As the diaphragm continues to move upward, a recirculation region forms near the inner wall of the outlet tube, where fluid enters the outlet from the exterior. We believe that this backflow is particular to the idealized geometry used in this simulation, in which no effort was made to streamline the blood chamber design and in which the VAD inlet and outlet are connected to an infinitely large reservoir. As high speed fluid rushes into the outlet tube non-axisymmetrically, it separates and generates a three-dimensional, unsteady, recirculating vortex, which entrains fluid from the open reservoir. It is believed that this backflow could be eliminated in an optimized VAD configuration. Furthermore, its magnitude would likely be reduced by connecting the VAD in a closed loop. This issue will be further discussed in following sections.

At one time step before $t = 0.25T$, the inlet valve opens followed at $t = 0.25T$ by the closing of the outlet valve as the diaphragm reaches its highest displacement. As the diaphragm moves down, blood flows into the inlet tube. Initially, the peak velocity is at the centre of the tube, but this velocity is gradually drawn downward towards the inner wall. As with the outlet tube, this creates a region of backflow, but in this case, it is near the outer wall.

During the filling stage, the largest velocity in the blood chamber occurs around the outside of the chamber as the fluid moves counter-clockwise around the outside wall. This fluid movement continues until one time step before $t = 0.75T$, when the outlet valve opens. At $t = 0.75T$, when the diaphragm is at its lowest point, the inlet valve closes and

fluid begins flowing out of the VAD again as the diaphragm moves back towards its undeformed state.

4.2.2 Mesh Studies

Simulations were done for two different fluid and solid mesh densities, as defined in Section 4.1, to examine the effect of the mesh density on the quality of the solution. During the solution process, the majority of computational time is spent solving the fluid equations. As a result, the solid mesh can be refined without significantly affecting the computational time. For this reason, the solid and fluid meshes were refined independently.

The solid mesh study was performed for one period with the coarse fluid mesh to reduce the necessary computational time. To compare results corresponding to these meshes, both nodal and elemental results have been saved at the five control locations previously described. For the nodes, the quantity of interest is displacement, while, for the elements, effective stress values were used for comparison. In both cases, results at each location were saved every thirteen time steps, for a total of forty values per period. The absolute difference between mesh densities was calculated for each location. The minimum, average, and maximum absolute differences for each control node and element are presented in Table 4-3 and Table 4-4, respectively.

Table 4-3. Comparison of nodal displacements for two solid mesh densities.

Node	Minimum Absolute Difference	Average Absolute Difference	Maximum Absolute Difference
1	2.0×10^{-7} mm	1.5×10^{-2} mm	2.1×10^{-2} mm
2	1.1×10^{-7} mm	8.3×10^{-3} mm	1.2×10^{-2} mm
3	1.2×10^{-7} mm	8.4×10^{-3} mm	1.2×10^{-2} mm
4	1.3×10^{-7} mm	9.1×10^{-3} mm	1.3×10^{-2} mm
5	1.2×10^{-7} mm	8.2×10^{-3} mm	1.2×10^{-2} mm

Excellent agreement between simulations with different mesh densities can be seen for the nodal displacements presented in Table 4-3. For the six control nodes, the maximum difference in nodal displacements for two different mesh densities was 0.021 mm, which is about 0.1% of the maximum displacement of 29 mm.

Table 4-4. Comparison of elemental effective stress values for two solid mesh densities.

Element	Minimum Absolute Difference	Average Absolute Difference	Maximum Absolute Difference
1	2.9 kN/m^2	2.7×10^4 kN/m^2	5.5×10^4 kN/m^2
2	2.6 kN/m^2	2.5×10^5 kN/m^2	3.1×10^5 kN/m^2
3	2.8 kN/m^2	2.4×10^5 kN/m^2	3.1×10^5 kN/m^2
4	1.7 kN/m^2	2.5×10^5 kN/m^2	3.1×10^5 kN/m^2
5	2.9 kN/m^2	2.5×10^5 kN/m^2	3.1×10^5 kN/m^2

Prior to examining the elemental results, it should be noted that the area of each element differs between mesh densities, with the elements in the coarse mesh having an area of approximately 21 mm^2 compared to 11 mm^2 for the fine mesh. However, due to the way the solid results are saved in ADINA, stress values are only available for elements, and not nodes. Because of this area difference, spatial differences in stress will be included in the differences in element results. Even with these small spatial differences, excellent agreement can be seen between the elemental results in the two meshes. While the maximum effective stress difference of 3.1×10^5 kN/m^2 in Table 4-4 might seem like a large discrepancy, it is actually small in relative terms. When this value is divided by the maximum effective stress of 3.5×10^7 kN/m^2, a percent difference of 0.9 % is found.

In view of the small percent differences in the results with the two solid mesh densities, it is evident that further refinement of the solid mesh is not required. Therefore, for the rest of the computations, the previously identified "fine" solid mesh density will be used.

With the solid mesh density fixed, the effect of refinement of the fluid mesh density will be investigated. In addition to the two fluid mesh densities defined in Section 4.1, a third "superfine'' fluid mesh of approximately 40 000 nodes was considered. While the computational resources are available on HPCVL to run simulations with the superfine mesh density, computational time must also be considered. A single period with the fine fluid mesh takes the order of a week to run on HPCVL, but the same period requires about one month with the superfine mesh. Because it was determined to be more desirable to simulate multiple periods than have excellent mesh refinement, simulations with the superfine fluid mesh were not pursued.

The two fluid mesh densities are compared at the control nodes both graphically and quantitatively for the fourth period of simulation. In Figure 26 to Figure 31, the quantity of interest (pressure or velocity) at each control node is plotted as a function of normalized time for both mesh densities. For a quantitative comparison, the absolute difference at each of the six control nodes was calculated for each of the forty saved time steps. The minimum, average, and maximum absolute differences for each node are presented in Table 4-5. Note that, for nodes *b* and *c*, the time steps for which the valve was closed, forcing the fluid velocity to zero, were removed from the values used in calculations.

Table 4-5. Comparison of nodal values between the two fluid mesh densities.

Point	Minimum Absolute Difference	Average Absolute Difference	Maximum Absolute Difference
a	0.003 kPa	0.237 kPa	1.273 kPa
b	0.003 m/s	0.168 m/s	0.509 m/s
c	4.9×10^{-4} m/s	0.476 m/s	1.770 m/s
d	6.6×10^{-4} m/s	0.035 m/s	0.144 m/s
e	0.002 m/s	0.056 m/s	0.190 m/s
f	1.5×10^{-4} m/s	0.026 m/s	0.099 m/s

Before discussing the differences in pressures and velocities between simulations with the two mesh densities, it should be noted that the nodes being used, while close in location, do not precisely coincide in both models. As a result, slight spatial differences exist between the two meshes.

When comparing the pressures at node *a* for the two mesh densities, the major differences occur at the two minima of the pressure wave, as can be seen in Figure 26. At the first minimum, the pressure for the fine mesh is lower than for the coarse mesh, and the reverse is true for the second minimum.

The velocities at node *b* agree fairly well for the two meshes. The only time when a large difference occurs is at $t = 0.825T$, for which the peak velocity for the fine mesh is much larger than for the coarse mesh. A similar peak is seen at node *c*, where, for $0.3T < t < 0.4T$, the velocity for the fine mesh is much larger than for the coarse mesh. With this exception, agreement between the simulations with the two meshes is good at node *c*. In both of these cases, the most significant differences in velocity magnitudes occur shortly after the valve has opened.

As can be seen in Figure 29 to Figure 31, *x*-velocities for the two fluid meshes agree well at nodes *d*, *e*, and *f*. Small differences at these locations can be partially accounted for by spatial differences, as all three nodal locations differ slightly in the two meshes. For nodes *e* and *f*, large differences can be seen near $t = 0.75T$. At node *e*, the *x*-velocities for the fine mesh are negative, while the *x*-velocities for the coarse mesh are positive, and, at node *f*, the *x*-velocities are much larger for the fine mesh than for the coarse mesh. These differences suggest that additional flow features are being captured by the fine mesh that are missed by the coarse mesh. Additional mesh refinement would further clarify the flow patterns at these locations.

Although the mesh dependence studies are not entirely conclusive, because we only considered two fluid mesh densities due to time considerations, they may still be used for some conclusions. Based on the overall similarity between the waveforms at the control

nodes, it is reasonable to believe that these waveforms would be representative of simulations with an even finer mesh. However, the appearance of spikes in the fine mesh results that are not seen in the coarse mesh results suggests that further mesh refinement is needed to capture the flow patterns at these locations. Considering that the objective of the present study is to demonstrate the feasibility of this approach and not to produce extremely accurate calculations, we conclude that results using the "fine" fluid mesh are of acceptable quality.

4.2.3 Periodicity

The desired solution to this problem is one that is truly periodic with no dependence on the initial conditions. However, the number of periods required to achieve a periodic solution cannot be known in advance. Therefore, comparisons must be made over multiple periods to determine whether a periodic solution has been reached. In this section, results at each of the six control nodes are compared for several periods for both mesh densities. Because the computational time required to run the coarse mesh is much less than the time required to run the fine mesh, more periods can be run with the coarse mesh over the same length of computational time.

For the coarse mesh, eight periods have been run. For each control node, the quantity of interest is plotted versus normalized time for all periods to allow a graphical comparison of the results (see Figure 32 to Figure 37). For a quantitative comparison, the average absolute differences between periods for each control node are presented in Table 4-6. As in the mesh study, times at nodes *b* and *c* when the valve is closed, making the velocity zero, have been removed from the average absolute difference calculations.

At the start of the first period of simulation, all of the fluid in the blood chamber was taken to be at rest. It is clear from Figure 35 to Figure 37, which represent flow inside the blood chamber, that the initial x-velocity value at these locations for all periods after the first one is not zero. As a result, it is necessary to run at least one period to initialize the system. This can also be seen in Table 4-6, in which the average differences between

the first and second periods are all larger than those for subsequent periods. As a result, only the differences between the second and subsequent periods will be examined.

For node *a*, excellent agreement is seen from the second to the eighth periods with the exception the values at $t = 0.225T$ and $0.25T$. A similar discrepancy is found when examining the results at node *b*, however the scatter is spread from $t = 0.175T$ to $t = 0.25T$. Smaller differences can also be seen at node *b* in the range $0.8T < t < 0.9T$.

Table 4-6. Comparison of fluid nodal results between periods with the coarse mesh.

	Average Absolute Difference			
Point	**Period 1 – Period 2**	**Period 2 – Period 3**	**Period 3 – Period 4**	**Period 4 – Period 5**
a	0.054 kPa	0.022 kPa	0.010 kPa	0.012 kPa
b	0.173 m/s	0.132 m/s	0.030 m/s	0.061 m/s
c	0.009 m/s	4.1×10^{-4} m/s	0.003 m/s	1.9×10^{-4} m/s
d	0.043 m/s	0.001 m/s	4.4×10^{-4} m/s	5.4×10^{-4} m/s
e	0.050 m/s	0.002 m/s	0.001 m/s	0.001 m/s
f	0.010 m/s	0.003 m/s	3.9×10^{-4} m/s	3.2×10^{-4} m/s

	Average Absolute Difference		
Point	**Period 5 – Period 6**	**Period 6 – Period 7**	**Period 7 – Period 8**
a	0.006 kPa	0.020 kPa	0.011 kPa
b	0.072 m/s	0.132 m/s	0.048 m/s
c	1.0×10^{-4} m/s	2.8×10^{-4} m/s	1.7×10^{-4} m/s
d	4.1×10^{-4} m/s	9.8×10^{-4} m/s	5.9×10^{-4} m/s
e	4.4×10^{-4} m/s	0.001 m/s	7.2×10^{-4} m/s
f	2.7×10^{-4} m/s	5.7×10^{-4} m/s	4.7×10^{-4} m/s

Node *c* is on the boundary of the end of the inlet tube and therefore has a specified zero velocity at the times where differences at node *b* are the largest. This may help to contribute to the much better overall agreement between periods at node *c*. Excellent agreement is also seen between periods at nodes *d* and *e*, both graphically and in terms of average differences. Good agreement is also seen between periods at node *f*, however,

slightly more scatter is present than at nodes *d* and *e* as can be seen in Figure 37. While this is not as clear in the average absolute difference calculations, it should be noted that the magnitude of the *x*-velocities at node *f* are smaller than those for nodes *d* and *e*, leading to a larger percent difference.

To summarize, the areas of most concern in the periodicity study for the coarse mesh are nodes *a* and *b* during the lead up to the highest diaphragm displacement. More periods need to be run for these results to ensure convergence to a periodic solution.

For the fine mesh, fewer periods were run due to the increased computational time required compared to that for the coarse mesh calculations. Plots of these results at nodes *a-f* are presented in Figure 38 to Figure 43 and quantitative comparisons between periods are given in Table 4-7. As with the coarse mesh results, a noticeable drop is seen in the average absolute difference values between the second and third period, compared to the values for the first and second periods. As it has been previously established that the first period must be run to initialize the system, the discussion of the periodicity results for the fine mesh will be limited to a comparison between the second, third, and fourth periods.

Table 4-7. Comparison of fluid nodal results between periods with the fine mesh.

	Average Absolute Difference		
Point	**Period 1 – Period 2**	**Period 2 – Period 3**	**Period 3 – Period 4**
a	0.046 kPa	0.009 kPa	0.007 kPa
b	0.131 m/s	0.005 m/s	0.002 m/s
c	0.109 m/s	0.058 m/s	0.043 m/s
d	0.041 m/s	0.004 m/s	0.003 m/s
e	0.057 m/s	0.006 m/s	0.003 m/s
f	0.017 m/s	0.003 m/s	0.001 m/s

Excellent agreement between periods two, three, and four can be seen for nodes *a* and *b*. The regions of scatter present with the coarse mesh density at these nodes are absent for the fine mesh. The opposite is true for node *c*. While there was very little scatter for the coarse mesh at node *c*, large scatter is present in the range $0.25T < t < 0.5T$ for the fine

mesh results. This scatter leads to an average absolute difference that is about ten times larger than those found for the other nodes.

For nodes *d-f*, good agreement exists between periods two, three, and four. The scatter that is present is generally during the middle of the period, beginning shortly after the end of the scatter seen at node *c*. This scatter, similar to that observed at node *c*, suggests that additional periods should be run with the fine mesh for the solution to approach a periodic state.

4.2.4 Comparison to Previous Research

As mentioned in Section 2.5, three quantitative results from the BU-VAD can be used for validating the current VAD model. These are the maximum Reynolds number at the distal end of the VAD inlet and outlet tubes, the pressure at the VAD apex, and the *x*-velocity at three locations in the VAD. A discussion of and comparison to these results is made below.

To begin comparing the current results to previous research, the maximum Reynolds numbers at the distal ends of the blood chamber inlet and outlet tubes will be examined. For the BU-VAD, the maximum Reynolds number is $Re_{max} = 3300$ (König *et al.*, 1999b), while for the current VAD, $Re_{max} = 4085$. In both cases, the maximum Reynolds number occurred at $t = 0.5T$ and $t = T$. In this context, the Reynolds number was defined as $Re = \rho VD/\mu$, where ρ and μ are the density and viscosity of blood previously defined in Table 3-1, V is the average velocity over the tube cross-section, and D is the diameter of the inlet/outlet tubes. Given that ρ, μ, and D are the same in both models, differences in Reynolds numbers are equivalent to differences in the average velocity. Furthermore, because the cross-sectional area of the tubes is the same in both models, differences in average velocity are equivalent to differences in volumetric flow rate. These differences will be discussed below.

To account for the differences in volumetric flow rate, we must first examine the temporal variation of blood volume inside the blood chamber. The diaphragm material

properties and input pressure magnitudes have been calibrated so that the maximum volume displaced in each cycle in the current VAD matches that in the BU-VAD studies. The input pressure function in the present model is sinusoidal in time. However, the waveform of the volume displacement deviates from the sinusoidal BU-VAD volume displacement waveform, as can be seen in Figure 44, in which the corresponding curve has been fitted to forty volume displacement values from simulations with the "fine" fluid mesh density.

As mentioned above, to calculate the maximum cross-sectional average velocity for the Reynolds number calculation, the maximum volumetric flow rate is used. To calculate the volumetric flow rate, the volume displacement curve is differentiated with respect to time. This was done by calculating the change in volumetric flow rate divided by the change in time for the forty intervals between the saved results. The resulting curve is shown in Figure 45. It is clear from this curve that the maximum volumetric flow rate is larger in the current VAD than in the BU-VAD, and this difference leads to the difference in Reynolds numbers.

To compare the pressure values at the apex of the VAD and the x-velocity values at three locations inside the current VAD to the BU-VAD results, graphs of the BU-VAD results had to be generated. The pressure results at the apex of the BU-VAD were approximated from Figure 5 in König and Clark (2001) and the x-velocity results were approximated from Figure 8 in König *et al.* (1999b).

The normalized pressure at node *a* for the third period of simulation with the fine mesh is plotted in Figure 46, along with the normalized BU-VAD pressures. The pressure magnitudes of these results were normalized by their respective maxima to account for the difference in order of magnitude between current and previous results. The pressures in the BU-VAD are of the order of 0.1 kPa, while the pressures in the current VAD are of the order of 1 kPa.

Poor agreement between the BU-VAD pressures and the current VAD pressures can be seen in Figure 46, not only in magnitude, but also in the shape of the curves. While the BU-VAD pressure curve has a single minimum and maximum, the pressure in the current VAD has two minima and maxima. We believe that one of the causes of the difference in the pressure waveforms between the two models is the difference in flow forcing.

For the x-velocity comparisons, the locations at which the BU-VAD results are available have been approximated from Figure 7 in König *et al.* (1999b), using the known inlet/outlet tube diameter to calculate the scale. The x and z locations of these points have been given as 0 and 42 mm respectively, leaving only the y location to be approximated. The approximate co-ordinates of these points are d' (0, -53 mm, 42 mm), e' (0, -38 mm, 42 mm), and f' (0, -25 mm, 42 mm). These three locations have been approximated by nodes d, e, and f in the current model for comparison. Plots of the x-velocity at each of these three locations are shown in Figure 47 to Figure 49, along with the corresponding results from the BU-VAD. In view of the approximate matching of the nodal locations in the current model and the BU-VAD, as well as differences in flow rate waveforms and flow forcing, close quantitative agreement between the results of the two models should not necessarily be expected.

In Figure 47, all three velocity waveforms begin at a low value, increase to a maximum and then return to the initial low value. However, the maximum velocity in the current VAD has a larger magnitude and occurs slightly earlier in the cycle than the maximum velocity in the BU-VAD cases. This shifting could be accounted for by spatial differences and the magnitude difference can be accounted for by the larger pressure gradient and flow rate in the current VAD model.

At node e, as shown in Figure 48, the BU-VAD x-velocities both increase from zero towards a maximum before decreasing to around 0.005 to 0.007 m/s. The x-velocity waveform in the current VAD initially follows the BU-VAD waveforms at a higher velocity, but differs from the BU-VAD results over the interval $0.7T < t < 0.875T$. Within this interval, results from the current VAD model show the x-velocity declining

from 0.10 m/s to a minimum of -0.08 m/s and then increasing to 0.07 m/s, while the results for the BU-VAD remain around 0.05 to 0.07 m/s. This suggests that a flow pattern is present in the current model that is different from that in the BU-VAD.

For node *f*, three different waveforms can be seen in Figure 49. Large differences are present in the *x*-velocities for the BU-VAD experimental and computational results. A third *x*-velocity waveform can be seen for the results of this study. The waveform for the current VAD study resembles that for the BU-VAD CFD results, but with magnitudes that are larger and shifted to earlier times. Note that the magnitudes of the *x*-velocities at node *f* are smaller than those at nodes *d* and *e*, making it more difficult to get agreement between models. In addition, the agreement between the BU-VAD experimental and computational results is not as good as the agreements at nodes *d* and *e*, which possibly suggests a reduced accuracy at this nodal location.

4.2.5 Particle Traces

One important criterion in the design of a VAD is the residence time of blood inside the VAD chamber, as this time is associated with clot formation. One way to study this residence time is with particle traces. As the residence time of particles may be several periods, it is necessary to trace particles over as many periods as possible. Had a periodic solution been reached, this solution could be repeated many times and linked together to form a particle trace of the desired length. However, because the present simulations have not reached a periodic state, we must use the case for which we have the most available results. In view of the large difference in computational time required to simulate one period with the coarse and fine meshes, the coarse mesh results will be used for particle tracing.

For this analysis, thirteen particles were injected into the VAD at the beginning of the first period, and tracked as they moved through the VAD during five periods. The locations of these particles are shown in Figure 50. In consideration of the regions of backflow in the inlet tube, the particles were injected at y = 70 mm, which is slightly upstream from the location at which the inlet tube merges with the hemispherical VAD

chamber. This was done to minimize the number of particles that exited the VAD through the inlet tube, as this path of exit would not be present in an actual device. The results of this particle tracing are presented in Figure 51. This graph shows that two of the particles left during the first period, nine of them left during the second period and one still remained inside the VAD at the end of the fifth period. Note that, even though the particles were injected close to the VAD chamber, four of the thirteen particles still exited the VAD chamber through backflow at the inlet.

4.3 Closed Loop Model

For this study, the VAD model was coupled to the circulatory system model to form a closed loop. The major difference from the open loop case is the use of a slightly compressible fluid model, as required by the ADINA flow solver in order to reach convergence. This causes certain limitations in the solution that are discussed later in this chapter.

Figure 52 to Figure 53 show fluid velocity vector results for the first period of the closed loop simulation. Like the corresponding open loop results, all velocity vectors have been assigned the same length, with the velocity magnitude indicated by colour only. Velocities with values higher than or equal to 0.42 m/s have been plotted with the same colour to improve visualization of the results at lower velocities. In these figures, blood flows around the loop in a counter-clockwise direction.

Due to the slightly compressible fluid model required in closed loop simulations, the pressure inside the loop is much larger than for the open loop case. This large pressure causes compression of the fluid, which slightly reduces the volume of blood ejected from the VAD from 480 to 465 cm^3 per period.

A brief description of the flow in the closed loop system will be presented below. At t = 0, the diaphragm and the tube walls are in their undeformed states and begin moving upward and outward, respectively, as fluid leaves the VAD. Notice that, in the first image in Figure 52, the fluid velocity decreases as it exits the rigid VAD outlet tube and

enters the elastic tube representing the total arterial compliance. A further decrease in velocity can be seen as the fluid moves through the porous medium and into the elastic tube representing the total venous compliance. Because the VAD is now connected to a loop, the backflow previously seen in the open loop case at the exit of the outlet tube is no longer present in the closed loop model.

At $t = 0.25T$, the diaphragm reaches its highest point and the tube walls have expanded to their maximum size. The inlet valve now opens, and the fluid begins to flow into the VAD, causing the tube wall to contract. Unlike the open loop case, the fluid flowing into the VAD flows towards the centre of the hemispherical chamber as opposed to the outer wall. As the elastic walls contract to their undeformed state, the flow into the VAD chamber becomes straighter, similar to what was seen in the open loop case. In the fourth image in Figure 52, representing the mid-point in the cycle, a clear increase in velocity can be seen as the fluid exits the porous medium, and again as the fluid enters the rigid VAD inlet tube from the attached elastic tube. As the diaphragm moves below its undeformed state, the elastic walls continue to contract. Once the diaphragm reaches its lowest point, the outlet valve opens forcing flow out of the VAD, which expands the elastic walls back to their undeformed states by the end of the period.

4.3.1 Periodicity

As with the open loop results, several periods must be simulated to approach a periodic solution. Graphical comparisons between these periods are given in Figure 54 to Figure 58 and quantitative comparisons are given in Table 4-8. Due to the slightly compressible fluid model generating unrealistic pressures in the VAD, results at control node *a* are not presented. Note that the first period was simulated using the less accurate Euler time integration method, while all subsequent periods used the TR-BDF method. As a result, differences between periods one and two are due not only to non-periodicity effects, but also to time integration effects.

Overall, excellent agreement can be seen between all periods. This agreement is much better between periods two to seven than between periods one to two, due to the poor

initial conditions for period one and the different time integration methods used. Differences between periods two to seven are discussed in more detail below.

For the external nodes, *b* and *c*, all differences between periods two to seven are minor. A slight improvement can be seen in the results starting with the third period, suggesting that a full period was required with the TR-BDF method for initialization.

Table 4-8. Comparison of fluid nodal results between periods with the coarse mesh.

	Average Absolute Difference					
Point	**Period 1 – Period 2**	**Period 2 – Period 3**	**Period 3 – Period 4**	**Period 4 – Period 5**	**Period 5 – Period 6**	**Period 6 – Period 7**
b	0.043 m/s	0.004 m/s	0.003 m/s	0.001 m/s	0.001 m/s	0.001 m/s
c	0.022 m/s	0.006 m/s	0.002 m/s	0.002 m/s	0.002 m/s	0.002 m/s
d	0.023 m/s	0.005 m/s	0.002 m/s	4×10^{-4} m/s	4×10^{-4} m/s	4×10^{-4} m/s
e	0.005 m/s	0.010 m/s	0.001 m/s	0.001 m/s	2×10^{-4} m/s	2×10^{-4} m/s
f	0.004 m/s	0.004 m/s	0.001 m/s	1×10^{-4} m/s	1×10^{-4} m/s	1×10^{-4} m/s

For the internal nodes, nodes *d*, *e*, and *f*, there is a visible improvement in the agreement between the results from periods three to seven compared to periods two and three. This improvement can be seen in Figure 56 to Figure 58, in which the waveforms for periods three to seven are almost coincident, while a gap exists between those waveforms and the ones for the second period. At node *d*, a small amount of scatter between periods three to seven is present around $t = 0.5T$. A similar scatter is seen at the same times for node *f*.

While agreement between periods continues to improve as the number of periods increases, small differences still exist suggesting that additional periods must be run to reach a periodic solution.

4.3.2 Comparison to Open Loop VAD

Before comparing the velocities found in the open and closed loop simulations, a brief look at the normalized pressures at node *a* will be presented. Due to the slightly compressible fluid used in the closed loop case, the magnitude of the pressure inside the

VAD is much larger for the closed loop than for the open loop. In order to compare the waveforms in the two cases, the pressures at node *a* have been normalized by their respective maxima and plotted in Figure 59. It can be seen that the pressure for the closed loop case has a waveform similar to that of the forcing function, while the pressure in the open loop case has a different waveform, as was discussed in more detail in the previous section.

Velocities at control nodes *b-f* for the seventh period of simulation with the coarse mesh density have been plotted in Figure 60 to Figure 64, for the open and closed loop cases, with quantitative comparisons given in Table 4-9. The velocity waveforms are similar for the two cases. With the exception of results at node *f*, the magnitudes of the closed loop velocities were smaller than the corresponding open loop results. For nodes *b* and *e*, the fluctuations in the velocities present in the open loop case are much smoother in the closed loop case. At node *f*, the magnitude of the *x*-velocities is much smaller than for the other nodes, making the differences between cases more noticeable in Figure 64 due to the smaller velocity scale. However, with the exception of a small shift in the peak values, overall agreement is good between the two cases.

Table 4-9. Comparison of fluid nodal results between open and closed loop models.

Point	Minimum Absolute Difference	Average Absolute Difference	Maximum Absolute Difference
b	0.048 m/s	0.548 m/s	1.179 m/s
c	0.066 m/s	0.800 m/s	1.270 m/s
d	0.030 m/s	0.167 m/s	0.651 m/s
e	0.013 m/s	0.093 m/s	0.307 m/s
f	2.7×10^{-4} m/s	0.020 m/s	0.111 m/s

With the exception of node *f*, the closed loop velocity results have been damped due to the slightly compressible fluid model that must be used for solution convergence. This damping is most likely caused by the large increase in pressure inside the system leading

to the compression of the fluid. The limitations of the slightly compressible fluid model are discussed in more detail in the next section.

4.4 Limitations

The results of this study are constrained by several simplifications that were made to make the completion of this study feasible. In view of the lack of available geometric information about actual VADs, an idealized geometry was chosen. This particular geometry was chosen due to the availability of results for comparison, even though these results were obtained using a different flow forcing. Because the fluid model was idealized and our interest was in the blood flow in the system, an idealized solid material was used to represent the diaphragm.

The flow in the VAD was taken to be laminar, although flow in an actual VAD would likely be turbulent. This simplification was made to allow for computational simplicity and to permit comparison to previous laminar flow studies.

Simplifications of the valves as instantly opening and closing were done to match the BU-VAD research and to reduce the complexity of this simulation. Modelling actual valves opening and closing is an active area of research, which requires excellent control of the mesh quality and large computational resources to model the valves themselves, making accurate valve modelling too complex for the scope of this thesis.

Simulations of complex systems requiring large mesh densities and multiple periods are currently limited by the speed of the computer hardware and software as well as the RAM available to the solvers. In both the open and closed loop cases, the coarse mesh densities were at the RAM limit of the Beowulf cluster, and therefore, further refinements forced us to run simulations on HPCVL. We were limited to two concurrent simulations on HPCVL, while seven concurrent simulations could be run on the Beowulf cluster. On both systems, we were limited to two processors per simulation.

At the current parallelization and optimization of the solvers in ADINA, running the multiple periods required to reach a grid-independent periodic solution would require several months of computational time.

The open loop model is limited by the fact that it is coupled to a zero pressure reservoir. This is obviously not the case with an actual VAD, and was one of the reasons for the closed loop simulations.

For the closed loop simulations, the major limitation is the requirement that a slightly compressible fluid model must be used to allow for solution convergence. As the fluid is compressed, the pressure inside the VAD increases and the pressure gradient decreases towards zero. Because of the lack of pressure gradient, compliance and resistance values for the circulatory system model cannot be calculated, as both of these quantities depend on non-zero pressure gradients. For the compliant tubes, the expansion and contraction of the walls are controlled by the difference between the fluid bulk modulus and the modulus of elasticity of the walls. If the walls are stiffer that the fluid, the fluid compresses instead of forcing the walls outward. Therefore, for wall motion to occur, the only criterion that needs to be satisfied is that the Young's modulus of the walls is less than the fluid bulk modulus. For the porous medium, the cross sectional area inside the medium seems to play a determining role in the resistance to flow. A U-shaped tube with the same diameter as the compliant tubes was tested as an alternative porous medium geometry. Even with a decrease in porosity and permeability, the velocity through the U-shaped tube did not decrease as much as in the rectangular prism porous medium geometry.

To improve the results, the fluid bulk modulus should be increased to simulate as closely as possible an incompressible fluid. However, as the fluid bulk modulus is increased and the fluid becomes less compressible, it becomes increasingly difficult to obtain convergence. As a result, to improve the closed loop results, further relaxation of the slightly compressible fluid requirements needs to be made.

CHAPTER 5

CONCLUSIONS AND RECOMMENDATIONS FOR FUTURE RESEARCH

5.1 Conclusions

CFD can be used as a powerful technique for the optimization of a VAD design. Because complications of the conditions of patients with VADs have been correlated to the fluid dynamics inside the VAD, accurate fluid simulations can suggest areas requiring design refinement. Although simplifications to the geometry, valves, and flow model have been made to make this study feasible, the major conclusion from this study is that FSI effects can be simulated in a VAD. This allows for a study of the flow features while taking into account the motion of the solid diaphragm, which has been neglected in previous studies.

The present thesis contains the results of open and closed loop simulations of blood flow in an idealized VAD. The open loop results were compared to the results of previous research at Brunel University, using a geometry on which the current VAD model was based. Differences were found in the shape of the volume displacement waveforms between the two models, despite matching the total ejection volumes. These differences lead to a somewhat higher maximum Reynolds number in the current model compared to the one in the BU-VAD. Differences were also found in the waveforms and magnitudes of the pressures inside the VAD. These differences were attributed to differences in flow

forcing. Overall, however, fair agreement is found in the velocity waveforms at representative control locations. Magnitudes of the velocities in the two studies differ slightly, in conformity with differences in Reynolds numbers and pressure magnitudes. It should be noted that differences of a similar order could be seen between the computational and experimental results in the BU-VAD studies.

Mesh studies were done for the solid and fluid meshes for the open loop VAD. The membrane mesh was found to be sufficiently fine for the numerical solutions to be essentially mesh-independent. While the corresponding waveforms were not very different for the two fluid meshes, non-trivial local differences in values were observed. It is acknowledged that further mesh refinement is required to resolve such differences. However, due to time considerations, additional fluid mesh refinement was not feasible at this time.

Multiple periods were run for both the coarse and fine mesh densities for the open loop VAD. Eight periods were simulated for the coarse mesh, compared to four periods for the fine mesh. In both cases, there is a tendency towards periodicity, indicating that such a state would be achieved if the study were extended to a few more periods.

In the second part of the study, the operating VAD was coupled to a representative circulatory system model. Incompressible fluid models could not be used in this case because of the strict volume conservation requirements for incompressible fluids that are difficult to achieve inside an enclosure with moving boundaries. As a result, slightly compressible fluid models were used. The consequence of this is that the results were limited by the compressibility of the fluid. The fluid compressibility around the loop was relatively high, causing the pressure inside the VAD to increase dramatically and the velocity to decrease. A lack of pressure gradient prevented us from calibrating the circulatory system model. Further work is needed to ease this slightly compressible fluid requirement.

Overall, this study showed the feasibility of this approach and its potential for simulating actual VAD operation. Considering the complexity of an actual VAD geometry and the need for a more realistic simulation of moving valves and other components, it is expected that the required computational power and time would be significantly higher than presently employed. Improvements in code parallelization, along with future increases in computational speed, would add to the feasibility of simulating the operation of an actual VAD.

5.2 Recommendations for Future Research

Before discussing improvements in the computational model, it is necessary to identify the need for validation of the simulation by comparison to experimental results in a closely related, if not identical, configuration. Such experimental results are not yet available, but an experimental model is currently under construction in the Fluid Mechanics Laboratory of the University of Ottawa and it is hoped that relevant information will become available in the near future.

This study is of a preliminary nature and has been carried out to show the feasibility of using CFD to simulate blood flow in an operating VAD. As such, many simplifications have been made to allow for its completion, but extensions and improvements of this work may help the model become more realistic. Two relatively straightforward improvements would be the use of a more physiologically accurate waveform, rather than the sinusoidal one used in this and previous works, and more realistic diaphragm models, rather than the linear elastic material with zero thickness that was presently used. Another important improvement would be to model the flow inside the VAD as turbulent instead of laminar as this is a more realistic representation of the actual flow in a VAD.

More significant changes to the current VAD model include improvements in the valve operation, the circulatory loop, and the VAD geometry. The instantly opening and closing valves could be replaced by models of mechanical heart valves found in actual VADs, as for example the moving leaflet type. This would require a substantial increase in computational time as well as the use of mesh adaptation techniques. The circulatory

loop used in this work is a dramatic simplification of the actual system. Several elements, such as the pulmonary circulatory loop and the chambers of the heart have been neglected in our simplified model. Adding these elements would more realistically model the impedance to pumping the VAD actually experiences. Alternatively, instead of using a three-dimensional FSI model of the circulatory system, an electric circuit analogy could be used. This could remove the current limitation of using a slightly compressible fluid instead of a purely incompressible one. By making these improvements and more closely representing a specific actual VAD, researchers will be able to use computational software to modify their VAD design to obtain the desired flow features without having to construct many prototypes.

REFERENCES

ADINA R & D, Inc. (2003). *Theory and modeling guide volume I: ADINA.* Report ARD 03-7. Watertown, MA: ADINA R & D, Inc.

ADINA R & D, Inc. (2003). *Theory and modeling guide volume III: ADINA-F.* Report ARD 03-9. Watertown, MA: ADINA R & D, Inc.

Anderson, J. B., Wood, H. G., Allaire, P. E., McDaniel, J. C., Olen, D. B., & Bearnson, G. (2000). Numerical studies of blood shear and washing in a continuous flow ventricular assist device. *ASAIO Journal, 46,* 486-494.

Bachmann, C., Hugo, G., Rosenberg, G., Deutsch, S., Fontaine, A., & Tarbell, J. M. (2000). Fluid dynamics of a pediatric ventricular assist device. *Artificial Organs, 24,* 362-372.

Baldwin, J. T., Deutsch, S., Geselowitz, D. B., & Tarbell, J. M. (1990). Estimation of Reynolds stresses within the Penn State left ventricular assist device. *ASAIO Transactions, 36,* M274-M278.

Baldwin, J. T., Deutsch, S., Geselowitz, D. B., & Tarbell, J. M. (1994). LDA measurements of mean velocity and Reynolds stress fields within an artificial heart ventricle. *Journal of Biomechanical Engineering, 116,* 190-200.

Baldwin, J. T., Tarbell, J. M., Deutsch, S., & Geselowitz, D. B. (1989). Mean flow velocity patterns within a ventricular assist device. *ASAIO Transactions, 35,* 429-433.

Bathe, K. J. (1996). *Finite element procedures.* Englewood Cliffs, NJ: Prentice Hall.

Bathe, K. J., Zhang, H., & Ji, S. (1999). Finite element analysis of fluid flows fully coupled with structural interactions. *Computers and Structures, 72,* 1-16.

Bathe, K. J., Zhang, H., & Wang, M. H. (1995). Finite element analysis of incompressible and compressible fluid flows with free surfaces and structural interactions. *Computers and Structures, 56,* 193-213.

Bathe, K. J., Zhang, H., & Zhang, X. (1997). Some advances in the analysis of fluid flows. *Computers and Structures, 64,* 909-930.

Bathe, M., & Kamm, R. D. (1999). A fluid-structure interaction finite element analysis of pulsatile blood flow through a compliant stenotic artery. *Journal of Biomechanical Engineering, 121*, 361-369.

Berne, R. M., & Levy, M. N. (1992). Control of cardiac output: Coupling of heart and blood vessels. In *Cardiovascular physiology* (pp. 194-218). (6th ed.). St. Louis, Missouri: Mosby - Year Book, Inc.

Chen, J. M., Spanier, T. B., Gonzalez, J. J., Marelli, D., Flannery, M. A., Tector, K. A., Cullinane, S., & Oz, M. C. (1999). Improved survival in patients with acute myocarditis using external pulsatile mechanical ventricular assistance. *Journal of Heart and Lung Transplantation, 18,* 351-357.

Chesler, N. C., & Kamm R. D. (1998). Performance analysis of a cardiac assist device in counterpulsation. *Journal of Biomechanical Engineering, 120,* 437-445.

Clark, C., Jin, W., & Glaser, A. (1990). The fluid mechanics of a sac-type ventricular assist device. *The International Journal of Artificial Organs, 13,* 814-822.

Collard, E., Van Dyck, M. J., & Jacquet, L. M. (2003). Ventricular assist devices. *Current Opinion in Anaesthesiology, 16,* 33-43.

De Hart, J., Baaijens, F. P. T., Peters, G. W. M., & Schreurs, P. J. G. (2003). A computational fluid-structure interaction analysis of a fiber-reinforced stentless aortic valve. *Journal of Biomechanics, 36,* 699-712.

Delgado, D. H., Rao, V., Ross, H. J., Verma, S., & Smedira, N. G. (2002). Mechanical Circulatory Assistance: State of the Art. *Circulation, 106,* 2046-2050.

Deserranno, D., Popovic, Z. B., Greenberg, N. L., Kassemi, M., & Thomas, J. D. (2003). Axisymmetric fluid-structure interaction model of the left ventricle. In K. J. Bathe (Ed.), *Second MIT Conference on Computational Fluid and Solid Mechanics* (pp. 1669-1672). Oxford, UK: Elsevier Science Ltd.

Formaggia, L., Gerbeau, J.-F., Nobile, F., & Quarteroni, A. (2000). *On the coupling of 3D and 1D Navier-Stokes equations for flow problems in compliant vessels.* Technical Report 3862, INRIA.

Formaggia, L., Nobile, F., & Quarteroni, A., & Veneziani, A. (1999). Multiscale modelling of the circulatory system: A preliminary analysis. *Computing and Visualisation in Science, 2,* 75-83.

Frazier, O. H., Fuqua Jr., J. M., & Helman, D. N. (2000). Clinical left heart assist devices: A historical perspective. In D. J. Goldstein, & M. C. Oz (Eds.), *Cardiac assist devices* (pp. 3-13). Armonk, NY: Futura Publishing Company, Inc.

Fuchs, A., & Netz, H. (2002). Ventricular assist devices in pediatrics. *Images in Paediatric Cardiology, 9,* 24-54.

Fung, Y. C. (1990). *Biomechanics: Motion, flow, stress, and growth.* New York, NY: Springer-Verlag.

Geertsema, A. A., Rakhorst, G., Mihaylov, D., Blanksma, P. K., & Verkerke, G. J. (1997). Development of a numerical simulation model of the cardiovascular system. *Artificial Organs, 21,* 1297-1301.

Gresho, P. M., & Sani, R. L. (2000). *Incompressible flow and the finite element method. Volume 2: Isothermal laminar flow.* Chichester, England: John Wiley & Sons Ltd.

Guyton, A. C., & Hall, J. E. (2000). *Textbook of medical physiology.* (10th ed.). Philadelphia, PA: W. B. Saunders Company.

Hendry, P. J., Mussivand, T. V., Masters, R. G., Bourke, M. E., Guiraudon, G. M., Holmes, K. S., Day, K.D., & Keon, W. J. (2001). The HeartSaver left ventricular assist device: An update. *Annals of Thoracic Surgery, 71,* S166-S170.

Henry, F. S., Shortland, A. P., Iudicello, F., Black, R. A., Jarvis, J. C., Collins, M. W., & Salmons, S. (1997). Flow in a simple model skeletal muscle ventricle: Comparison between numerical and physical simulations. *Journal of Biomechanical Engineering, 119,* 13-19.

Herwig, V., Severin, M., Waldenberger, F. R., & Konertz, W. (1997). Medos®/HIA-assist system: First experiences with mechanical circulatory assist in infants and children. *The International Journal of Artificial Organs, 20,* 692-694.

Hochareon, P., Manning, K. B., Fontaine, A. A., Deutsch, S., & Tarbell, J. M. (2003). Diaphragm Motion Affects Flow Patterns in an Artificial Heart. *Artificial Organs, 27,* 1102-1109.

Hoppensteadt, F. C., & Peskin, C. S. (2002). *Modeling and simulation in medicine and the life sciences.* (2nd ed.). New York, NY: Springer-Verlag.

Jin, W., & Clark, C. (1993). Experimental investigation of unsteady flow behaviour within a sac-type ventricular assist device (VAD). *Journal of Biomechanics, 26,* 697-707.

Jin, W., & Clark, C. (1994). Experimental investigation of the motions of the pumping diaphragm within a sac-type pneumatically driven ventricular assist device. *Journal of Biomechanics, 27,* 43-55.

Kim, S. H., Chandran, K. B., & Chen, C. J. (1992). Numerical simulation of steady flow in a two-dimensional total artificial heart model. *Journal of Biomechanical Engineering, 114,* 497-503.

Kiris, C., Kwak, D., Rogers, S., & Chang, I.-D. (1997). Computational approach for probing the flow through artificial heart devices. *Journal of Biomechanical Engineering, 119,* 452-460.

König, C. S., & Clark, C. (2001). Flow mixing and fluid residence times in a model of a ventricular assist device. *Medical Engineering and Physics, 23,* 99-110.

König, C. S., Clark, C., & Mokhtarzadeh-Dehghan, M. R. (1999). Comparison of flow in numerical and physical models of a ventricular assist device using low- and high-viscosity fluids. *Proceedings of the Institution of Mechanical Engineers Part H, 213,* 423-432.

König, C. S., Clark, C., & Mokhtarzadeh-Dehghan, M. R. (1999). Investigation of unsteady flow in a model of a ventricular assist device by numerical modelling and comparison with experiment. *Medical Engineering and Physics, 21,* 53-64.

Loebe, M., Kaufmann, F., & Hetzer, R. (2000). Extracorporeal support: The Berlin Heart. In D. J. Goldstein, & M. C. Oz (Eds.), *Cardiac assist devices* (pp. 275-287). Armonk, NY: Futura Publishing Company, Inc.

McCarthy, D. F. (1998). *Essentials of soil mechanics and foundations: Basic geotechnics.* (5th ed.). Upper Sapple River, NJ: Prentice Hall, Inc.

Mehta, S. M., Pae, W. E., Rosenberg, G., Snyder, A. J., Weiss, W. J., Lewis, J. P., Frank, D. J., Thompson, J. J., & Pierce, W. S. (2001). The LionHeart LVD-2000: A completely implantable left ventricular assist device for chronic circulatory support. *Annals of Thoracic Surgery, 71,* S156-S161.

Nakata, M., Masuzawa, T., Tatsumi, E., Taenaka, Y., Nishimura, T., Tsukiya, T., Takano, H., Tsuchimoto, K., & Ohba, K. (1998). Characterization and optimization of the flow pattern inside a diaphragm blood pump based on flow visualization techniques. *ASAIO Journal, 44,* M714-M718.

Okamoto, E., Hashimoto, T., Inoue, T., & Mitamura, Y. (2003). Blood compatible design of a pulsatile blood pump using computational fluid dynamics and computer-aided design and manufacturing technology. *Artificial Organs, 27,* 61-67.

Orime, Y., Takatani, S., Tasai, K., Ohara, Y., Naito, K., Mizuguchi, K., Meier, D., Wernicke, J. T., Damm, G., Glueck, J., Noon, G. P., & Nosé, Y. (1994). The Baylor total artificial heart: Flow visualization studies. *ASAIO Journal, 40,* M499-M505.

Pedley, T. J. (1980). *The fluid mechanics of large blood vessels.* Cambridge, UK: Cambridge University Press.

Pennington, D. G., Oaks, T. E., & Lohmann, D. P. (2000). Extracorporeal support: The Thoratec device. In D. J. Goldstein, & M. C. Oz (Eds.), *Cardiac assist devices* (pp. 251-262). Armonk, NY: Futura Publishing Company, Inc.

Peskin, C. S., & McQueen, D. M. (1995). A general method for the computer simulation of biological systems interacting with fluids. In C. P. Ellington, & T. J. Pedley (Eds.), *Biological Fluid Dynamics: Proceedings of a meeting held at the University of Leeds, UK, 4-8 July 1994. Symposia of the society for experimental biology, 49* (pp. 265-276). Cambridge, UK: The Company of Biologists Limited.

Peskin, C. S., & McQueen, D. M. (1996). Fluid dynamics of the heart and its valves. In H. G. Othmer, F. R. Adler, M. A. Lewis, and J. C. Dallon (Eds.), *Case studies in mathematical modeling - Ecology, physiology, and cell biology* (pp. 309-337). Englewood Cliffs, NJ: Prentice-Hall, Inc.

Reddy, J. N. (1993). *An introduction to the finite element method.* (2nd ed.). New York, NY: McGraw-Hill, Inc.

Reddy, J. N., & Gartling, D. K. (2001). *The finite element method in heat transfer and fluid dynamics.* (2nd ed). Boca Raton, FL: CRC Press.

Reichenbach, S. H., Farrar, J., & Hill, J. D. (2001). A versatile intracorporeal ventricular assist device based on the Thoratec VAD system. *Annals of Thoracic Surgery, 71,* S171-S175.

Reul, H. (1999). The MEDOS/HIA system: Development, results, perspectives. *Thoracic and Cardiovascular Surgeon, 47,* 311-315.

Reul, H., Kaufmann, R., & Siess, T. (1998). Cardiac assist devices. In P. Verdonck (Ed.), *Intra and extracorporeal cardiovascular fluid dynamics* (pp. 233-257). Southampton, UK: Computational Mechanics Publications.

Rosenberg, G., Phillips, W. M., Landis, D. L., & Pierce, W. S. (1981). Design and evaluation of the Pennsylvania State University mock circulatory system. *ASAIO Journal, April/June,* 41-49.

Scheidegger, A. E. (1974). *The physics of flow through porous media.* (3rd ed.). Toronto, ON: University of Toronto Press.

Segers, P, Stergiopulos, N., & Westerhof, N. (2002). Relation of effective arterial elastance to arterial system properties. *American Journal of Physiology, 282,* H1041-H1046.

Tang, D., Yang, C., Walker, H., Kobayashi, S., Zheng, J. & Ku, D. N. (2003). 2D and 3D multi-physics models for flow and nonlinear stress/strain analysis of stenotic arteries with lipid cores. In K. J. Bathe (Ed.), *Second MIT Conference on Computational Fluid and Solid Mechanics* (pp. 1829-1832). Oxford, UK: Elsevier Science Ltd.

Tortora, G. J. (2002). *Principles of human anatomy.* (9th ed.). New York, NY: John Wiley & Sons, Inc.

Tsach, U., Geselowitz, D. B., Sinha, A., & Hsu, H. K. (1989). A novel output feedback pusher plate controller for the Penn State electric ventricular assist device. *Journal of Dynamic Systems, Measurement, and Control, 111,* 69-74.

Verdonck, P., Vierendeels, J., & Dierickx, P. (1998). Cardiac mechanical models. In P. Verdonck (Ed.), *Intra and extracorporeal cardiovascular fluid dynamics* (pp. 1-49). Southampton, UK: Computational Mechanics Publications.

Yu, Y.-C., Boston, J. R., Simaan, M. A., Miller, P. J., & Antaki, J. F. (2001). Pressure-volume relationship of a pulsatile blood pump for ventricular assist device development. *ASAIO Journal*, 47, 293-301.

Zhang, H., & Bathe, K. J. (2001). Direct and iterative computing of fluid flows fully coupled with structures. In K. J. Bathe (Ed.), *First MIT Conference on Computational Fluid and Solid Mechanics* (pp. 1440-1443). Oxford, UK: Elsevier Science Ltd.

Zhang, H., Zhang, X., Ji, S., Guo, Y., Ledezma, G., Elabbasi, N., & deCougny, H. (2003). Recent development of fluid-structure interaction capabilities in the ADINA system. *Computers & Structures, 81,* 1071-1085.

Zhang, Q., & Hisada, T. (2001). Analysis of fluid-structure interaction problems with structural buckling and large domain changes by ALE finite element method. *Computer Methods in Applied Mechanics and Engineering, 190,* 6341-6357.

Zienkiewicz, O. C., & Taylor, R. L. (2000). *The finite element method volume 1: The basis.* (5th ed.). Oxford, UK: Butterworth Heinemann.

Zienkiewicz, O. C., & Taylor, R. L. (2000). *The finite element method volume 2: Solid mechanics.* (5th ed.). Oxford, UK: Butterworth Heinemann.

Zienkiewicz, O. C., & Taylor, R. L. (2000). *The finite element method volume 3: Fluid dynamics.* (5th ed.). Oxford, UK: Butterworth Heinemann.

FIGURES

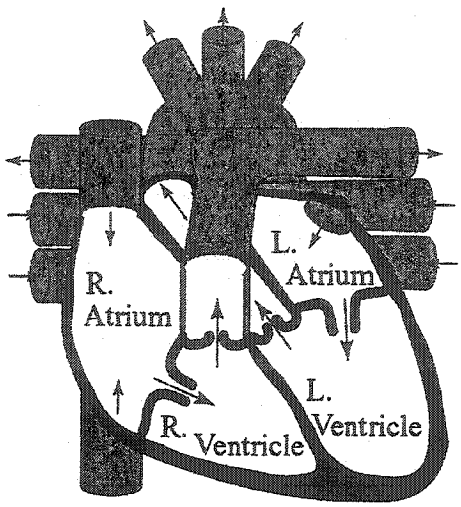

Figure 1. Chambers of the heart.

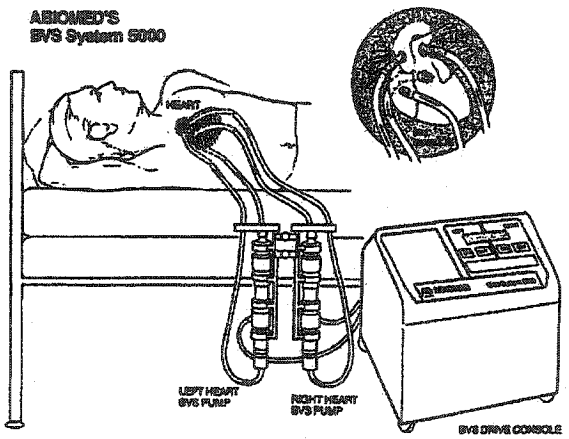

Figure 2. ABIOMED BVS 5000 (from Chen *et al.*, 1999).

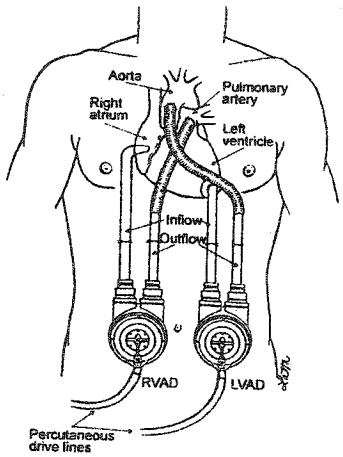

Figure 3. Thoratec VAD (from Frazier *et al.*, 2000).

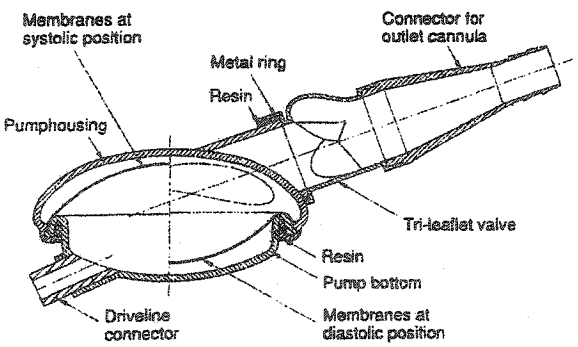

Figure 4. Medos/HIA-VAD (from Reul, 1999).

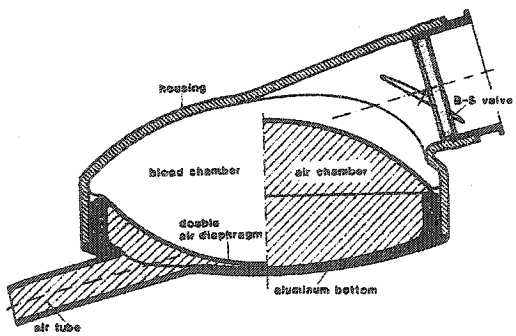

Figure 5. Berlin Heart VAD (from Reul *et al.*, 1998).

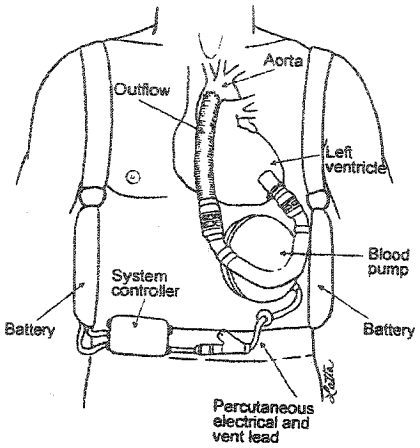

Figure 6. HeartMate VE
(from Frazier *et al.*, 2000).

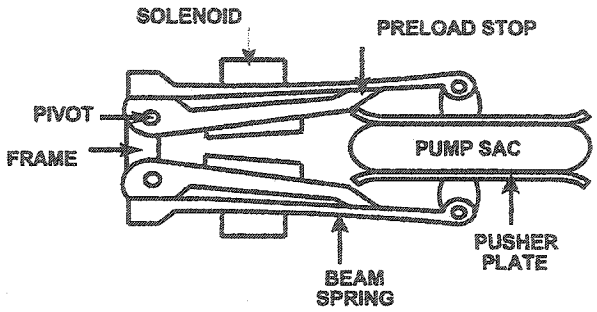

Figure 7. Novacor LVAS
(from Yu *et al.*, 2001).

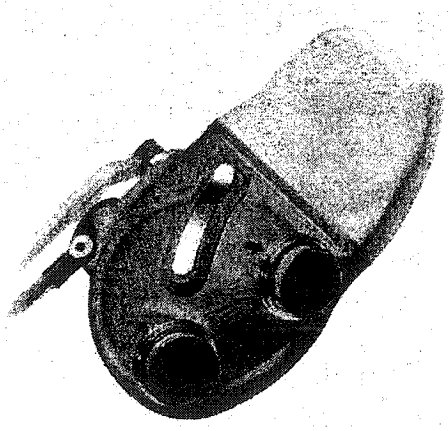

Figure 8. HeartSaver VAD
(from Hendry *et al.*, 2001).

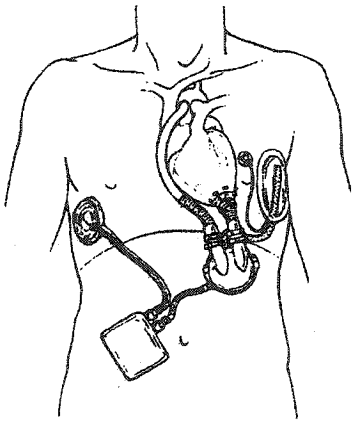

Figure 9. LionHeart LVD-2000
(from Mehta *et al.*, 2001).

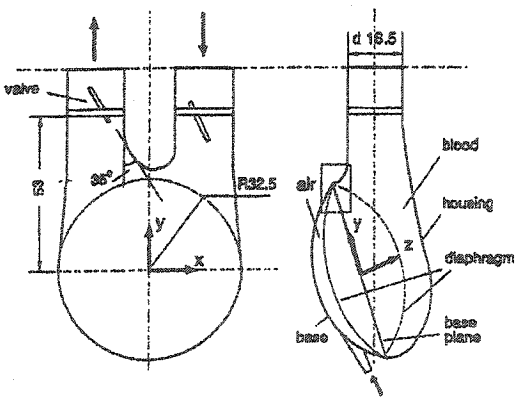

Figure 10. Brunel University VAD
(from Jin & Clark, 1994).

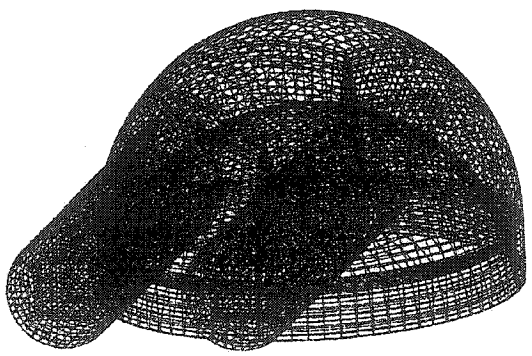

Figure 11. BU-VAD
(from König & Clark, 2001).

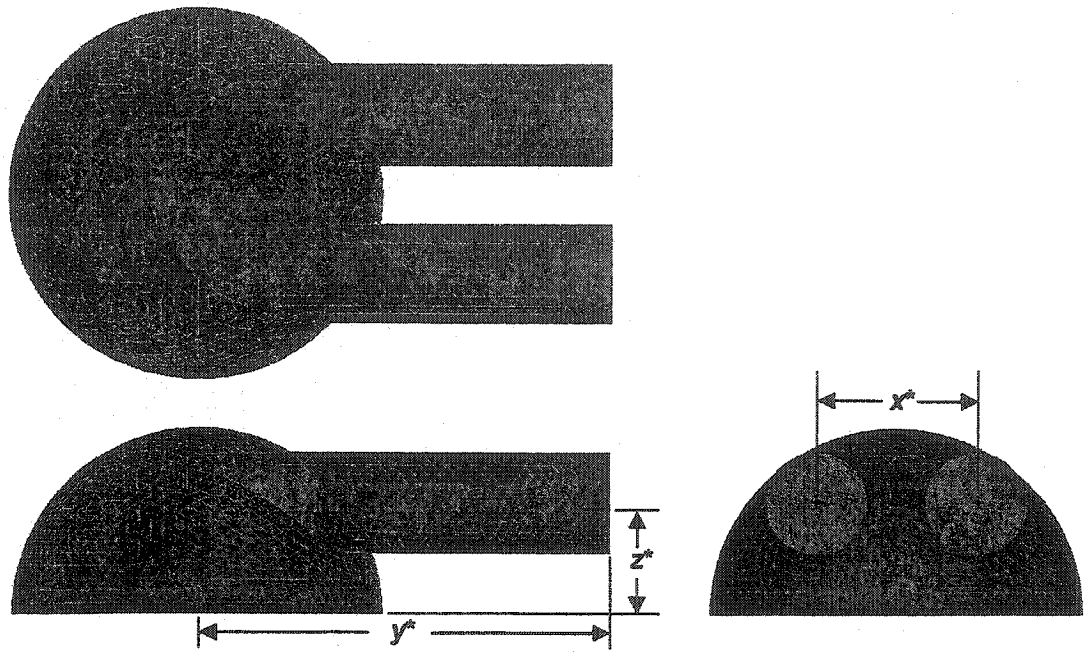

Figure 12. Top and side views of VAD geometry.

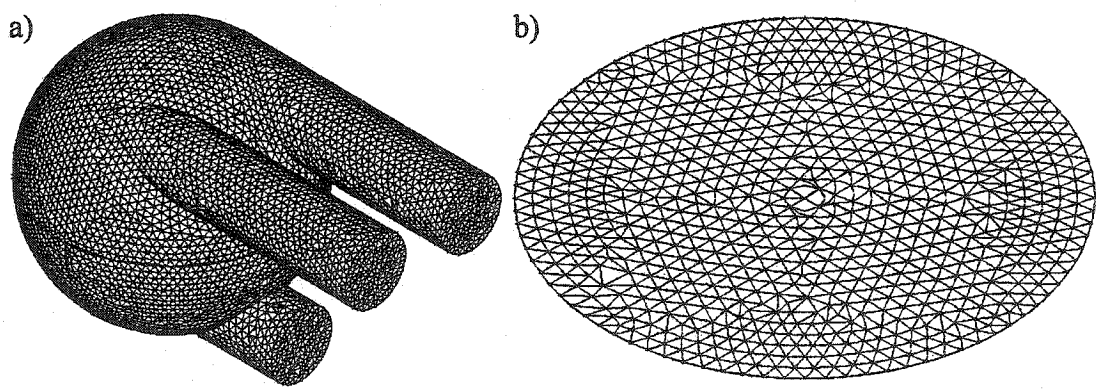

Figure 13. a) Fluid and b) solid VAD geometries.

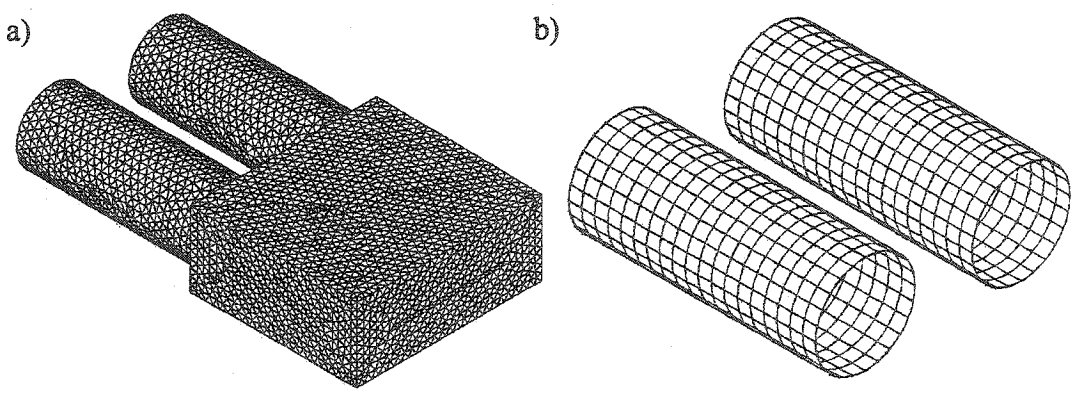

Figure 14. a) Fluid and b) solid circulatory system model geometries.

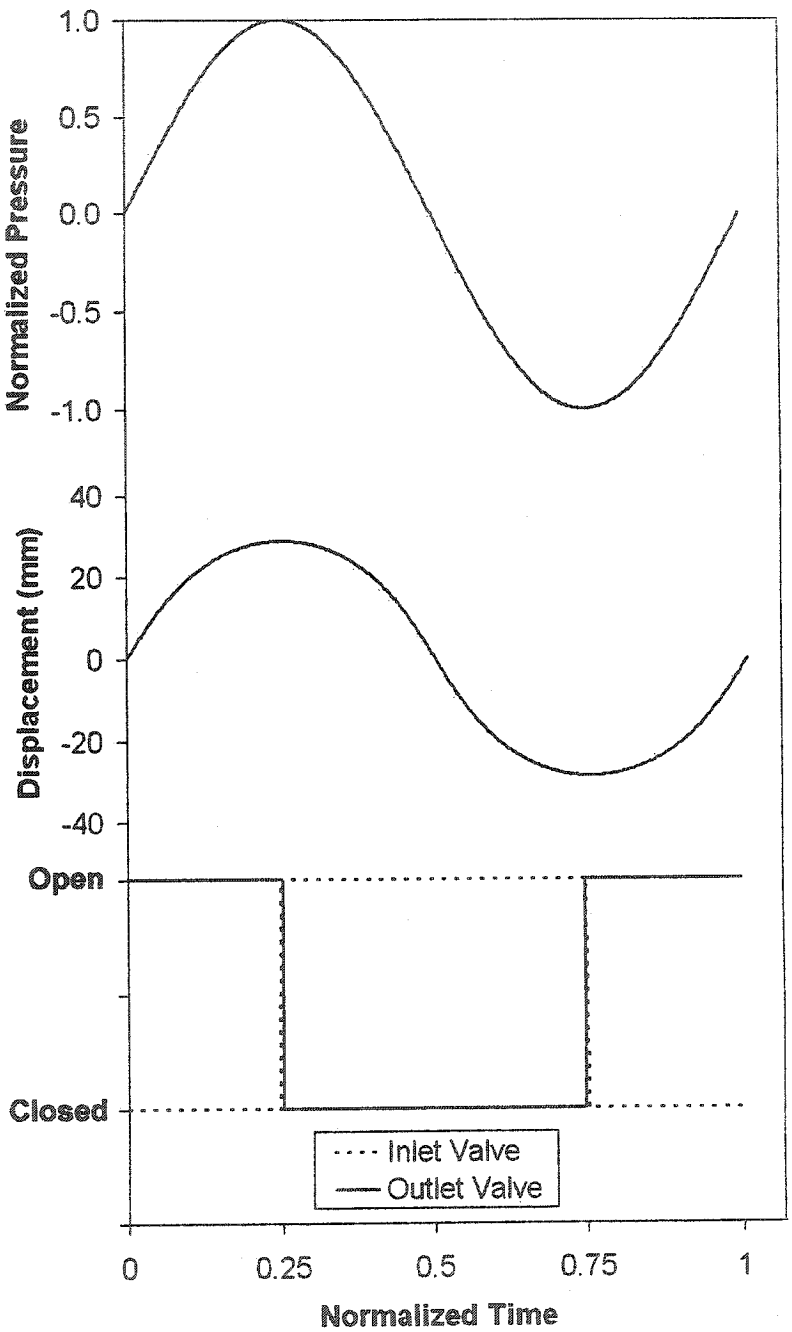

Figure 15. Input pressure function, diaphragm displacement, and valve sequencing during one period of simulation.

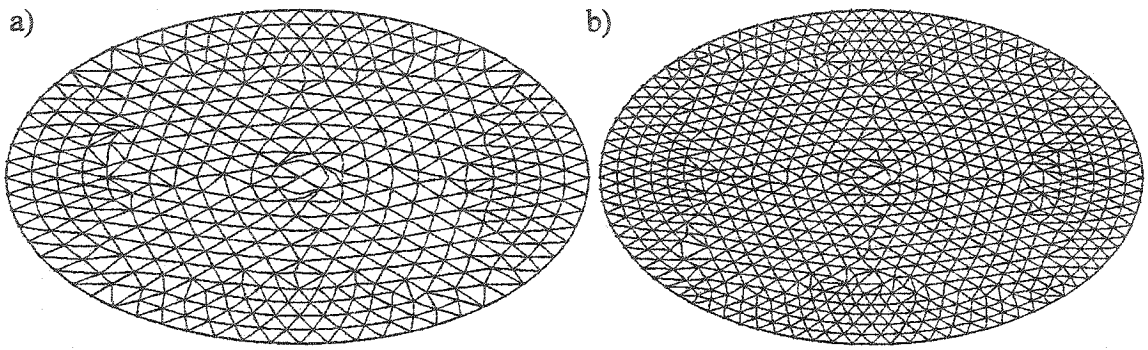

Figure 16. a) Coarse and b) fine solid diaphragm meshes.

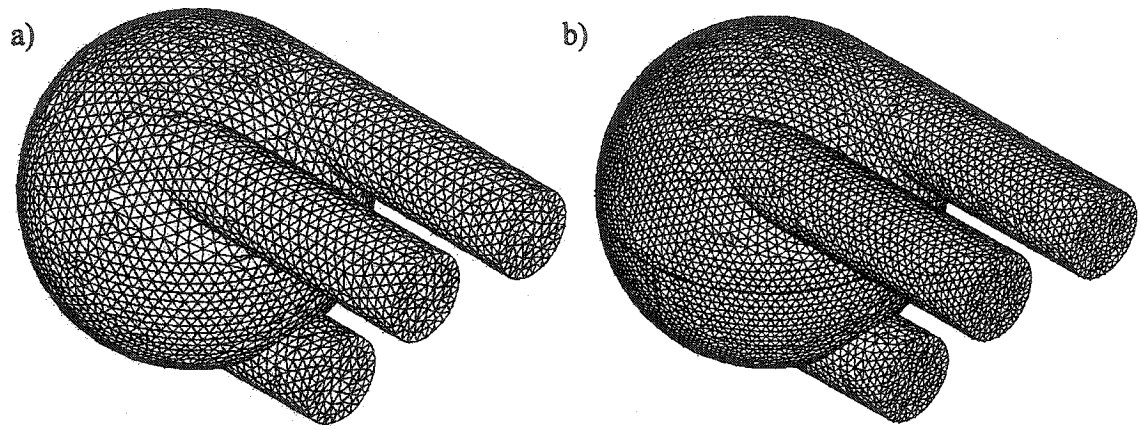

Figure 17. a) Coarse and b) fine fluid VAD meshes.

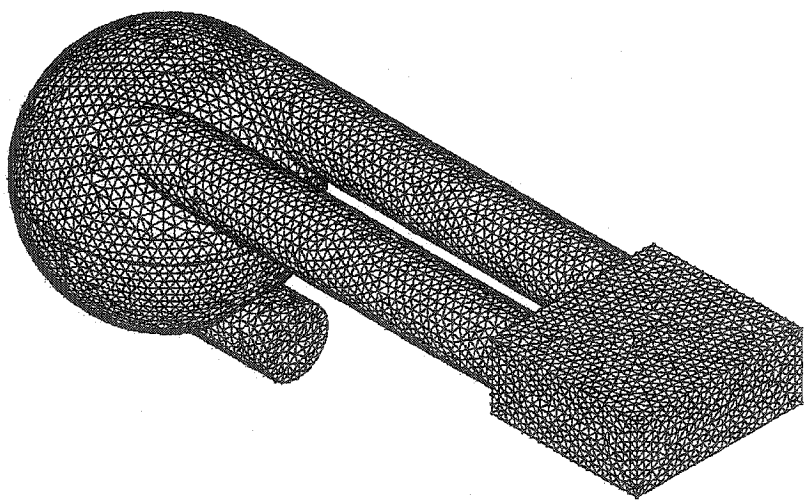

Figure 18. Closed loop mesh.

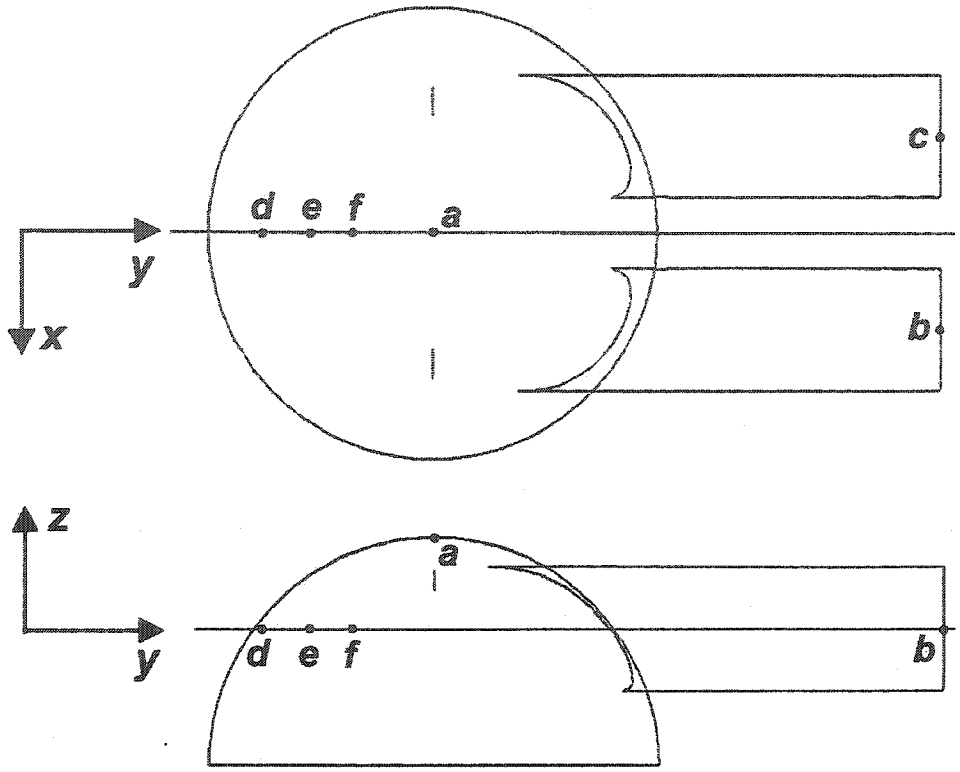

Figure 19. Control node locations within the fluid geometry.

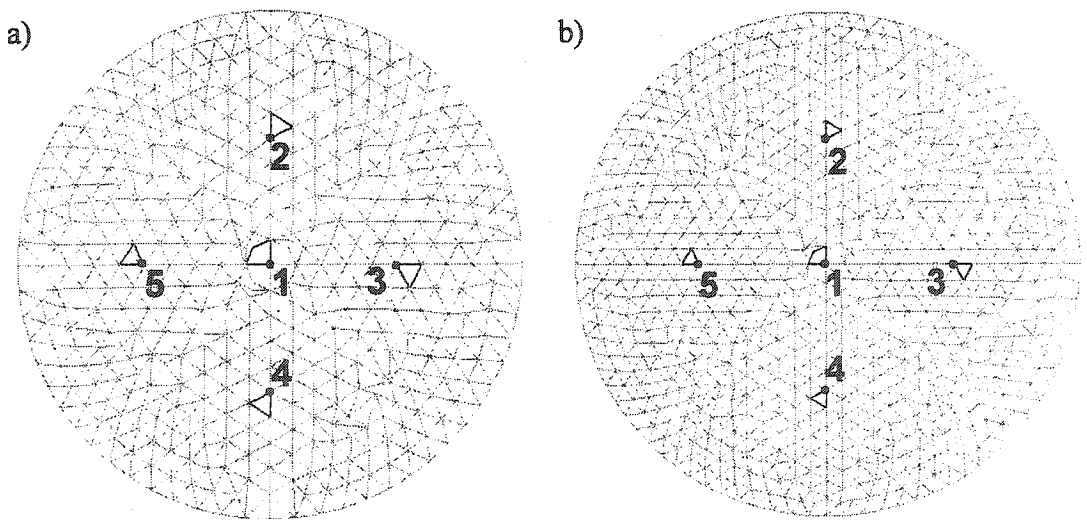

Figure 20. Control element and node locations on the solid diaphragm for the a) coarse and b) fine mesh densities.

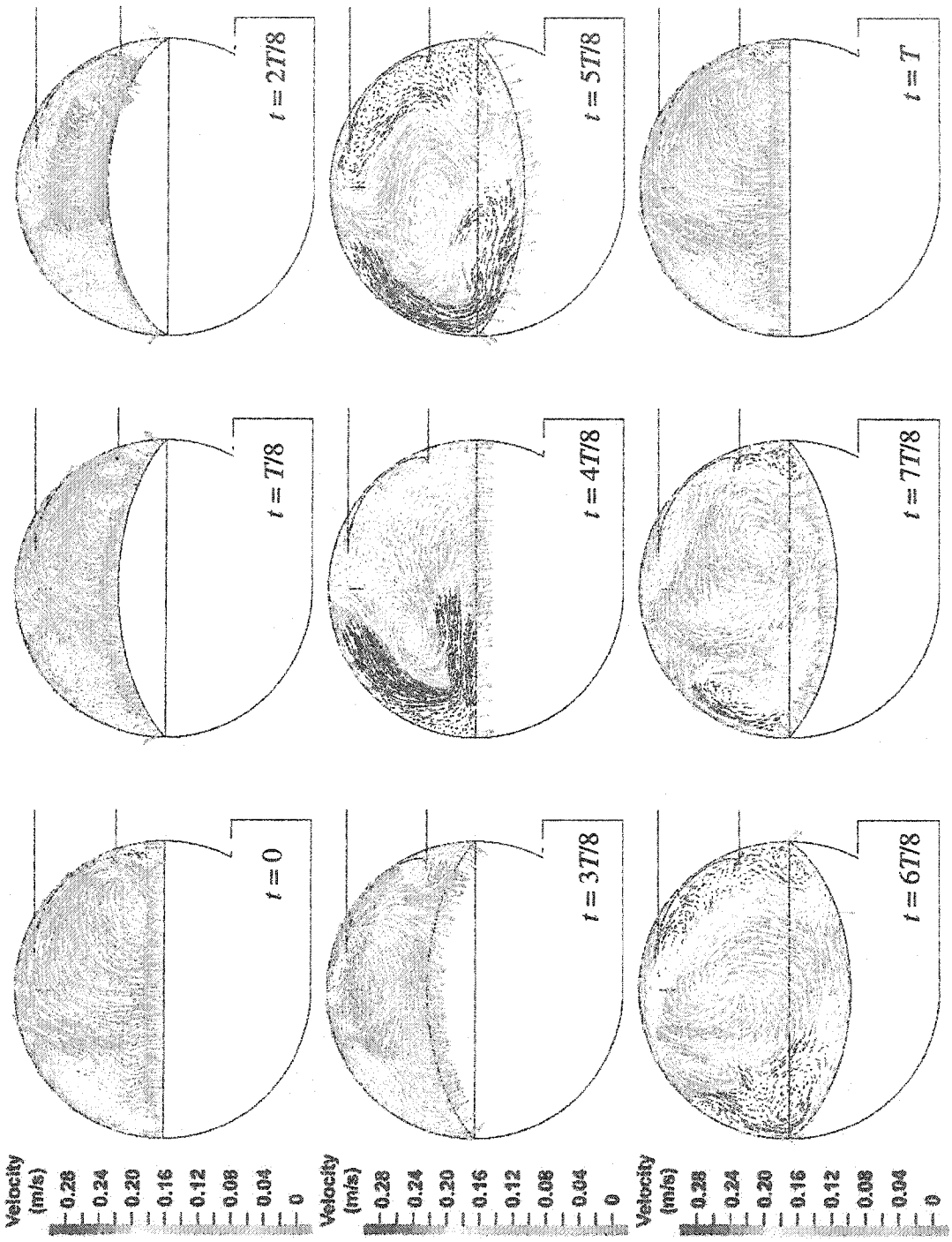

Figure 21. Open loop diaphragm deformation and velocity vectors for one period.

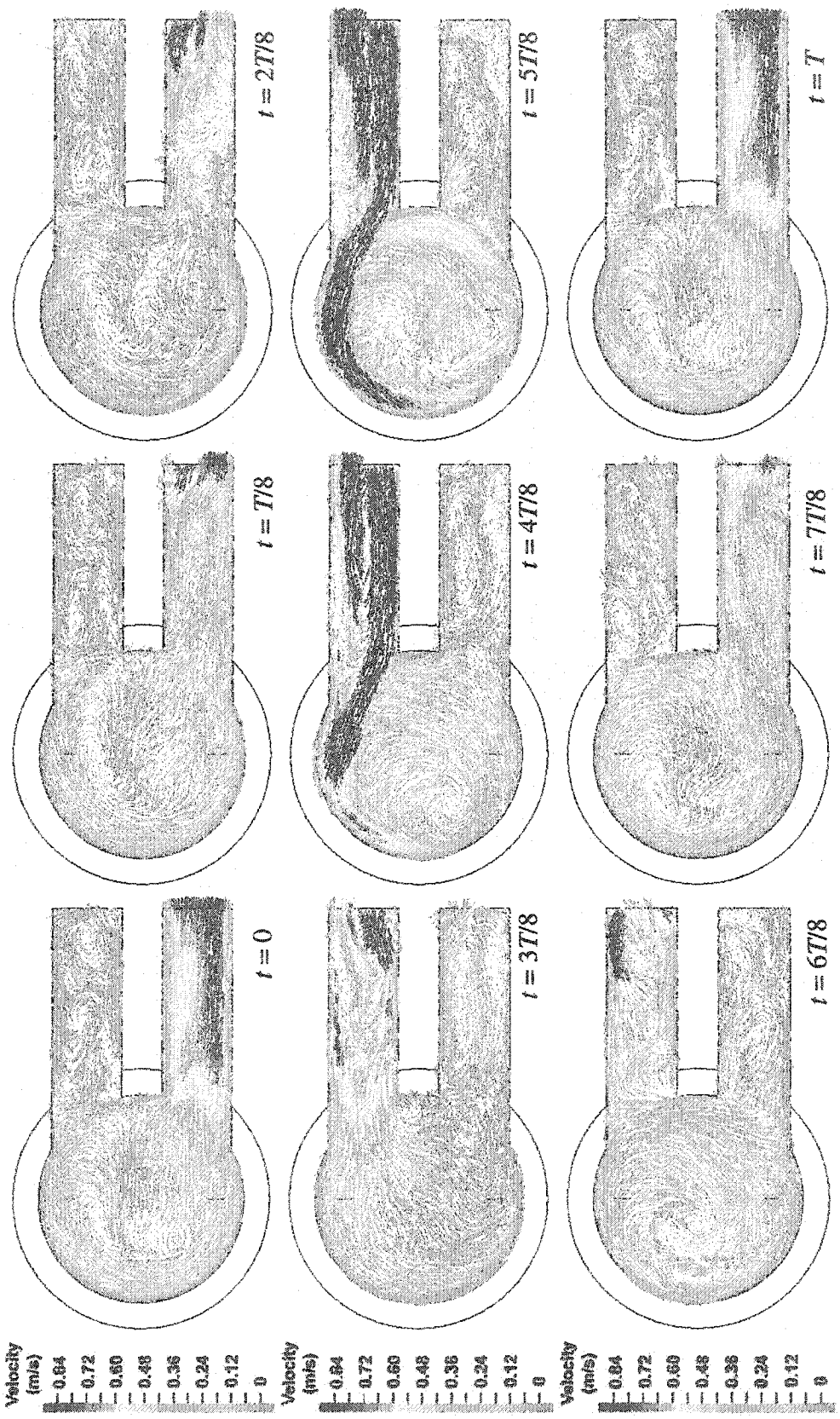

Figure 22. Open loop velocity vectors for one period.

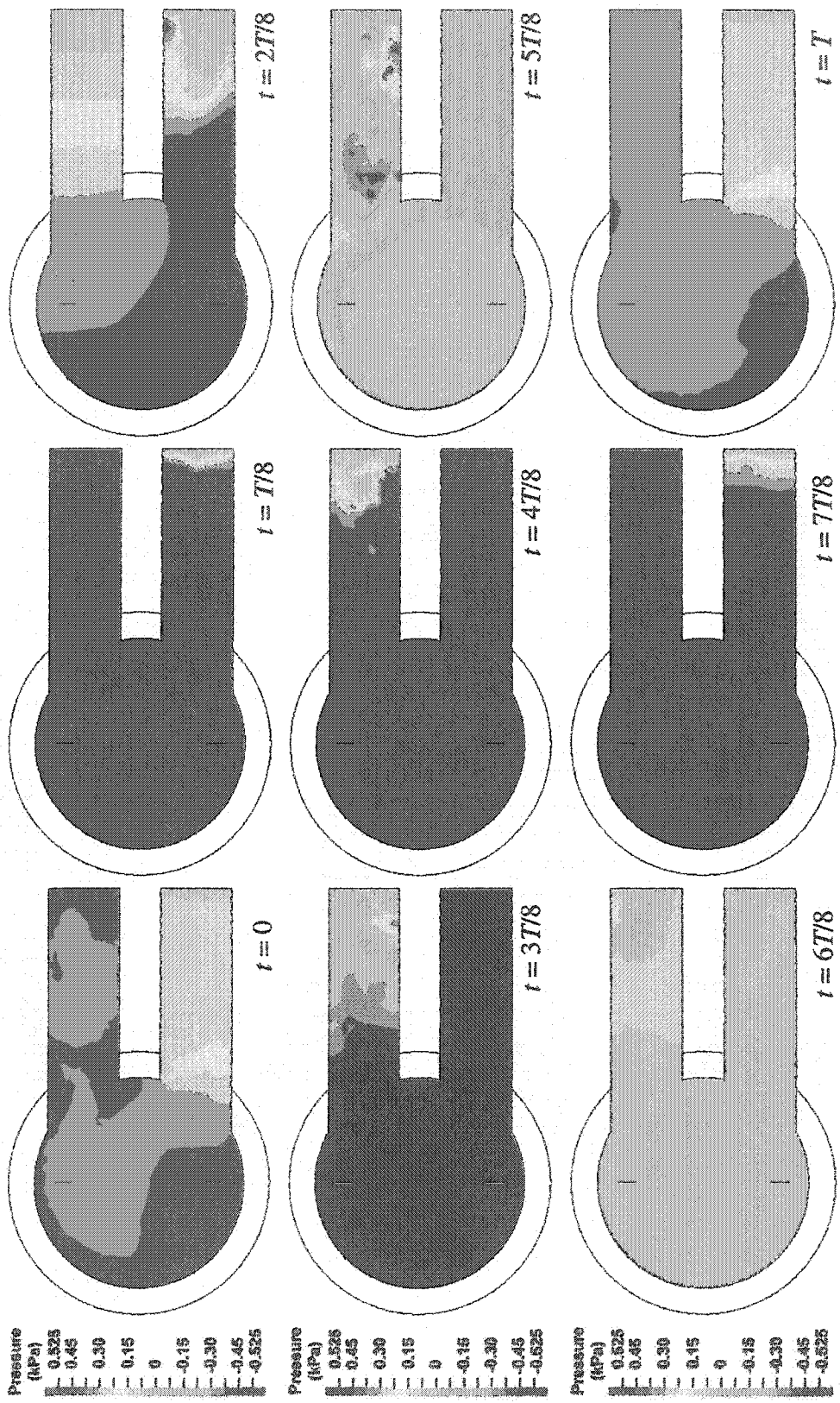

Figure 23. Open loop pressure bands for one period.

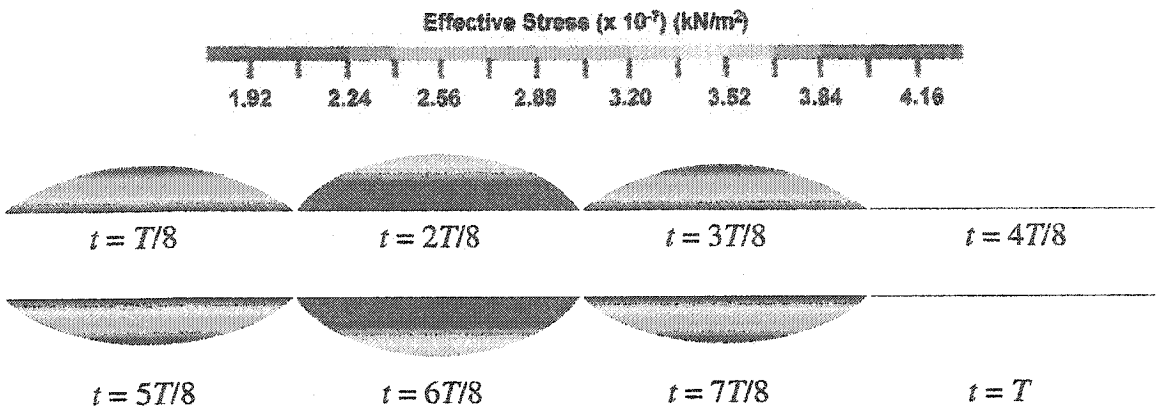

Figure 24. Side view of diaphragm effective stress for one period.

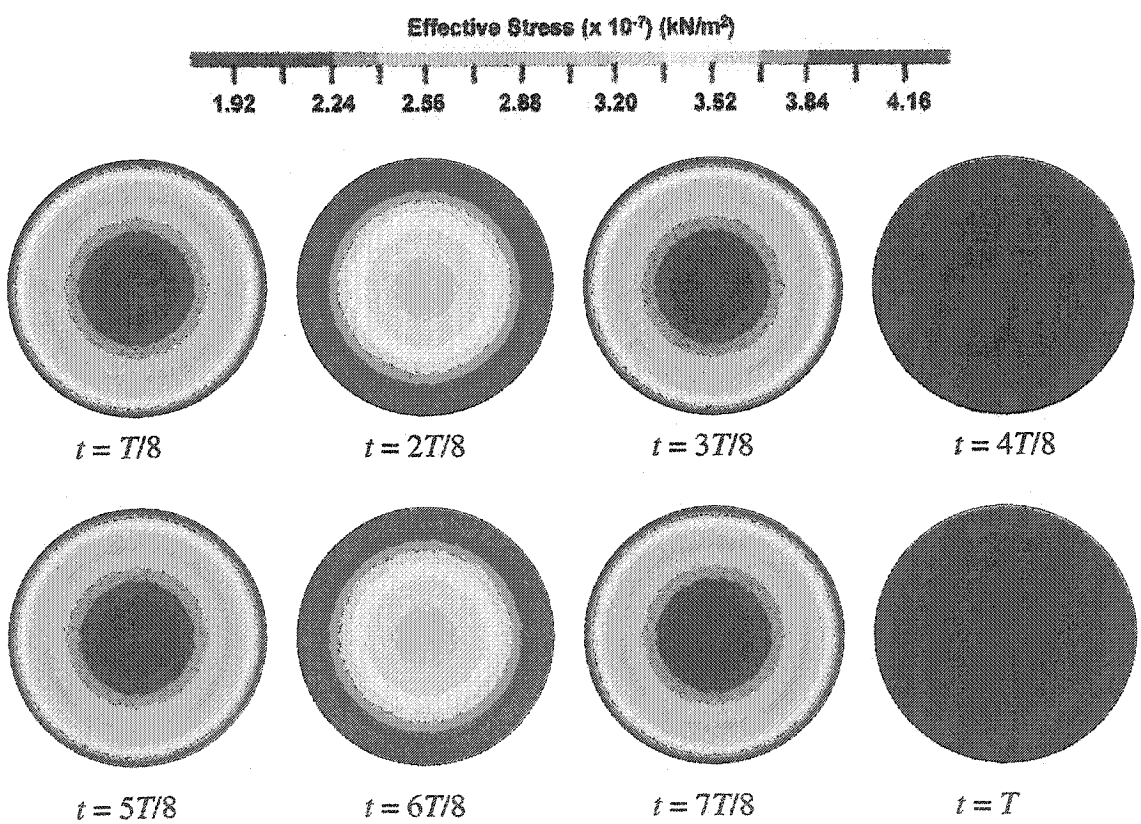

Figure 25. Top view of diaphragm effective stress for one period.

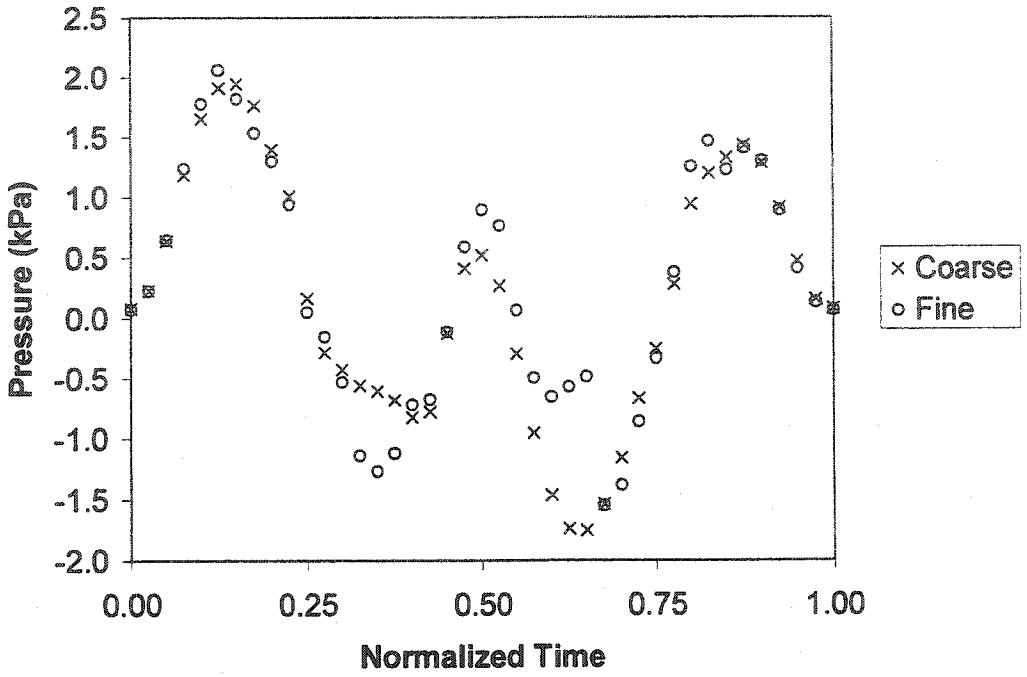

Figure 26. Pressure at point *a* for different mesh densities.

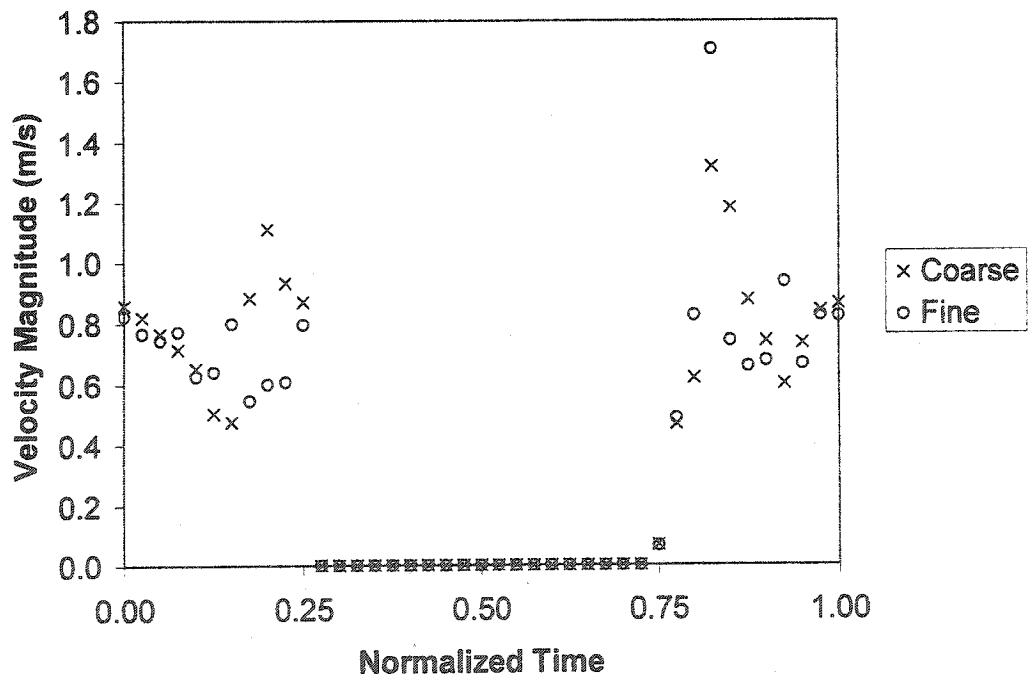

Figure 27. Velocity magnitude at point *b* for different mesh densities.

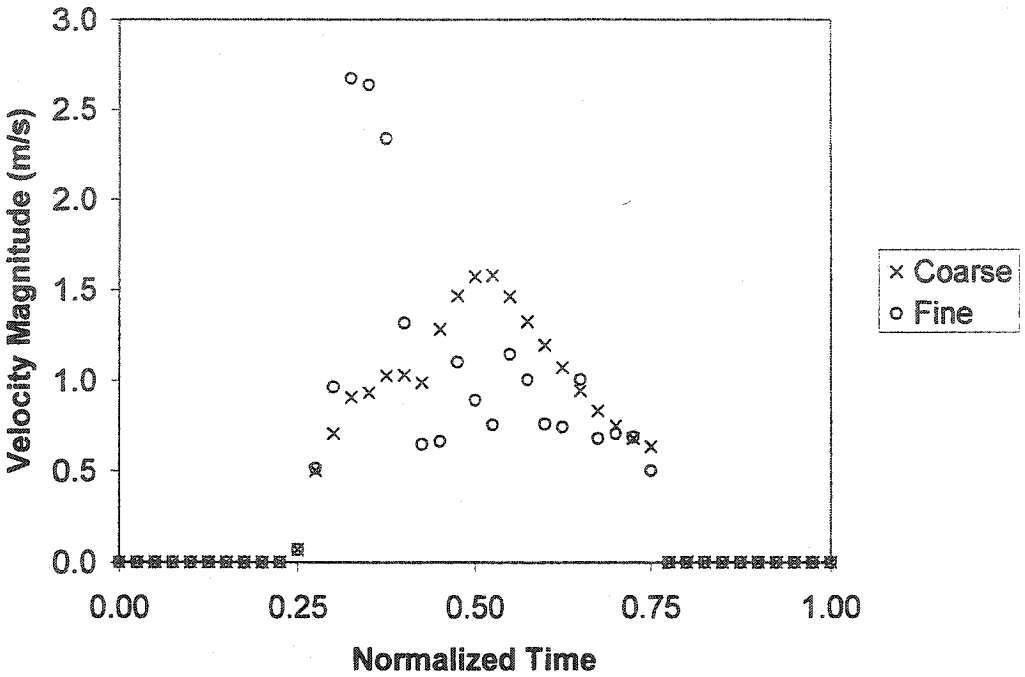

Figure 28. Velocity magnitude at point *c* for different mesh densities.

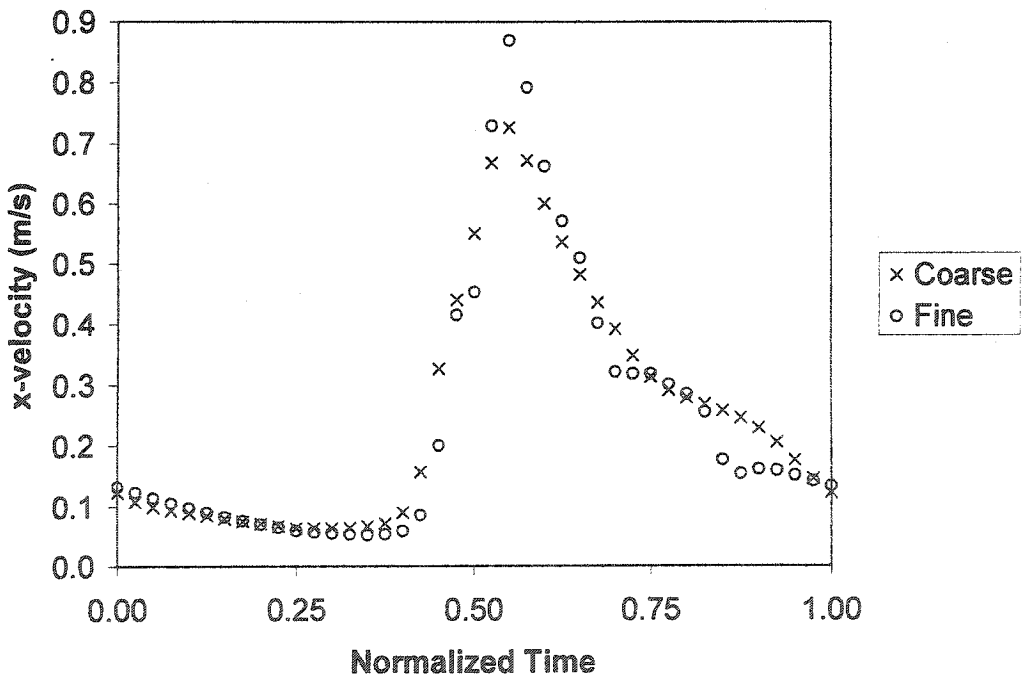

Figure 29. *x*-velocity at point *d* for different mesh densities.

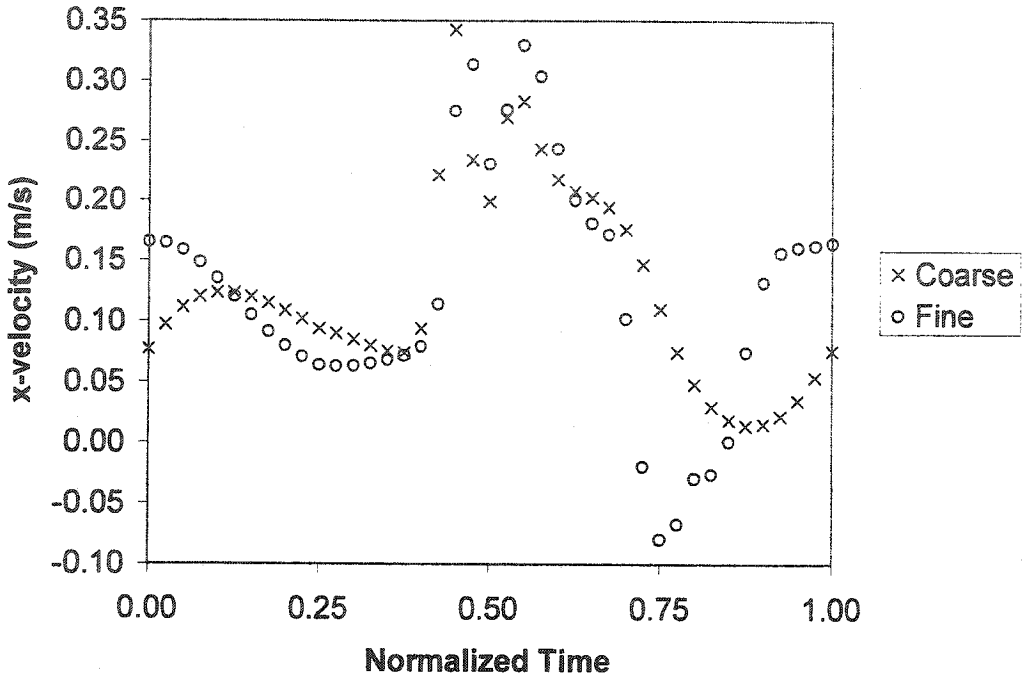

Figure 30. *x*-velocity at point *e* for different mesh densities.

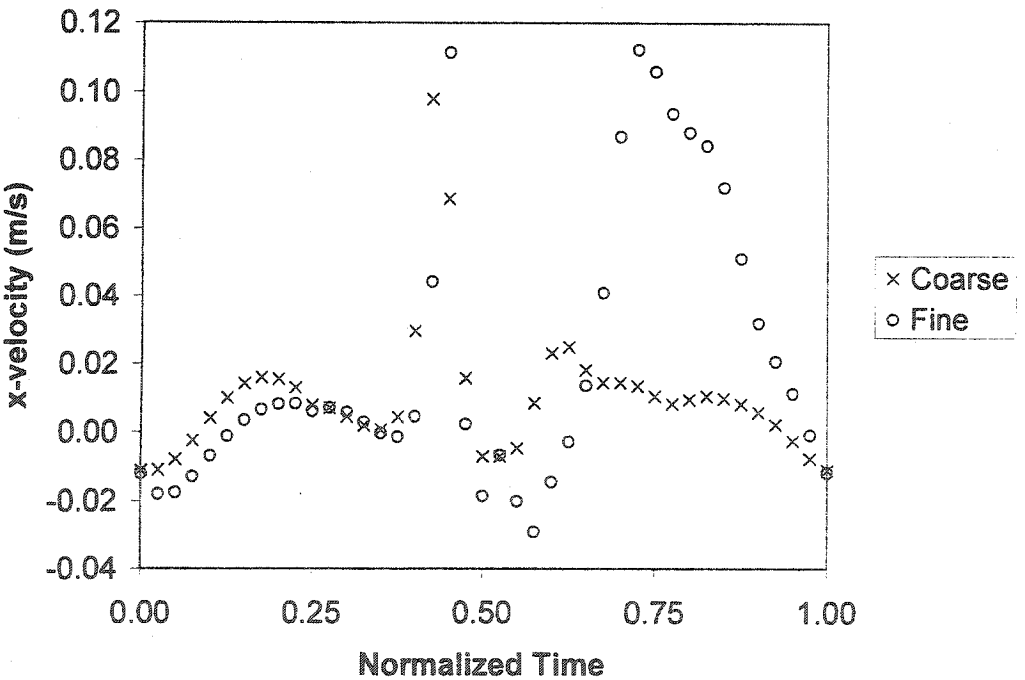

Figure 31. *x*-velocity at point *f* for different mesh densities.

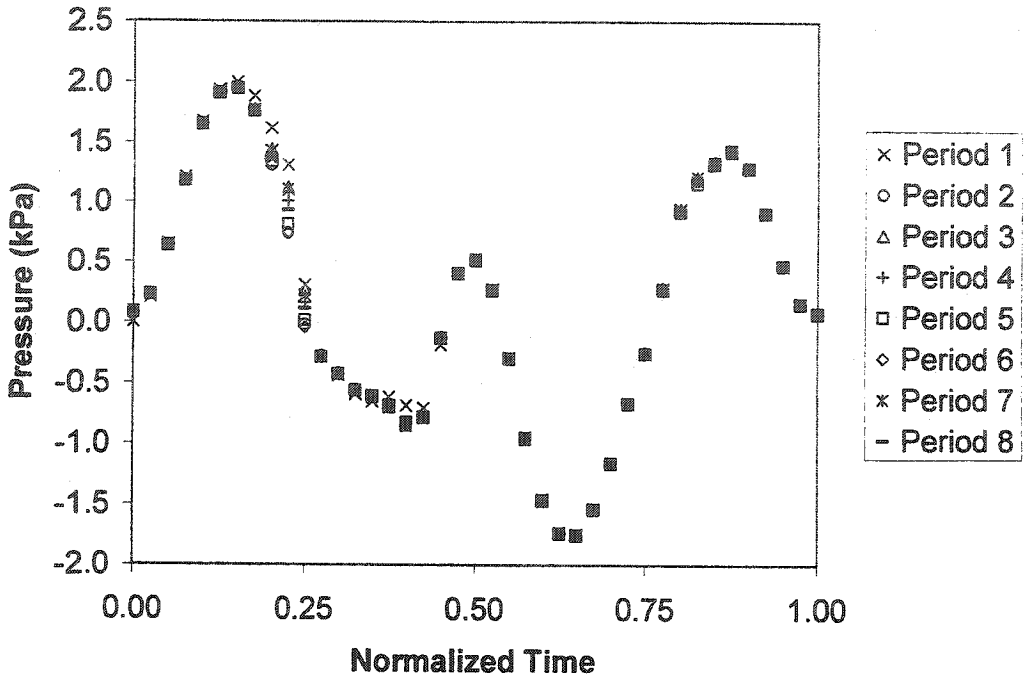

Figure 32. Pressure at point *a* for multiple periods with the coarse mesh.

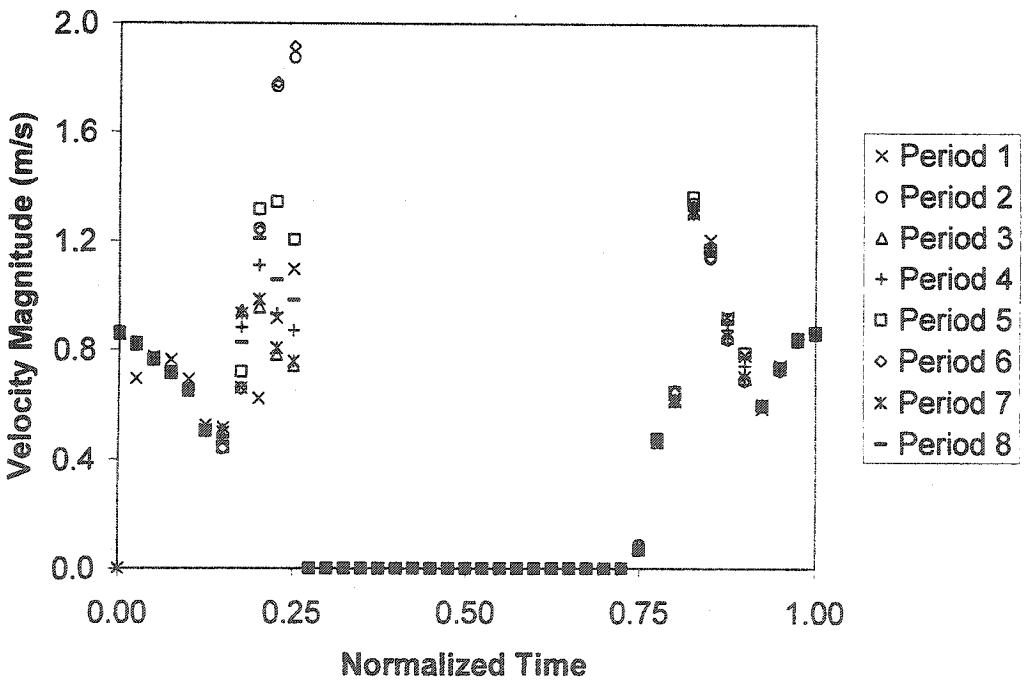

Figure 33. Velocity magnitude at point *b* for multiple periods with the coarse mesh.

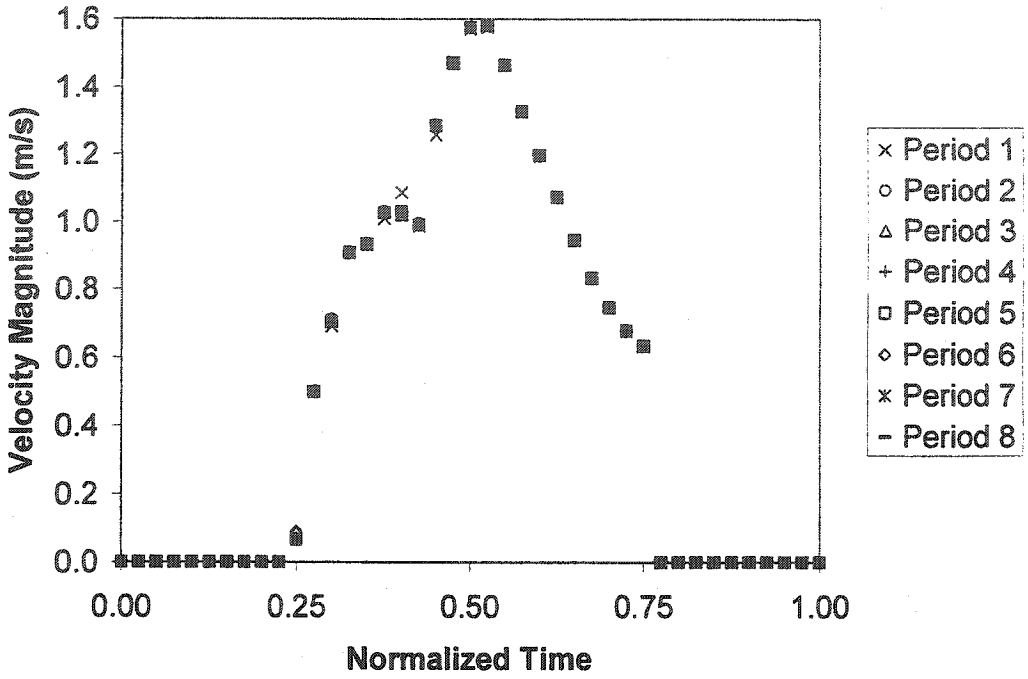

Figure 34. Velocity magnitude at point *c* for multiple periods with the coarse mesh.

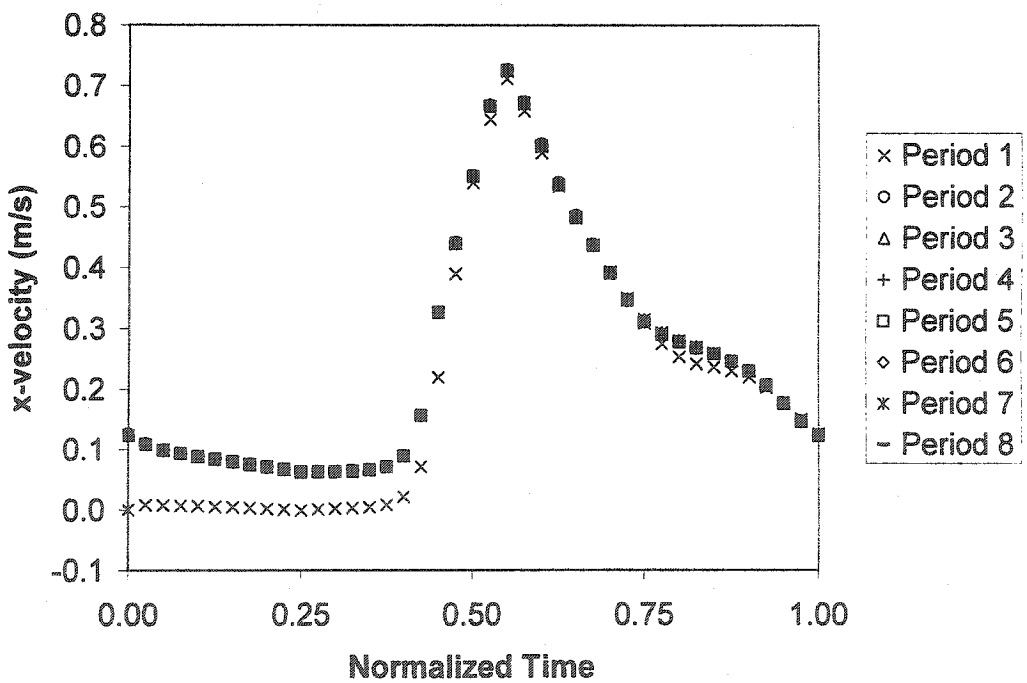

Figure 35. *x*-velocity at point *d* for multiple periods with the coarse mesh.

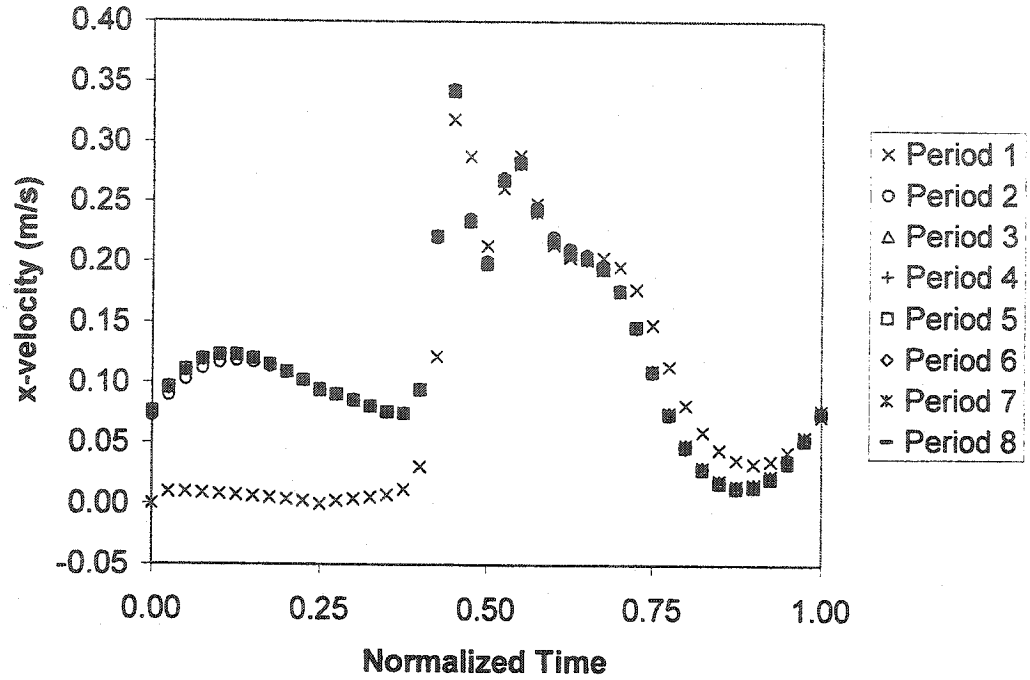

Figure 36. *x*-velocity at point *e* for multiple periods with the coarse mesh.

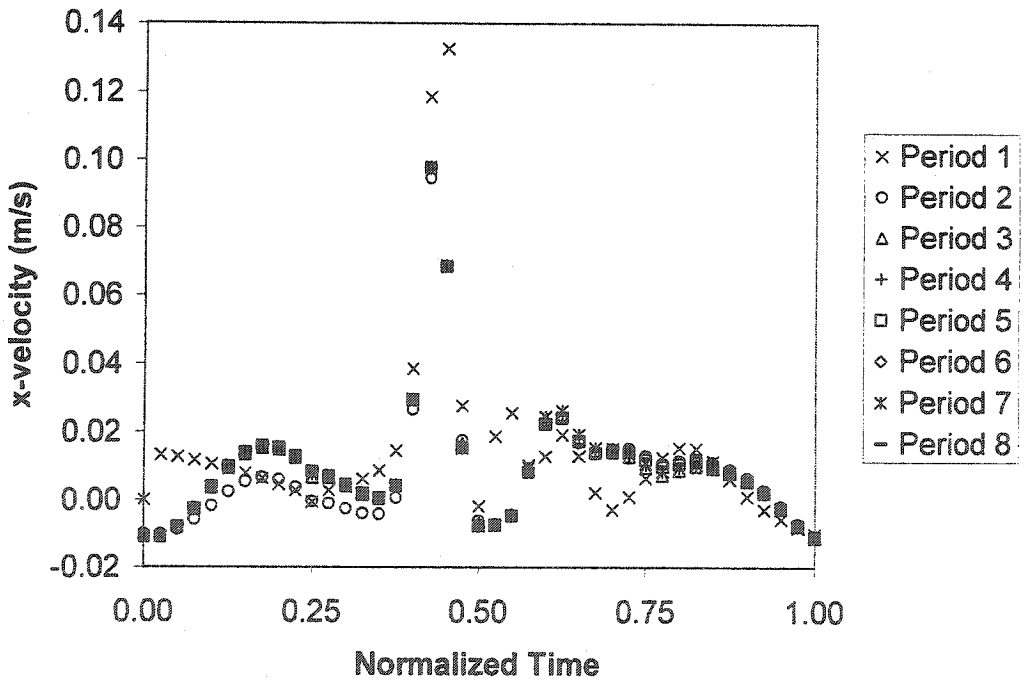

Figure 37. *x*-velocity at point *f* for multiple periods with the coarse mesh.

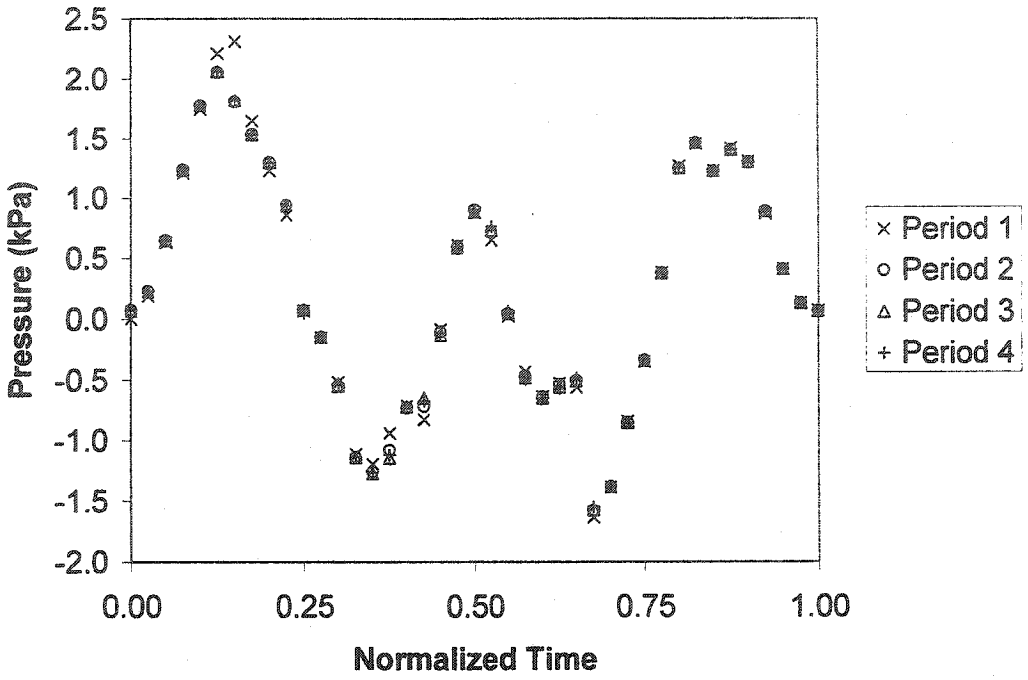

Figure 38. Pressure at point *a* for multiple periods with the fine mesh.

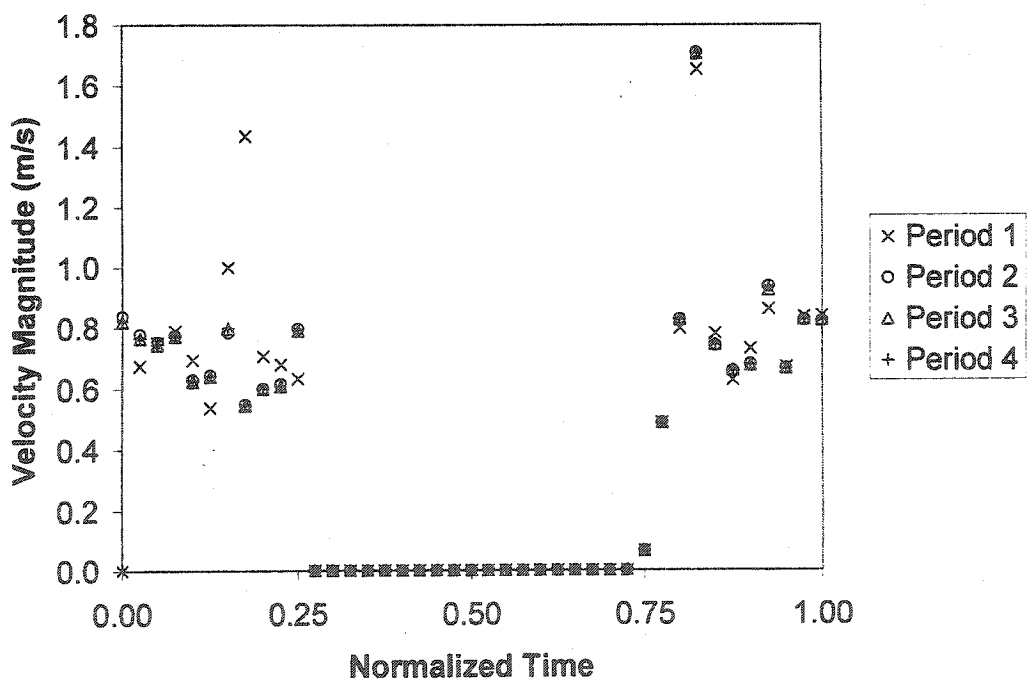

Figure 39. Velocity magnitude at point *b* for multiple periods with the fine mesh.

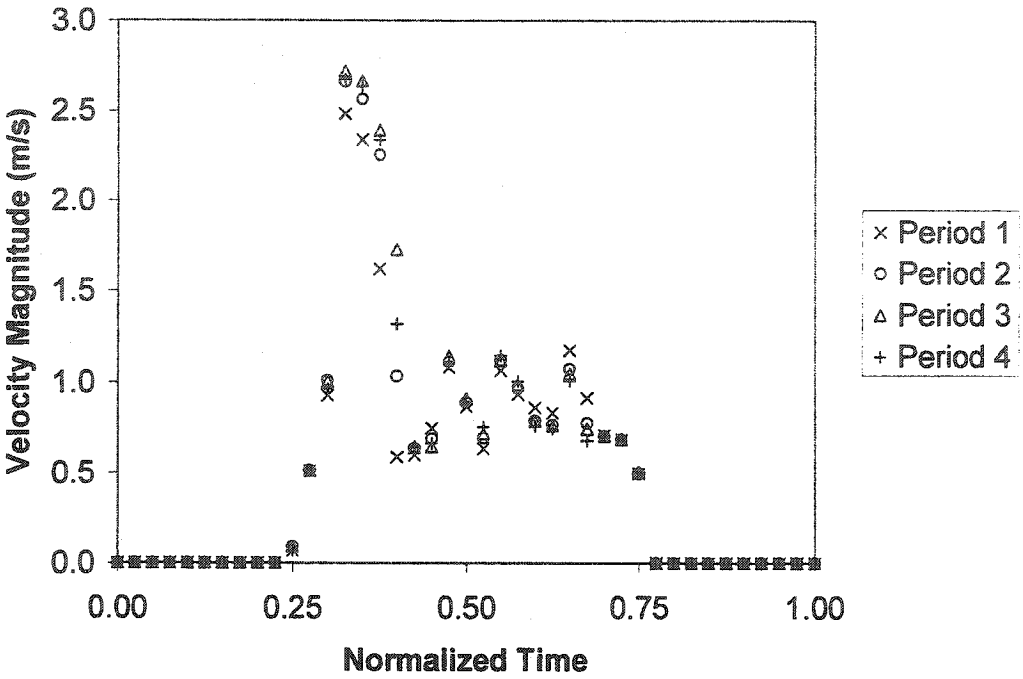

Figure 40. Velocity magnitude at point *c* for multiple periods with the fine mesh.

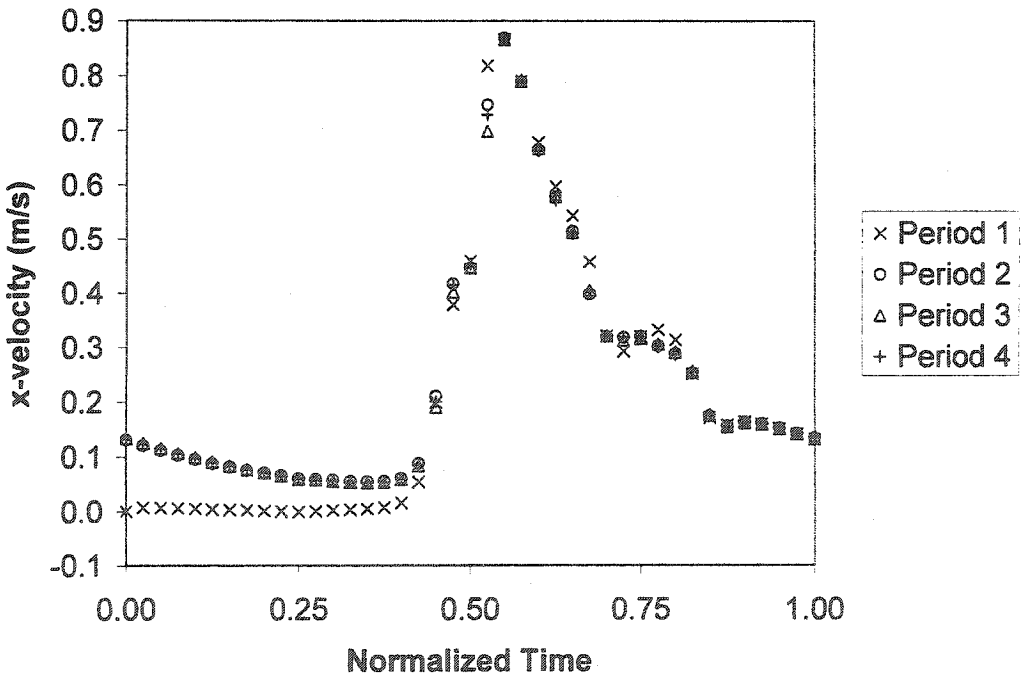

Figure 41. *x*-velocity at point *d* for multiple periods with the fine mesh.

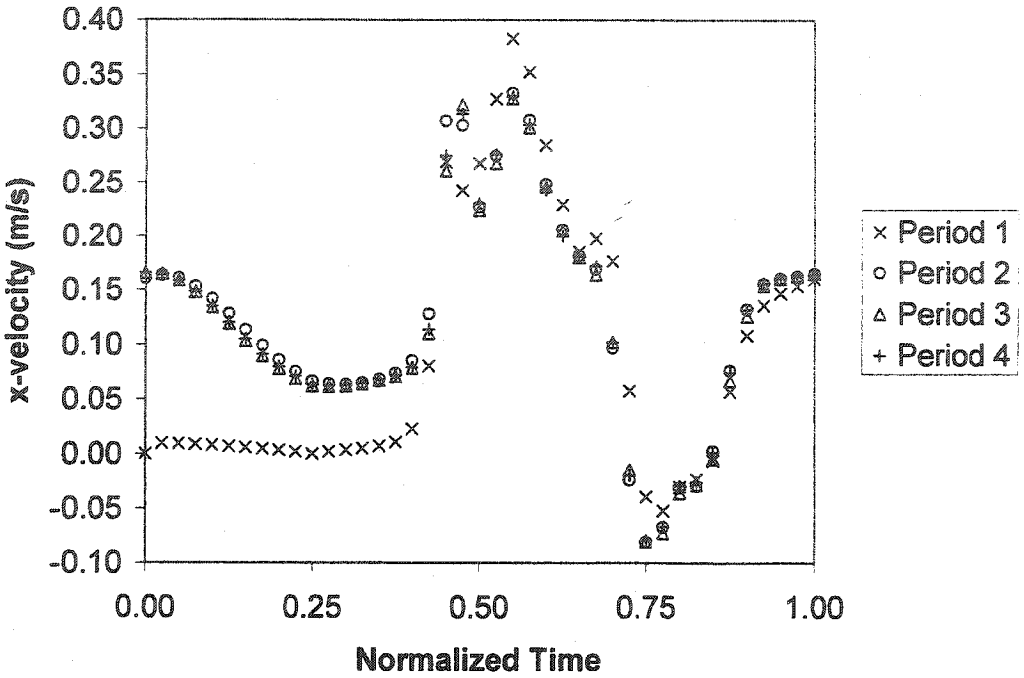

Figure 42. *x*-velocity at point *e* for multiple periods with the fine mesh.

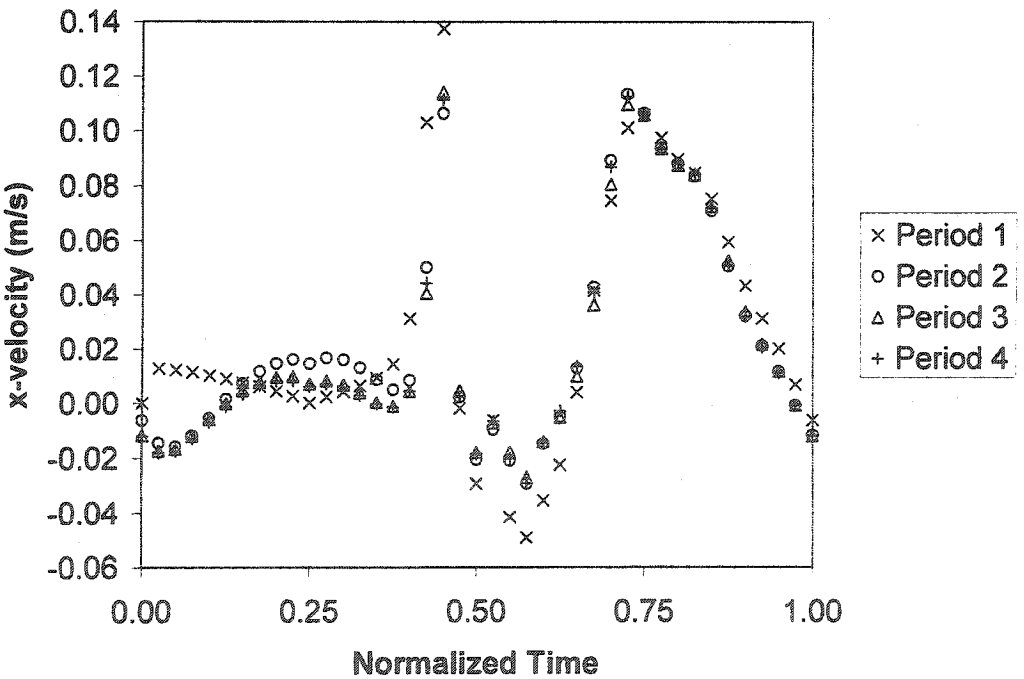

Figure 43. *x*-velocity at point *f* for multiple periods with the fine mesh.

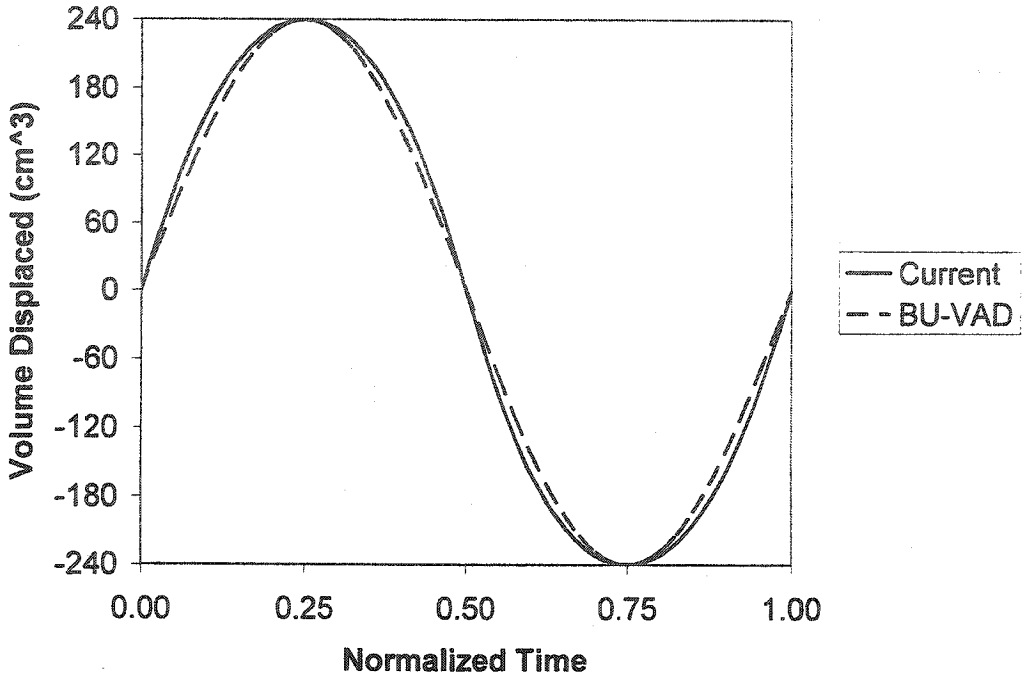

Figure 44. Comparison of blood chamber volume displacements.

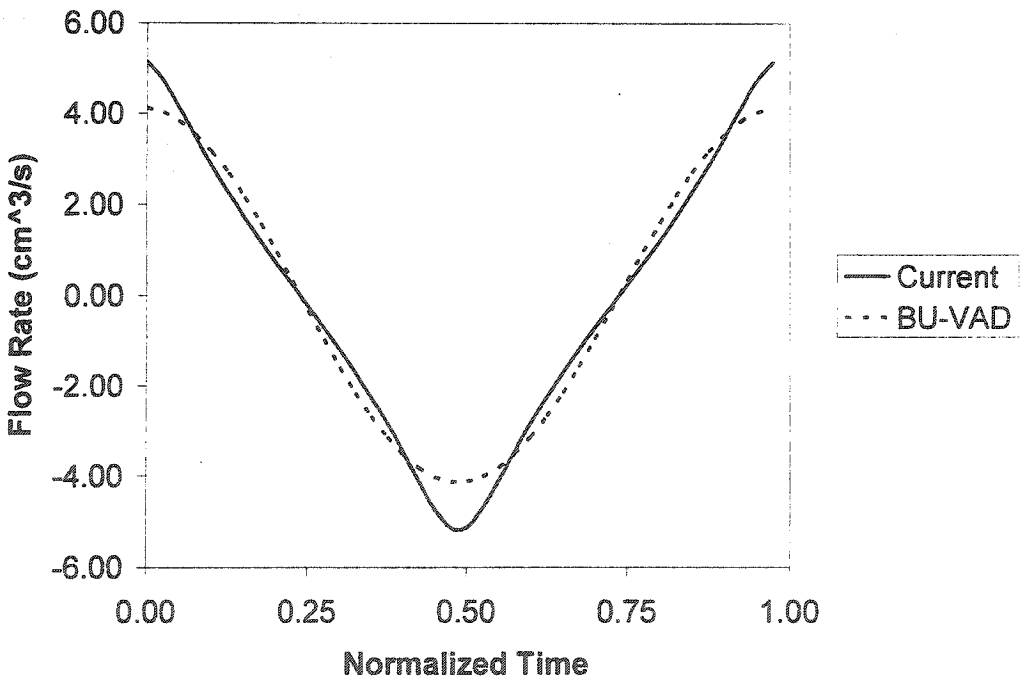

Figure 45. Comparison of blood chamber inlet/outlet tube flow rates.

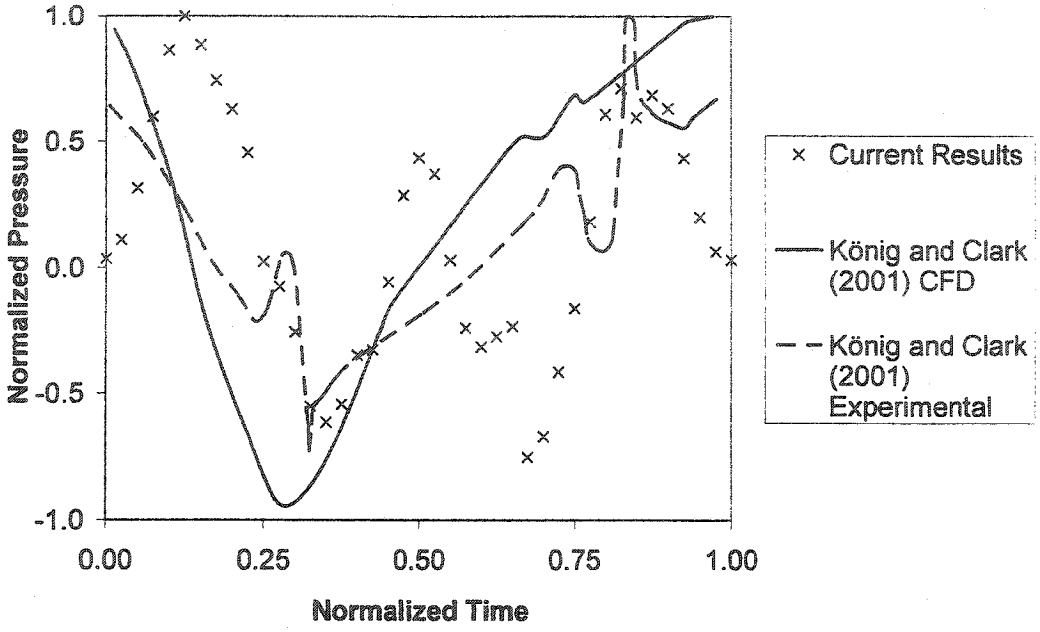

Figure 46. Comparison of pressures at node *a*.

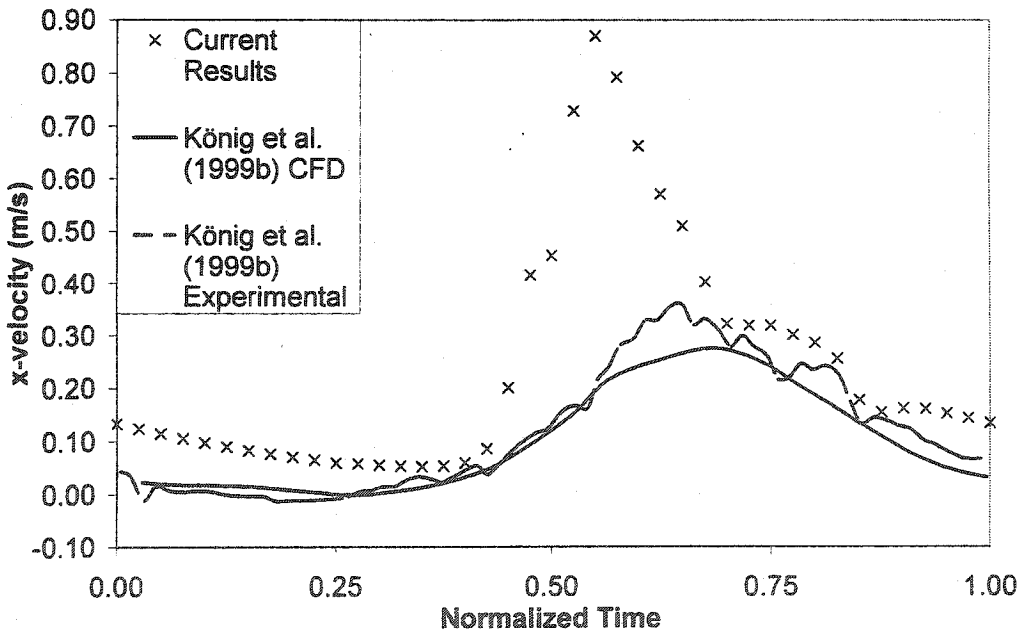

Figure 47. Comparison of *x*-velocities at node *d*.

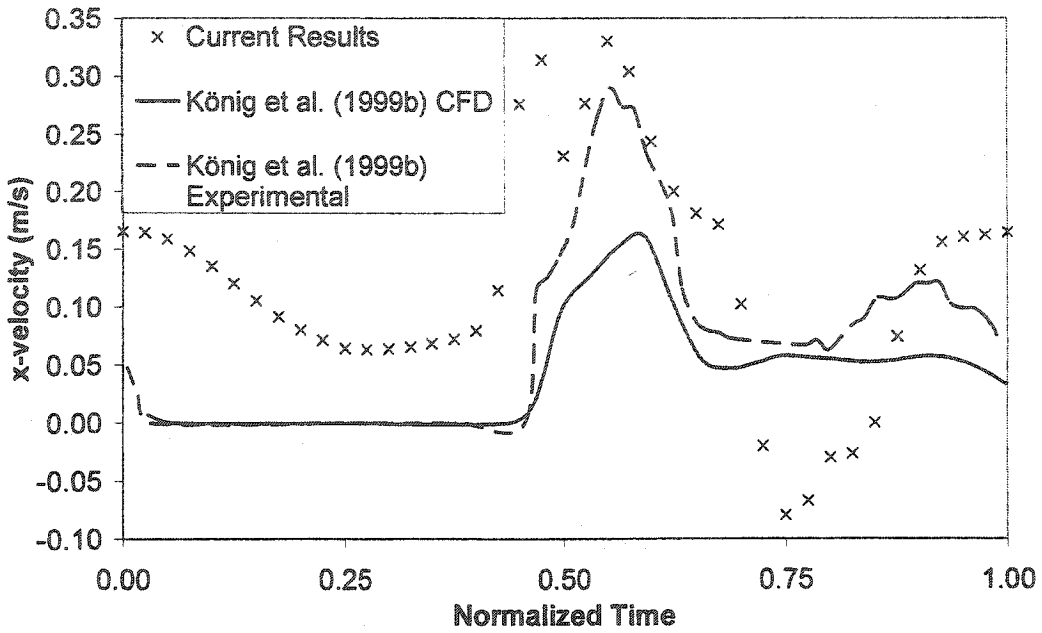

Figure 48. Comparison of *x*-velocities at node *e*.

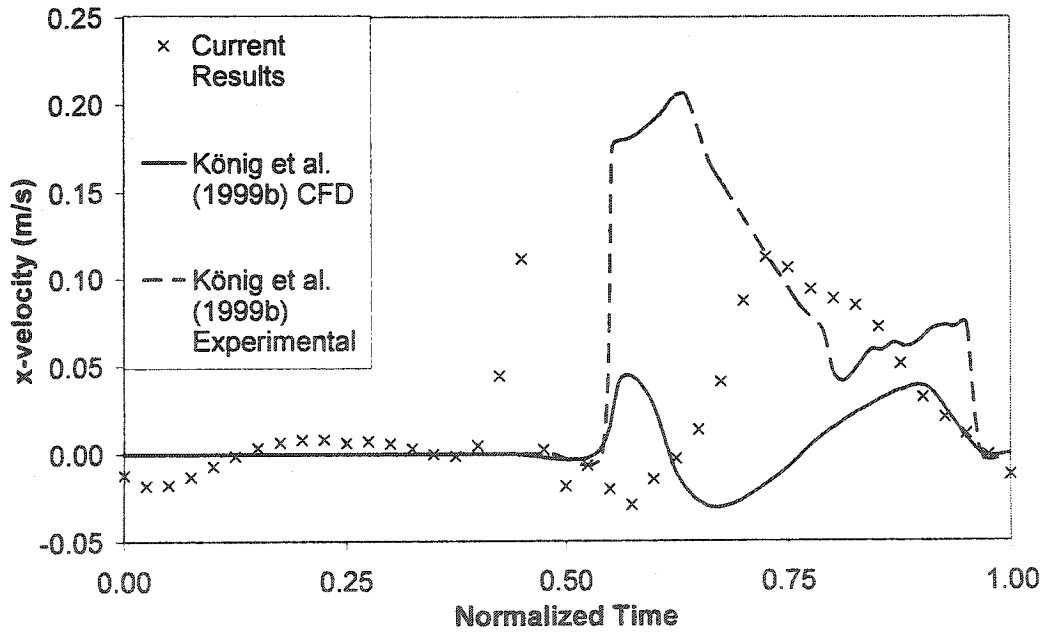

Figure 49. Comparison of *x*-velocities at point *f*.

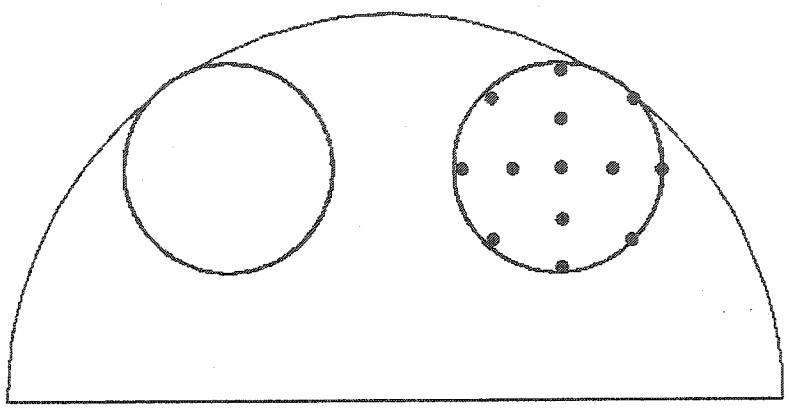

Figure 50. Location of particles in blood chamber inlet tube.

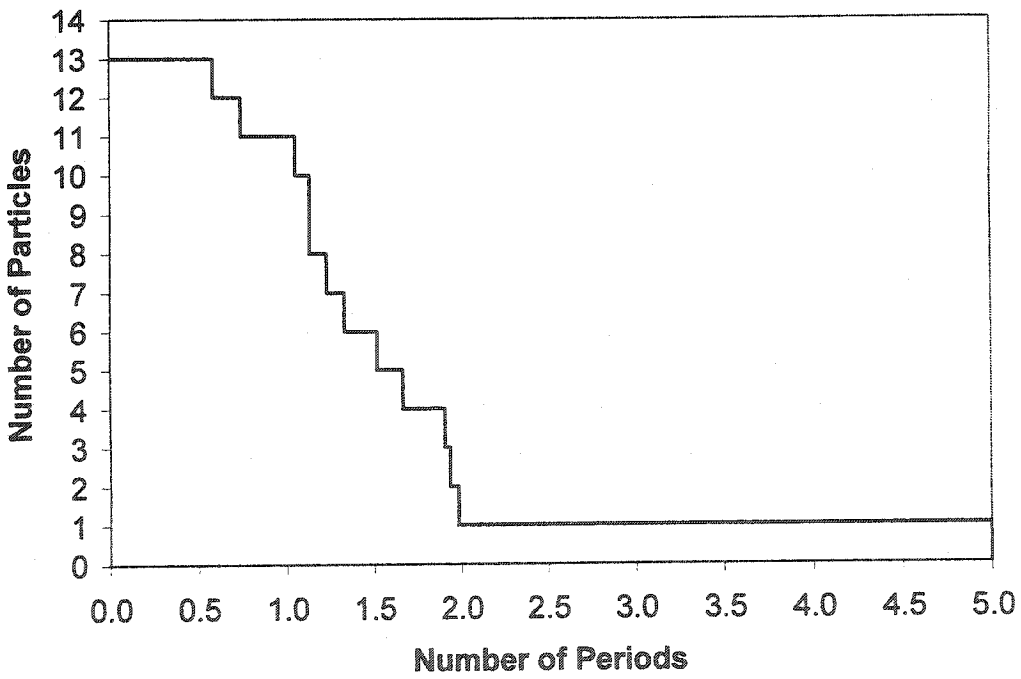

Figure 51. Number of particles residing within the VAD over five periods.

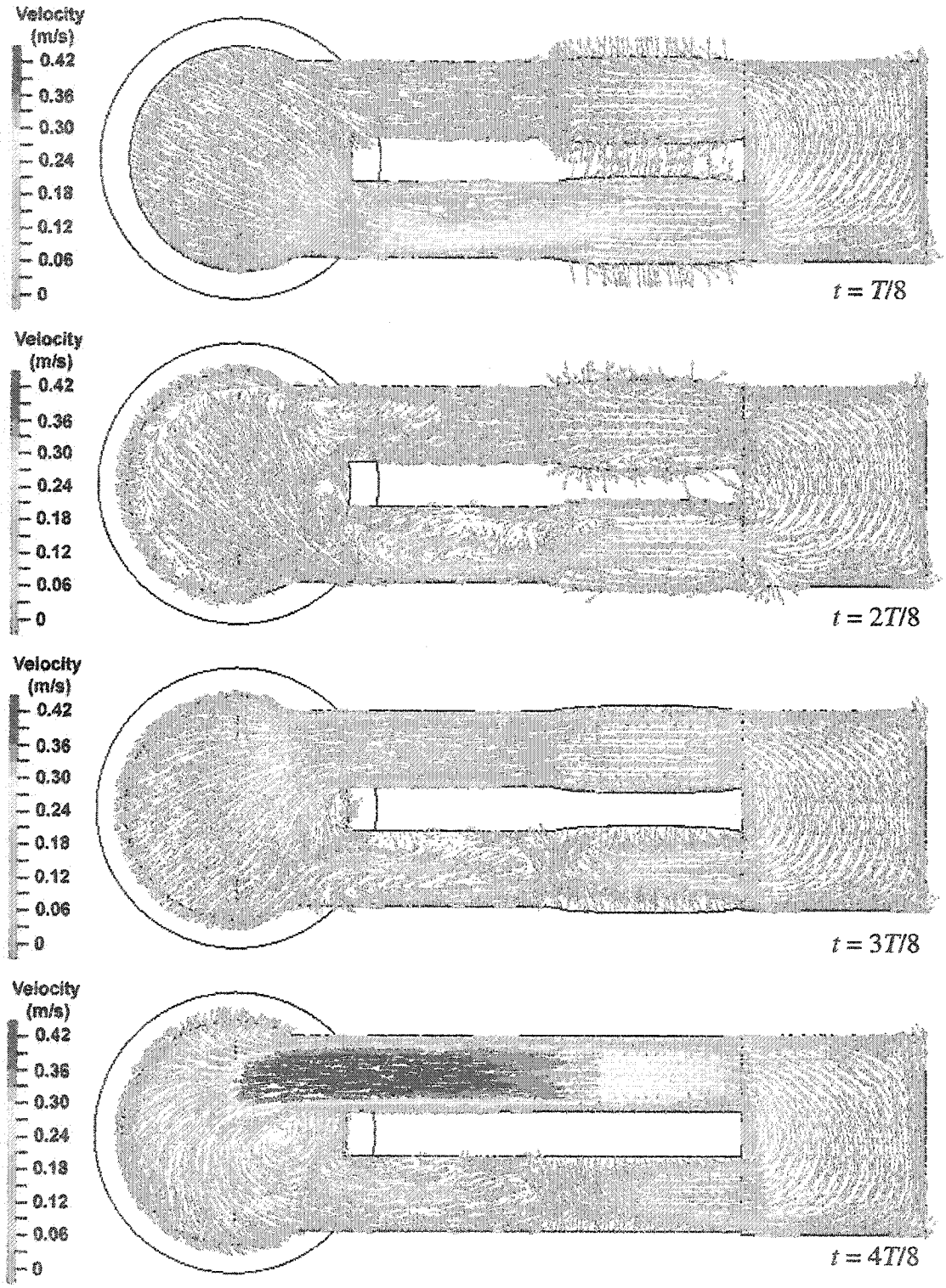

Figure 52. Closed loop velocity vectors for the first half of one period.

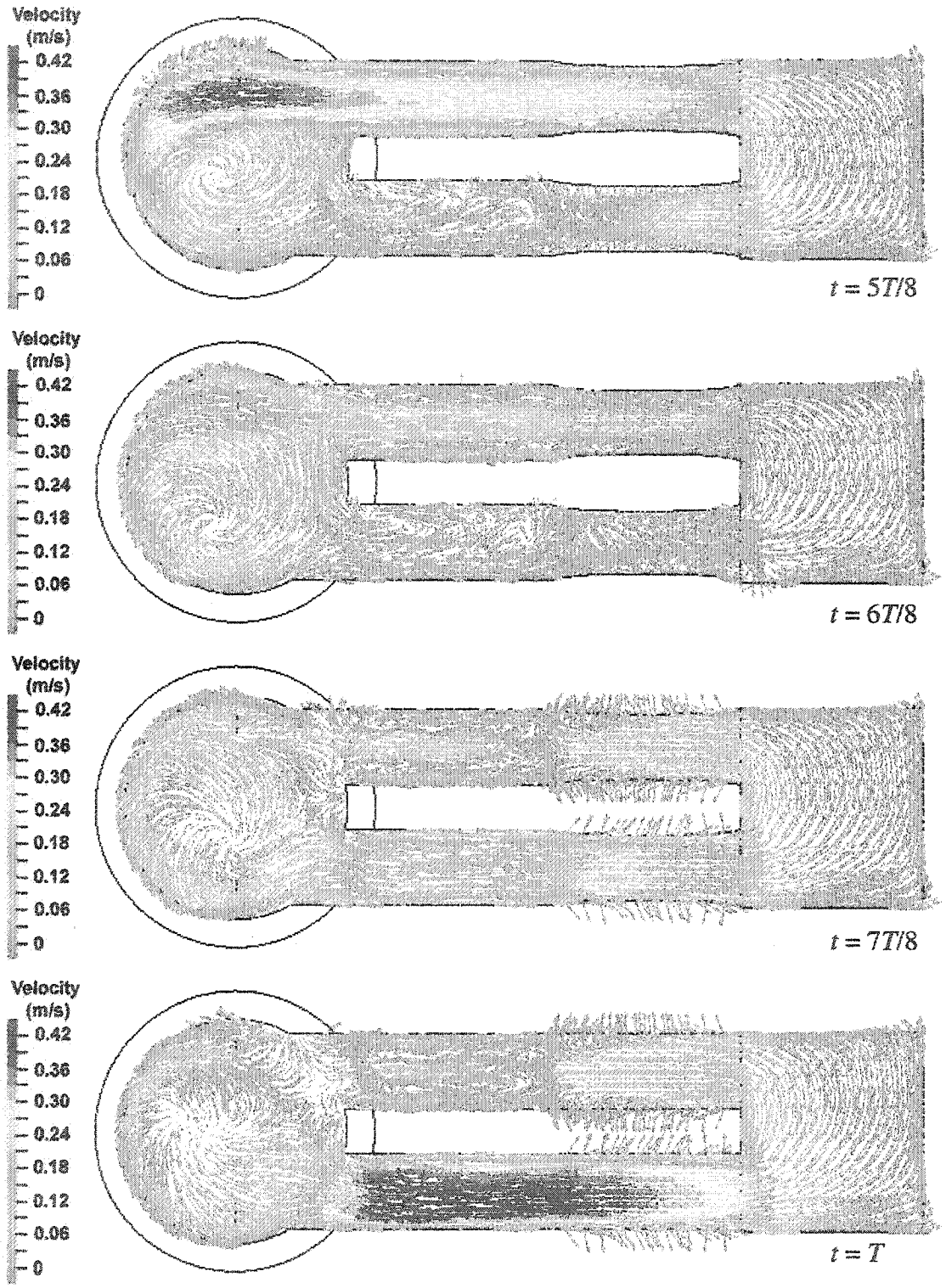

Figure 53. Closed loop velocity vectors for the second half of one period.

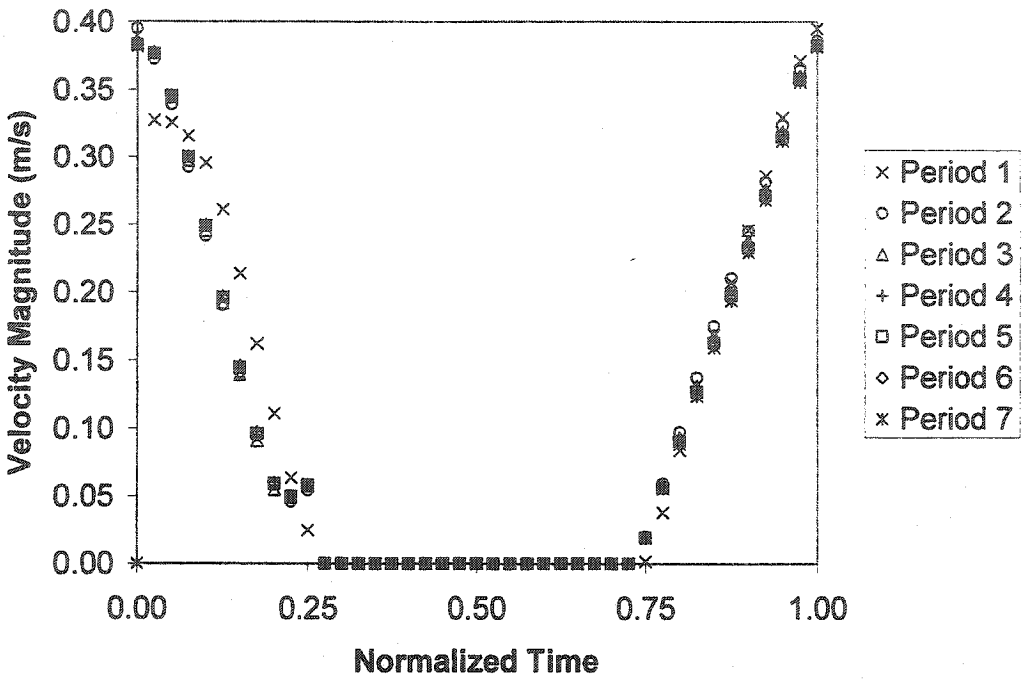

Figure 54. Velocity magnitude at point *b* for multiple periods.

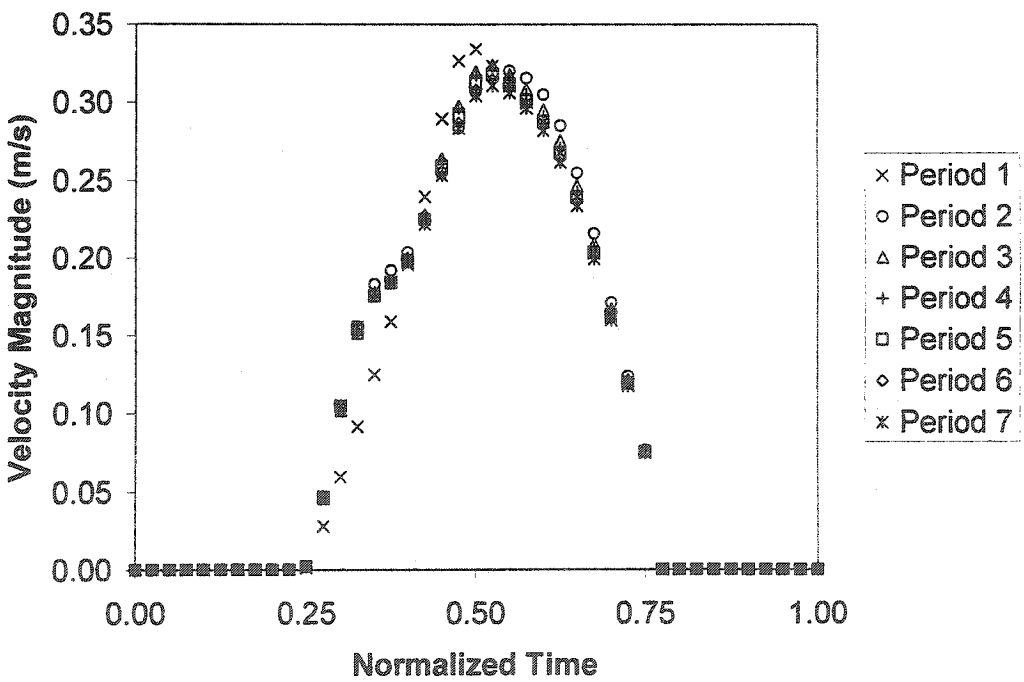

Figure 55. Velocity magnitude at point *c* for multiple periods.

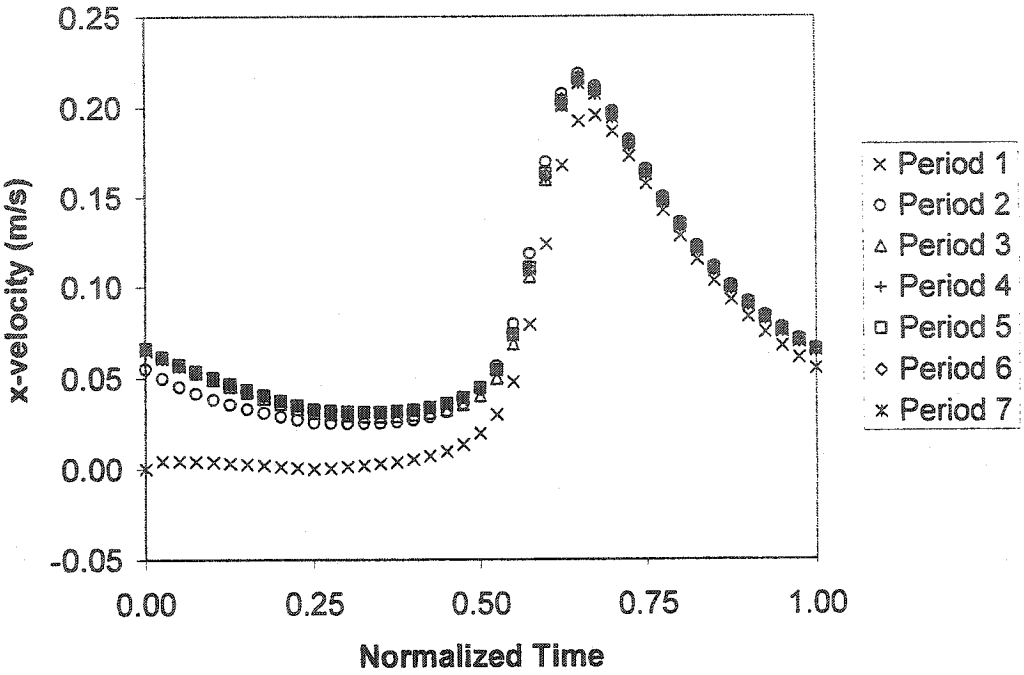

Figure 56. *x*-velocity at point *d* for multiple periods.

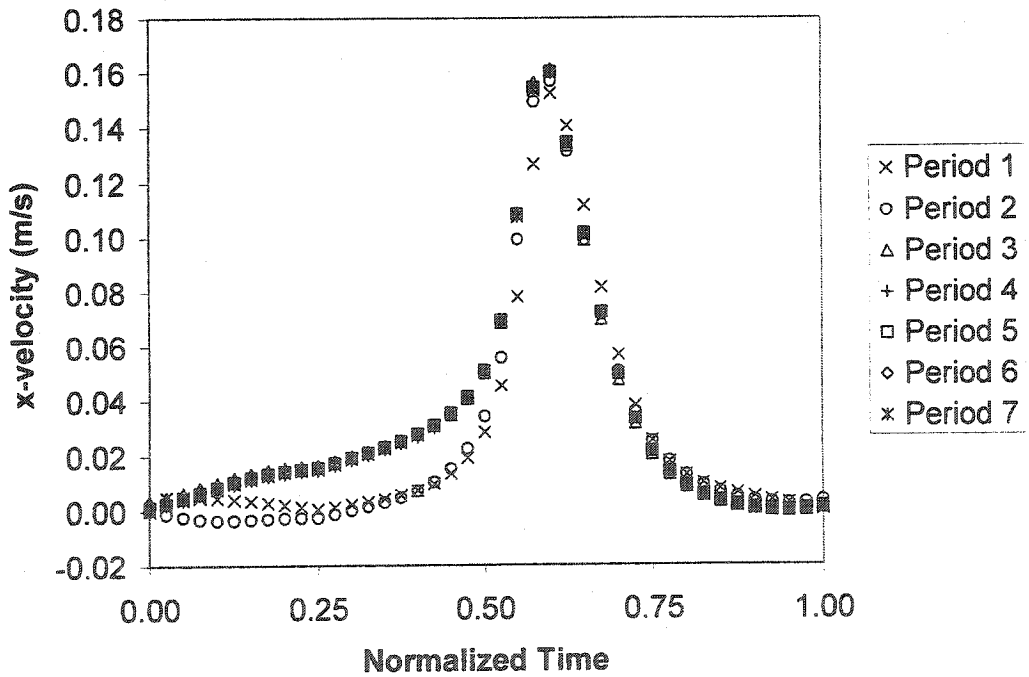

Figure 57. *x*-velocity at point *e* for multiple periods.

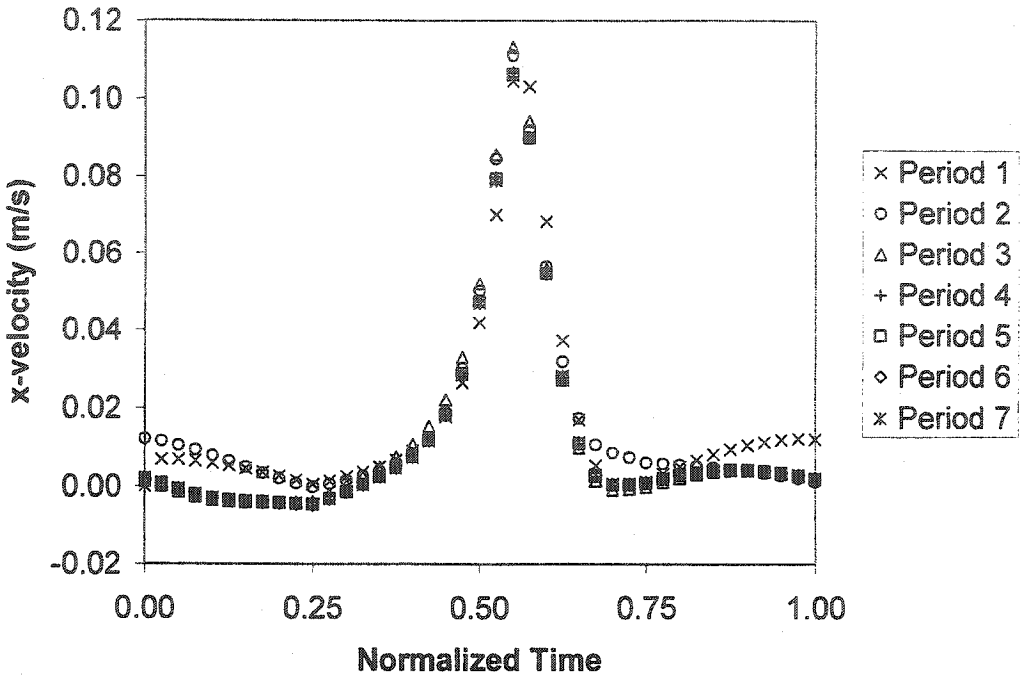

Figure 58. *x*-velocity at point *f* for multiple periods.

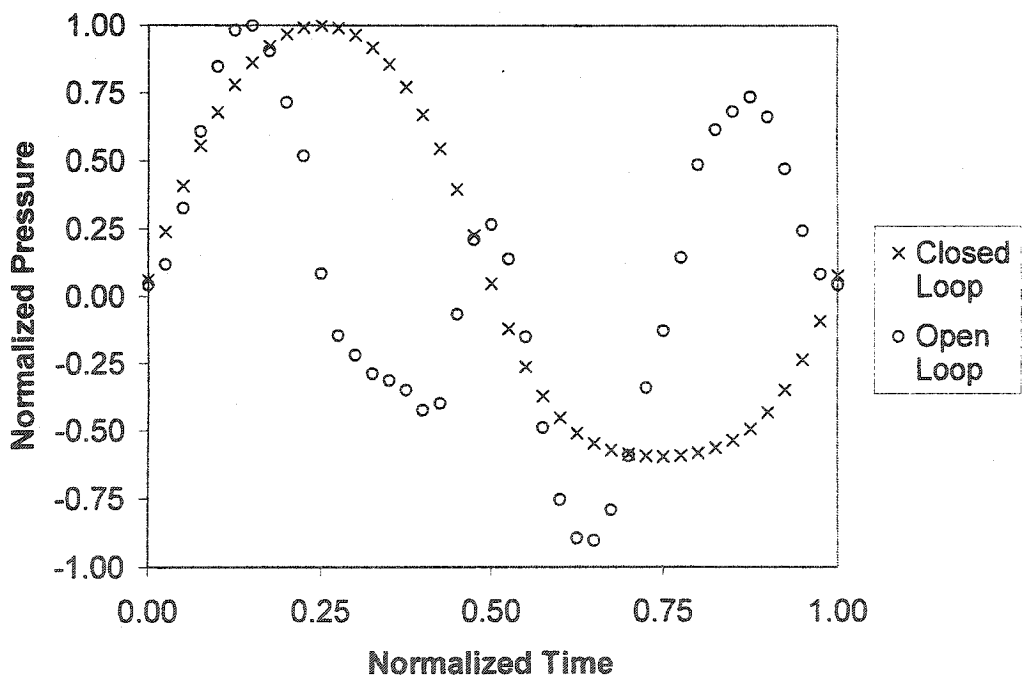

Figure 59. Normalized pressure at node *a* for closed and open loop models.

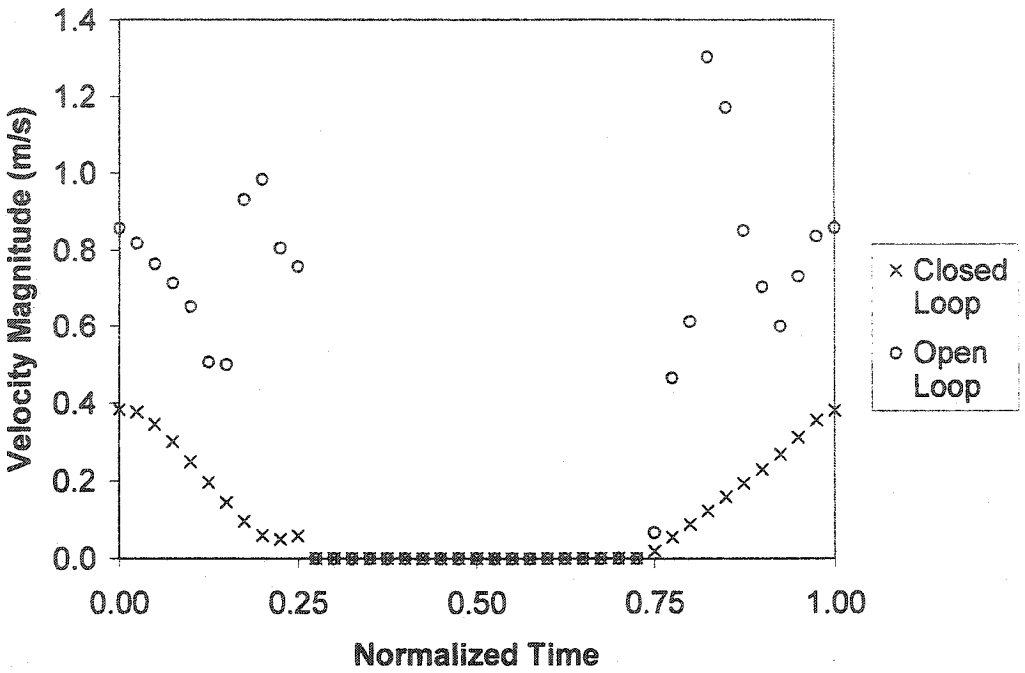

Figure 60. Velocity magnitude at point *b* for closed and open loop models.

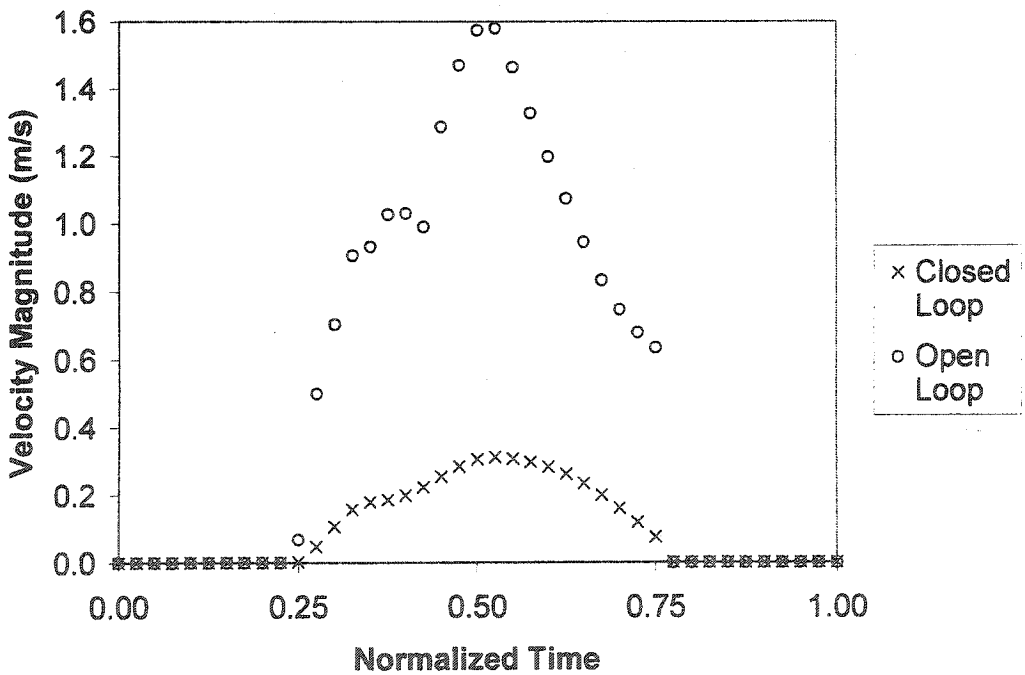

Figure 61. Velocity magnitude at point *c* for closed and open loop models.

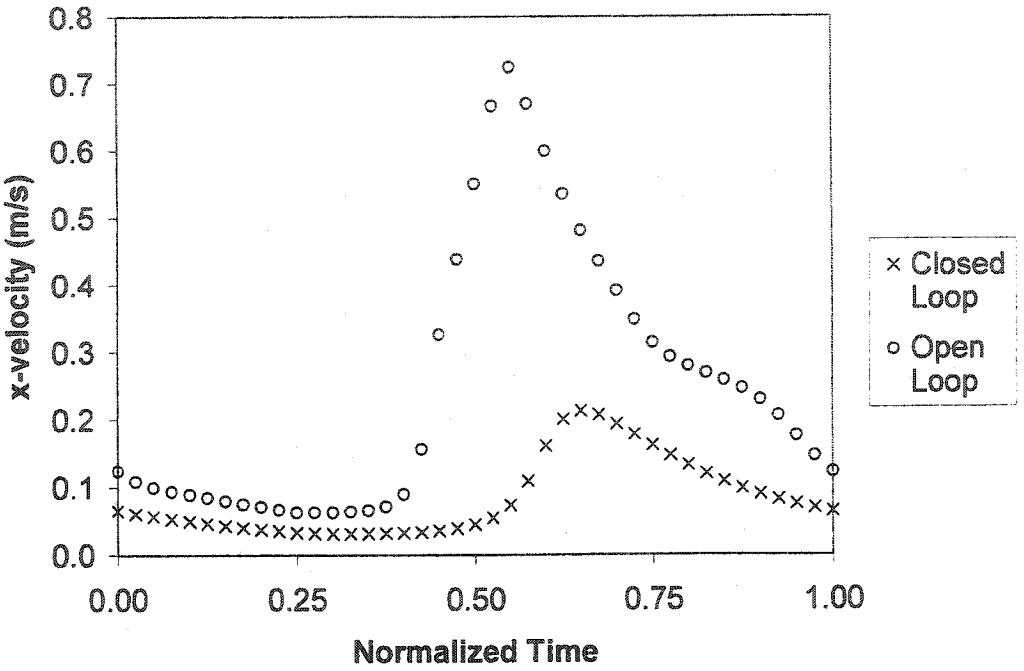

Figure 62. *x*-velocity at point *d* for closed and open loop models.

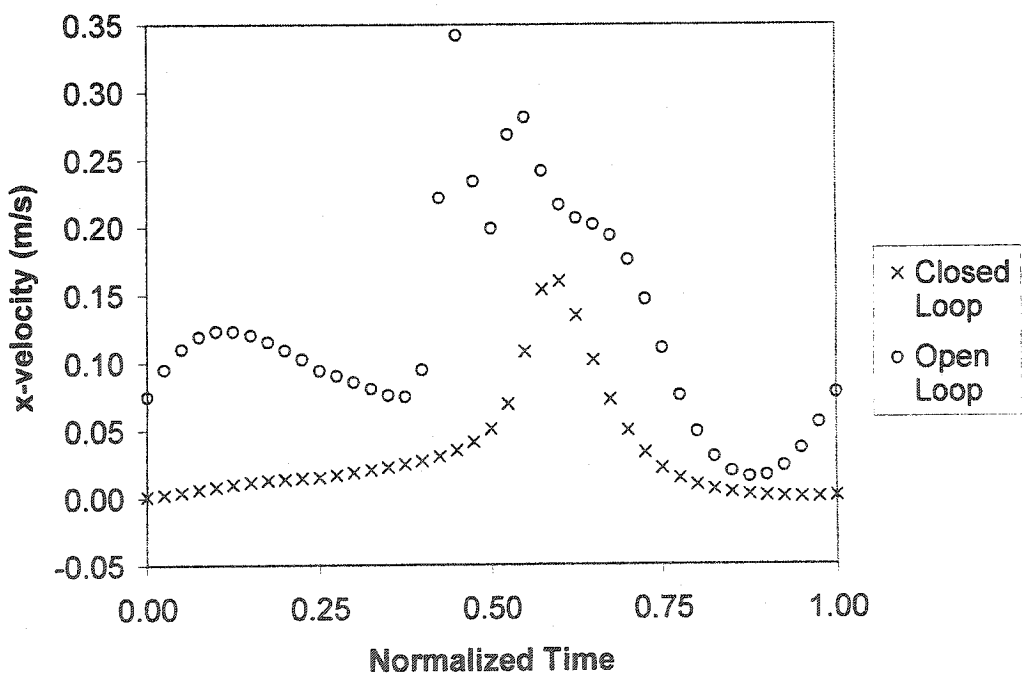

Figure 63. *x*-velocity at point *e* for closed and open loop models.

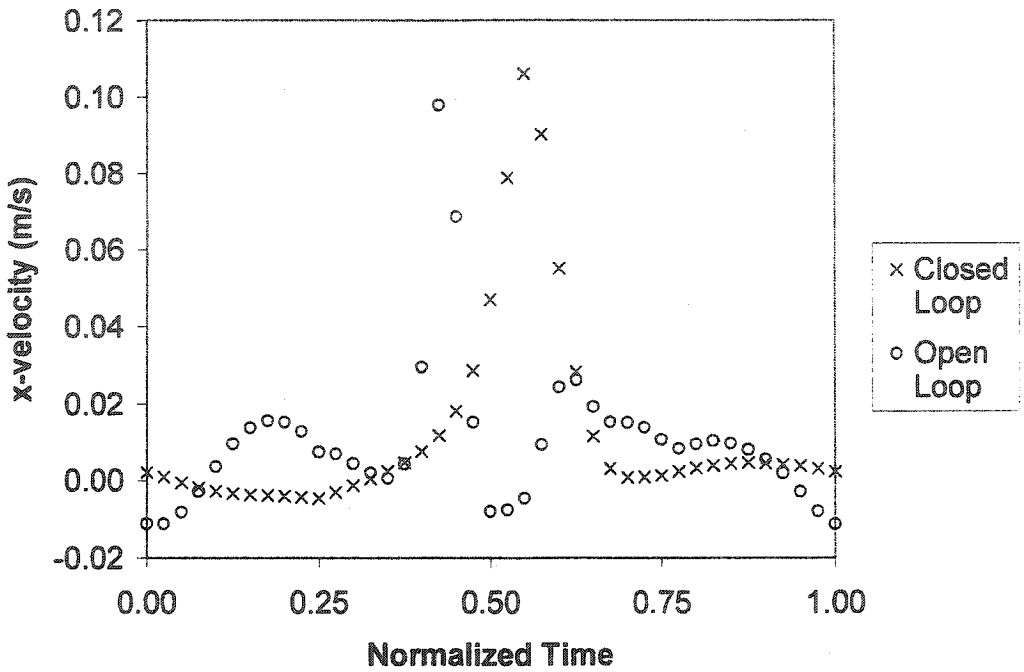

Figure 64. *x*-velocity at point *f* for closed and open loop models.

FIGURE CREDITS

Figure 2. Reprinted from *Journal of Heart and Lung Transplantation,* V. 18: 351-357. Chen, J. M. *et al.*: "Improved survival in patients with acute myocarditis using external pulsatile mechanical ventricular assistance". Copyright (1999), with permission from International Society for Heart and Lung Transplantation.

Figure 3. Reprinted with permission from Frazier, O. H. *et al.* (2000). Clinical left heart assist devices: A historical perspective. In D. J. Goldstein, & M. C. Oz (Eds.), *Cardiac Assist Devices* (pp. 3-13). Armonk, NY: Futura Publishing Company, Inc.

Figure 4. Reprinted by permission from Reul, H. The MEDOS/HIA system: Development, results, perspectives. *Thoracic and Cardiovascular Surgeon* (1999); 47: 311-315.

Figure 5. Reproduced with permission from "Intra and Extracorporeal Cardiovascular Fluid Dynamics, Volume 1: General Principles in Application", Ed. P. Verdonck, WIT Press, Southampton, UK, 1998, ISBN 1-85312-547-4.

Figure 6. Reprinted with permission from Frazier, O. H. *et al.* (2000). Clinical left heart assist devices: A historical perspective. In D. J. Goldstein, & M. C. Oz (Eds.), *Cardiac Assist Devices* (pp. 3-13). Armonk, NY: Futura Publishing Company, Inc.

Figure 7. Reprinted with permission from Yu, Y.-C., *et al.* (2001). Pressure-volume relationship of a pulsatile blood pump for ventricular assist device development. *ASAIO Journal, 47* (*3*), 293-301.

Figure 8. Reprinted from *Annals of Thoracic Surgery,* V. 71: S166-S170. Hendry, P. J. *et al.*: "The HeartSaver left ventricular assist device: An update". Copyright (2001), with permission from Society of Thoracic Surgeons.

Figure 9. Reprinted from *Annals of Thoracic Surgery,* V. 71: S156-S161. Mehta, S. M. *et al.*: "The LionHeart LVD-2000: A completely implantable left ventricular assist device for chronic circulatory support". Copyright (2001), with permission from Society of Thoracic Surgeons.

Figure 10. Reprinted from *Journal of Biomechanics*, V. 27: 43-55. Jin, W., & Clark, C.: "Experimental investigation of the motions of the pumping diaphragm within a sac-type pneumatically driven ventricular assist device". Copyright (1994), with permission from Elsevier.

Figure 11. Reprinted from *Medical Engineering and Physics*, V. 23, 99-110. König, C. S., & Clark, C.: "Flow mixing and fluid residence times in a model of a ventricular assist device". Copyright (2001), with permission from The Institute of Physics and Engineering in Medicine.